# Local field modeling of interaction between a soil body and a falling boulder

Lingran Zhang

## ▶ To cite this version:

## HAL Id: tel-01278478
## https://tel.archives-ouvertes.fr/tel-01278478

Submitted on 24 Feb 2016

# UNIVERSITÉ GRENOBLE ALPES

**THÈSE**

Pour obtenir le grade de

**DOCTEUR DE L'UNIVERSITÉ GRENOBLE ALPES**

Spécialité : **Matériaux, Mécanique, Génie civil, Electrochimie**

Arrêté ministériel : 7 août 2006

Présentée par

## Lingran ZHANG

Thèse dirigée par **François NICOT** et
codirigée par **Stéphane LAMBERT**

préparée au sein du **Laboratoire IRSTEA**
dans **l'École Doctorale Ingénierie-Matériaux Mécanique
Énergétique Environnement Procédés Production (I-MEP2)**

# Modélisation en champ proche de l'interaction entre sol et bloc rocheux

Thèse soutenue publiquement le **08  Décembre  2015**,
devant le jury composé de :

**M. Jian-Fu SHAO**
Professeur, Université Lille 1, Président

**M. Olivier  MILLET**
Professeur, Université de la Rochelle, Rapporteur

**M. Jérôme FORTIN**
Professeur, Université Picardie Jules Verne, Rapporteur

**M. David BERTRAND**
Maître de Conférences, INSA Lyon, Examinateur

**M. François NICOT**
Directeur de Recherche, Irstea de Grenoble, Directeur de thèse

**M. Stéphane LAMBERT**
Ingénieur de Recherche, Irstea de Grenoble, Co-Directeur de thèse

# Acknowledgements

First of all, I would like to thank my two dear supervisors François Nicot and Stéphane Lambert. Thank them very much for giving me this great opportunity to come to France and to do this PhD study. I am lucky to have them as supervisors. They put students' need in the first place and respond to student's questions very rapidly. They guide me to do researches and teach me to have very serious attitude towards research through our numerous discussions. Besides, I admire them for their their responsibilities and their commitments to research.

Second, I would like to thank the jury committee. Thank Mr. Jiaofu Shao, Olivier Millet, Jérôme Fortin, David Bertand very much for accepting the invitations. Thank them for spending time reading my manuscript and travelling long distances to participate the defense. They asked important questions and gave suggestions for the manuscript improvement. Meanwhile, I would like to thank Mr. Thierry Faug, Franck Bourrier, Bruno Chareyre for their participations of my two committee of the thesis. They helped me a lot improve my work during the studies. Particularly thanks to Thierry and Franck, my presentation skills have been improved a lot.

Third, I would like to thank my dear colleagues of Irstea laboratory: Nejib Hadda, Adel Albaba, Raphael Maurin, Nguyen Nho Gia Hien, Pascal Hagenmuller, Francois Kenib, etc. They helped me a lot during our scientific discussions. Besides, thank colleagues: Philomenon, Bel Coraline, Estelle, Isabelle et Fed Ousset, etc, for being very kind to me. They welcome me to join them and give me opportunity to feel their attitudes towards life.

In the end, I would like to thank my dear friends: Gilles Nicolet, Zhun Mao, Huaxiang Zhu, for their friendships and their encouragements. They helped me a lot during the hard times. Besides, I also thank my friends Wentao Cheng, Chao Quan, Meina Chang, Xiaoxiu Li, kai Wu, Chenggang Wang, zhenzhen Liu, etc. They make my life to be very colorful during my studies.

# Abstract

The prediction of boulder trajectory and the design of protection structures are particularly two main interests of rockfall engineering. The prediction of boulder trajectory largely depends on the bouncing of the boulder, and the design of protection structures, such as embankments, is closely related to the impact force directed by the boulder.

In this context, the thesis deals with the interaction between a falling boulder and a granular medium through numerical modelling based on a discrete element method. The objective of the thesis is to identify and quantify the mechanisms that govern the bouncing of boulder and the load transfer inside the impacted medium. The manuscript consists of three parts: DEM modelling of the impact process, global bouncing of the boulder and micromechanical behaviour of the impacted medium.

The boulder is modelled as a single sphere with an incident velocity, the medium is modelled as an assembly composed of poly-disperse spherical particles. An elastic-plastic contact law implemented with rolling resistance to consider particle shape effects is used to model the dynamic impact process. The numerical impact modelling is validated by comparison with experimental results from literature in terms of impact force, impact duration, penetration depth.

Bouncing of the boulder is investigated together with energy propagation processes inside the impacted medium. Investigation shows that impact induces the increase of elastic strain energy inside the medium which is followed by a fluidization process characterized by the increase in kinetic energy and energy dissipation, as well as the decrease in coordination number. Boulder's bouncing occurrence considering various boulder size and medium thickness obtained based on 3D simulations shows that three impact regimes exist, which is consistent with the results of Bourrier et al. (2008). In addition, shifts of bouncing occurrence curves exist between 2D and 3D impact cases due

to the different strength and energy dissipation properties of 2D and 3D mediums during the impact loading. Based on the two aspects of investigation, the relation between the bouncing of boulder and the energy propagation within the impacted medium is discussed.

The behaviour of the impacted medium is investigated from a micromechanical point of view. The force chain network in the impacted medium is characterized based on particle stress information. The aim is to find the role of force chains in the strength and the microstructure evolution of the medium. Investigation of the impact force on the boulder by impacting samples composed of different grain sizes shows that sample composed of big grains result in a larger impact force, longer force chains with respect to the medium thickness, and large percentage of long age force chains. In addition, the spatial and temporal distribution of force chains are investigated. The results show that the strength of the medium under impact is contributed by chain particles located between the boulder and the bottom boundary, force transmission in the lateral direction of the medium plays a secondary role. Moreover, the investigation of force chain buckling mechanisms indicates that, triggered by the relative movements between the chain particles, the increase of buckling number is related to the decrease of impact force on the boulder as well as the increase of kinetic energy and energy dissipation within the medium.

**Keywords**: Impact, granular material, rockfall, discrete element modelling, bouncing, force chain, energy dissipation.

# Résumé

La prédiction de trajectoire des blocs et la conception de structures de protection sont deux questions importantes de l'ingénierie des chutes de pierres. La prédiction de la trajectoire d'un bloc dépend en grande partie des rebonds de ce bloc tandis que la conception de structures de protection, comme les merlons, est étroitement liée à la force d'impact sur le bloc.

Dans ce contexte, la thèse traite de l'interaction entre un bloc qui tombe et un milieu granulaire en utilisant une modélisation numérique par la méthode des éléments discrets. L'objectif de la thèse est d'identifier les mécanismes qui contrôlent le rebond du bloc et le transfert d'effort dans le milieu impacté. Ce travail s'articule autour de trois grands axes: la modélisation DEM du processus d'impact, le rebond du bloc et le comportement micromécanique du milieu impacté.

Le bloc est modélisé par une unique sphère avec une vitesse incidente tandis que le milieu est modélisé par un assemblage de particules sphériques poly-disperses. La loi de contact élastique-plastique, avec une résistance au roulement pour considérer les effets de forme des particules, est utilisée pour modéliser le processus d'impact. La modélisation numérique de l'impact est validée par des comparaisons avec des résultats expérimentaux issus de la littérature en termes de force d'impact, de durée d'impact et de profondeur de pénétration.

Le rebond du bloc est examiné en s'appuyant sur les processus de propagation d'énergie dans le milieu impacté. L'étude montre que l'impact provoque l'augmentation de l'énergie de tension élastique à l'intérieur du milieu qui est suivie par un processus de fluidisation caractérisé par l'augmentation d'énergie cinétique et la dissipation d'énergie ainsi que par la diminution du nombre de coordination. L'occurrence du rebond du bloc obtenue avec des simulations 3D en considérant plusieurs tailles de bloc et plusieurs

épaisseurs du milieu montre que trois régimes d'impact existent, ce qui est en accord avec les résultats obtenu par Bourrier et al. (2008). De plus, il existe des différences entre les diagrammes d'occurrence de rebond 2D et 3D en raison de résistances et de propriétés de dissipation d'énergie différentes. En se basant sur les deux aspects de l'étude, la relation entre le rebond du bloc et la propagation d'énergie dans le milieu est discutée.

Le comportement du système impacté est examiné d'un point de vue micromécanique. Le réseau de chaînes de force dans le milieu impacté est caractérisé à partir des contraintes moyennes au sein des particules. L'objectif est d'identifier le rôle des chaînes de force dans l'évolution de la résistance et de la microstructure du milieu. L'étudiant de la force d'impact sur le bloc avec des impacts sur des échantillons de grains de tailles différentes montre que l'échantillon composé de grains de taille importante induit une force d'impact plus élevée, des chaînes de force plus longues comparées à l'épaisseur du milieu ainsi qu'un pourcentage important de chaînes de force avec une longue durée de vie. De plus, l'étude de la distribution spatiale et temporelle des chaînes de force montre que la résistance du milieu pendant l'impact est due aux particules des chaînes situées entre le bloc et la frontière inférieure du milieu impacté et que la transmission des forces dans la direction latérale joue un rôle secondaire. Enfin, l'étude des mécanismes de flambage des chaînes de force indique que, induit par les mouvements entre les particules de la chaîne, l'augmentation de nombre d'éffondrement est liée à la diminution de la force d'impact sur le bloc ainsi qu'à l'augmentation d'énergie cinétique et de la dissipation d'énergie au sein du milieu.

**Mots-clés** : Impact, matériau granulaire, chute de blocs, modélisation par éléments discrets, occurrence de rebond, rebond, chaîne de force, dissipation d'énergie.

# Abbreviations

| | |
|---|---|
| $BN$ | Number of buckling chain segments |
| $dF_n$ | Incremental normal contact force |
| $dF_s$ | Incremental shear contact force |
| $d_m$ | Mean diameter of grains |
| $E_d$ | Total energy dissipation |
| $E_{db}$ | Energy dissipation due to bending |
| $E_{ds}$ | Energy dissipation due to sliding |
| $E_{dtw}$ | Energy dissipation due to twisting |
| $E_k$ | Kinetic energy of the medium |
| $E_{kb}$ | Kinetic energy of boulder |
| $E_{mgh}$ | Gravity potential energy |
| $E^n$ | Local normal modulus |
| $E^s$ | Elastic strain energy |
| $E_t$ | Total energy of the system |
| $F_{boul}$ | Impact force on the boulder |
| $F_n$ | Normal contact force |
| $F_s$ | Shear contact force |
| $g(r)$ | Radial distribution function |
| $H$ | Medium thickness |
| $HDCD$ | Homogeneously distributed chain domain |
| $InE_d$ | Incremental of total energy dissipation |
| $L$ | Medium length |
| $l_{chain}$ | Mean length of chain |
| $l_{HDCD}$ | Critical length of $HDCD$ |
| $\max F_{boul}$ | Maximum value of Impact force on the boulder |

| | |
|---|---|
| $\max \Delta F_{bott}$ | Maximum incremental transmitted force on the bottom boundary |
| $pv$ | p-value for chi-square test |
| $\overline{pv}$ | Mean value of $pv$ |
| $R_b$ | Radius of boulder |
| $R_m$ | Mean radius of grains |
| $T_{imp}$ | Impact duration |
| $V_{boul}$ | Vertical velocity of the boulder |
| $Z_{boul}$ | Penetration depth of boulder inside the layer |
| $\beta_r$ | Bending stiffness parameter |
| $\beta_{tw}$ | Twisting stiffness parameter |
| $\Delta F_{bott}$ | Incremental transmitted force on the bottom boundary |
| $\Delta t$ | Time step |
| $\sigma_1$ | The major principal stress |
| $\theta$ | Orientation of $\sigma_1$ with the $z$ axis |
| $\theta_b$ | Critical chain buckling angle |
| $\theta_c$ | Chain criterion |
| $\eta_b$ | Rolling elastic limit |
| $\eta_{tw}$ | Twisting elastic limit |
| $\mu$ | Local Poisson's ratio |
| $\rho$ | Mass density |
| $\phi$ | Orientation of $\sigma_1$ with the $x$ axis |
| $\varphi$ | Local frictional angle |

# Contents

# List of Figures

# List of Tables

# Chapter 1

# General introduction

## Contents

## 1.1   Rockfall hazards

Rockfall is one of major risks in mountainous areas. Triggered by the detachment of rock fragments from cliffs, rockfall is an extremely rapid process with potentially long travel distances (Figure 1.1). A specific definition of rockfall is one or several fragments of rock blocks detached by sliding, toppling or falling, that fall along a vertical or sub-vertical cliff, and proceed down the slope by bouncing and flying along ballistic trajectories or by rolling and sliding (Dorren et al., 2011). The carried kinetic energies of rock blocks along their trajectories vary from a few kilojoules to 50,000 kJ or even beyond (Nicot et al., 2007).
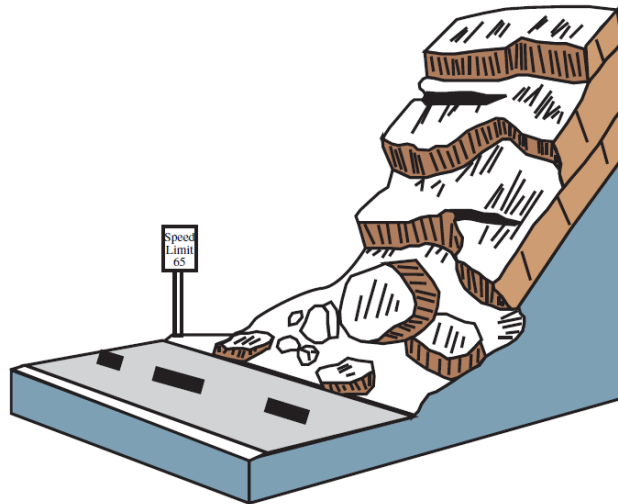


*Figure 1.1:*  *Schematic description of rockfall movement (Highland, 2004)*

Rockfall can cause serious damage to residential areas and infrastructures. For instance, in a beautiful tourist spot of Guilin China, seven tourists were killed during a rockfall event on 19 March 2015 (Figure 1.2(a)). In United States, a rockfall event led to the injury of one motorist and the damage of a roadway on 24 February 2015 (Figure 1.2(b)). In south Tyrol Italy, around 4000 cubic meters of rocks detached from a near vertical rock cliff, the major part of debris consisted of a number of enormous boulders that slid and rolled down the slope before striking a 300 year old building on 21 January 2014 (Figure 1.2(c)). Another example of rockfall event occurred in the Arly Gorge in the French Alps (the road built there is the most expensive one in Europe due to the

protection structures constructed against mountain hazards: rockfalls, landslides, snow avalanches), a car was crushed by a 20-tonne boulder in February 2012 (Figure 1.2(d)). Moreover, due to the warming trends in world climate which have a significant influence on mountain permafrost and destabilize rockfall starting zones, more and more rockfall events are expected to occur (Kenner et al., 2011; Einhorn et al., 2015).



(a)

(b)

(c)

(d)
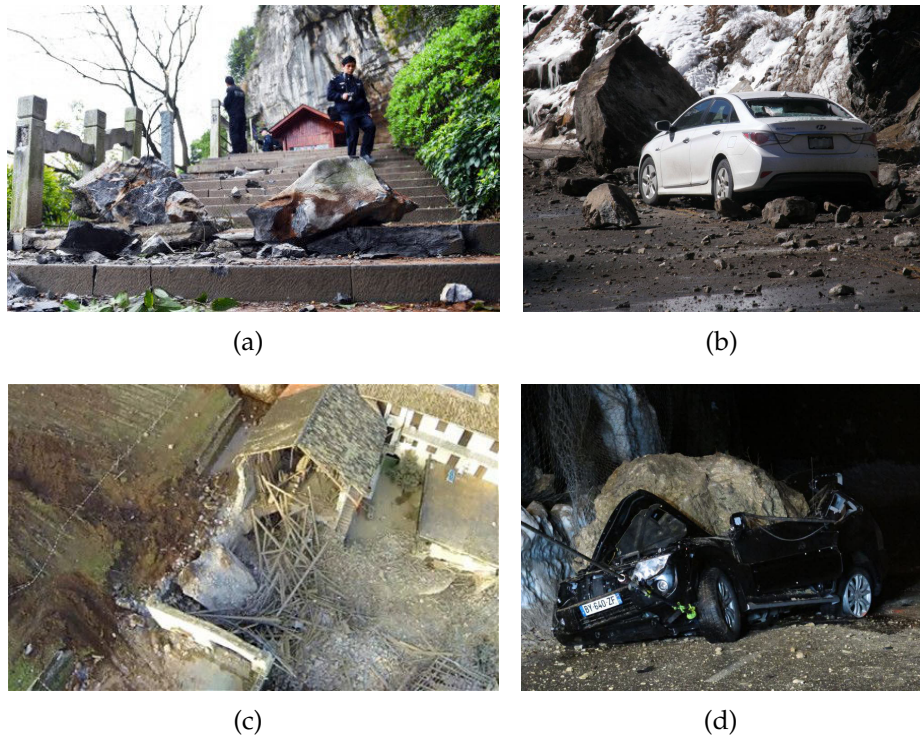
*Figure 1.2:* *Examples of rockfall events occurred in: (a) Guilin China, (b) United States, (c) Tramin Italy, (d) Arly Gorge in the French Alps*

## 1.2 Engineering expectations

Characterized by its rapid process, the occurrence of rockfall events is difficult to predict, while it is possible to reduce the damage by risk assessment and protection structure design. Rockfall engineering in particular concerns two interests: the prediction of boulder trajectory and the design of protection structures.

### 1.2.1 Trajectory predictions

The prediction of rockfall trajectories is of crucial importance in rockfall engineering. It is used not only for rockfall hazard assessment and hazard zoning, but also for the design of rockfall mitigation structures. Both of the two engineering expectations have high requirements upon the trajectory predictions (Evans and Hungr, 1993; Chau et al., 2002; Dorren et al., 2006; Peila et al., 2007; Ronco et al., 2009; Peila, 2011; Dorren et al., 2011; Volkwein et al., 2011; Lambert and Bourrier, 2013).
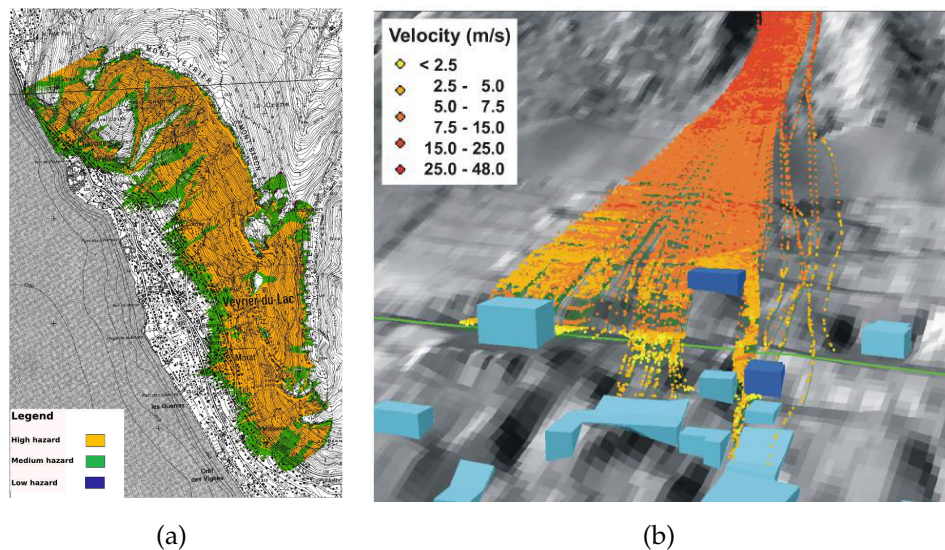


*Figure 1.3:* *(a) Rockfall hazard zoning (Irstea, F. Berger),(b) Simulations of rockfall trajectories near a residence area(Agliardi et al., 2009)*

Generally, rockfall hazard assessment and trajectory predictions would require evaluating the temporal probability and the spatial susceptibility of rockfall events, the 3D trajectory and maximum run-out distance of falling blocks as well as the distribution of rockfall intensity at each location and along each falling path (Figure 1.3). Particularly, the hazard mapping for defining levels of hazards taking into account both rockfall occurrence frequency and the kinetic energy of boulder allows to improve the hazard assessment accuracy (Figure 1.3(a) and 1.3(b)). The design of rockfall mitigation structures is based on an estimation of the size of the rockfall as well as the kinetic energy level of the boulder at the location where the mitigation device is to be installed.

## 1.2.2    Protection structure design

Based on the knowledge of rockfall risk assessment and trajectory analysis, rockfall mitigations which include active and passive protection systems can be carried out. Active protection systems (Figure 1.4(a)) are designed to avoid rockfalls from occurring, while passive protection structures are designed to protect at-risk structures from the rockfall event. The most commonly used passive protection structures include flexible fences and barriers (Figure 1.4(b)), rockfall galleries and rock sheds (Figure 1.4(c)), embankments (Figure 1.4(d)). The choice between different protection strategies depends on the site topography and the impact energy of falling boulders.



|     |     |
| --- | --- |
| (a) | (b) |
| (c) | (d) |
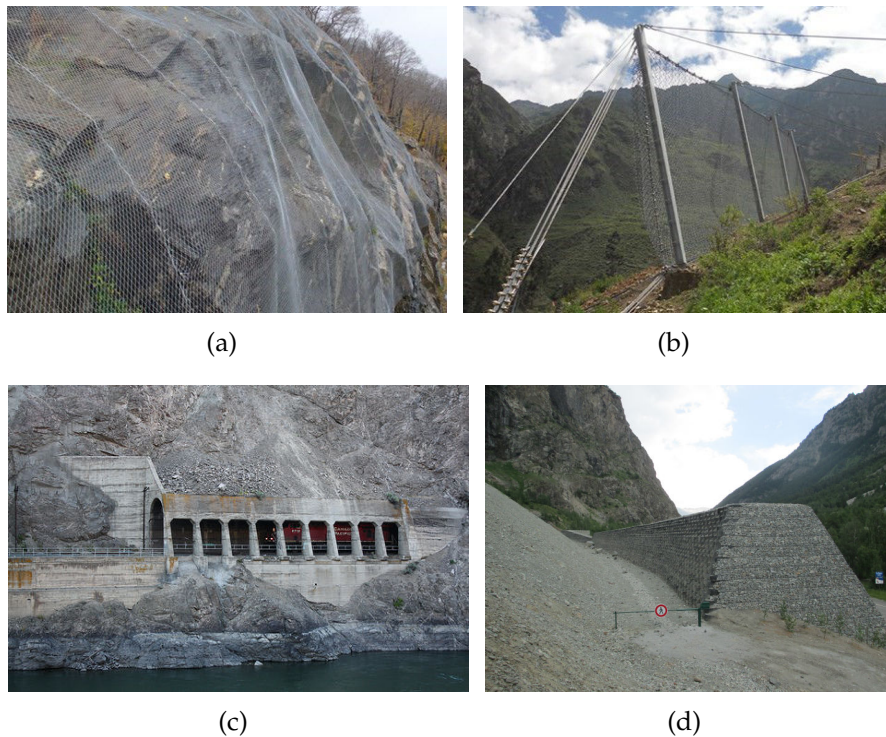
*Figure 1.4:* *(a) Rockfall protection drapes (from Geobrugg company), (b) Rockfall protection barriers (from Geobrugg comany), (c) Railways protected by rock sheds, (d) Rockfall protection embankment (Irstea, S. Lambert)*

In general, the sheltering structures (rock sheds or galleries) devoted to the protection of roads and railways against rockfalls consist of a reinforced concrete roof-plate supported by a bearing structure (Figure 1.4(c)). The roof-plate is usually covered by a cushion layer to attenuate the impact force of rockfall and diffuse transmitted impact

stress side the concrete plate. The current engineering practice consists in using on-site material as cushion layer, sand or other 'specific' materials are marginally used (Calvetti et al., 2005).

Apart from rockfall sheltering structures, embankments have shown to be an efficient way of protecting areas where the falling blocks have volumes or velocities large enough to break through the net fences, or where frequent rockfall events have to be faced within a short interval of time (Lambert and Bourrier, 2013). Different types of embankments made of natural compacted soil, huge rock blocks, gabions or reinforced ground are used in rockfall engineering. The embankments should have the abilities of controlling block's trajectory and resisting against the impact force of the boulder. In addition, embankments are usually associated with catching ditches made of loose materials to dissipate the block's energy (Figure 1.4(d)).

## 1.3 The role of impact in rockfall predictions and mitigations

The trajectory prediction particularly depends on the bouncing of boulder. The design of protection structure relies on the impact force and the transmitted force inside the granular medium which are sometimes used to estimate the stress within the protection structures and verify the deformation and the stability of the structures (Labiouse et al., 1996; Pierson et al., 2001; Peila et al., 2007; Schellenberg, 2009; Peila, 2011; Lambert and Bourrier, 2013).

Both the trajectory prediction of boulder and the design of the protection structures are related to the interaction of a boulder and a granular medium. This medium can represent either natural or man-made soils, covering the slope or constituting protection structures. This boulder-medium interaction issue is of paramount importance for governing the bouncing of the boulder and the response of the protection structure. Therefore, this boulder-medium interaction issue is important not only for conducting rockfall trajectory predictions, but also for defining optimum protection strategies and design protection structures.

The impact of a boulder on a granular medium is characterized by rapid loading and unloading, large deformations, rapid energy exchange and compression wave propagation process (Makse et al., 2004; Crassous et al., 2007). The boulder-medium interaction is a very complex process which depends not only on the mass, shape, velocity of boulder, but also on the characteristics of the granular medium such as stiffness, density, porosity, medium thickness (Ciamarra et al., 2005; Bourrier et al., 2008; Pacheco-Vázquez et al., 2011; Kondic et al., 2012). The bouncing and the design of protection structures therefore require well taking into account the complex mechanisms that are working during the impact.

However, for either the design of protection structures or the bouncing of a block, the current investigation approaches dealing with the boulder-medium interaction have limitations. The analytical models were calibrated based on global measurements obtained in specific impact and boundary conditions. These models are limited to these specific cases and cannot be generalized, due to the lack of sufficient knowledge of the mechanisms actually occurring in the granular material during the impact. Meanwhile, these models are most often based on strong assumptions which also limit their reliability. Numerical models calibrated based on experiments are relevant for predicting the bouncing and the impact force on the boulder. However, numerical modelling does not sufficiently go deep enough to address the micromechanisms that govern the bouncing of the boulder and the response of the granular medium. Therefore, research-based investigations of a boulder impacting a granular medium to well understand the mechanisms that govern the bouncing of the boulder as well as the response of the granular medium are required.

## 1.4    Objectives and contents of the thesis

This thesis addresses the boulder-medium interactions from both global and micromechanical points of view through numerical modelling approach. The objective is to identify and quantify the mechanisms involved in load transfer in the neighbourhood of the impact and to estimate their consequences on the global response of the granular layer. The investigations mainly focus on the bouncing of the boulder and the micromechanical load transfer inside the impacted medium.

The work of the thesis includes (Figure 1.5):

Chapter 2, State of the art reviewing researches concerning rockfall impact reported in the literature. The important issue is interaction between a boulder and a granular medium, including the bouncing of the boulder on a granular medium. In addition, micromechanical properties of the granular material are important issue that controls the response of the granular medium during the impact. In the end, numerical modelling based on a discrete element method is introduced.

Chapter 3, DEM modelling of the impact process by adopting rolling resistance in the contact law to model the particle shape effects. The contact parameters will be calibrated based on quasi-static triaxial tests of angular Ticino sand. This sand is chosen since it can be used to represent the soil composing the slopes or rockfall protection structures. The impact simulation will be validated by comparison with experimental results from literature.

Chapter 4, Investigation of the global bouncing of the boulder on the medium. First of all, effects of the local configuration are investigated, a specific number of simulations is shown to be sufficient to capture the average impact force and reflect velocity of boulder. Second, elastic strain and kinetic energy propagation inside the medium is quantified in order to investigate the relation between energy processes within the specimen and the rebound of he boulder. Third, the bouncing occurrence diagrams are investigated by fixing the grain size while varying the boulder size and the medium thickness. The studies permit to better quantifying the bouncing of boulder in 3D context, which can be useful for improving the prediction of the boulder trajectories.

Chapter 5, Investigation of the micromechanical behaviour of the impacted medium from a micromechanical point of view. The aim is to give the macroscopic behaviour of the impacted medium a micromechanical explanation. First, force chain network inside the impacted medium is characterized based on particle stress information. Second, impacts of boulders on granular mediums composed of different grain sizes are investigated. Third, the spatial and temporal distribution of force chains are investigated. Finally, studies are conducted to investigate the buckling mechanism of force chains and its relation with impact force and energy items. The investigations indicate that force

chains play a fundamental role in governing the impact force on the boulder as well as the microstructure strength of granular medium. The micromechanial features allow to better serve the design of protection structures.

Chapter 6, Conclusions and perspectives.
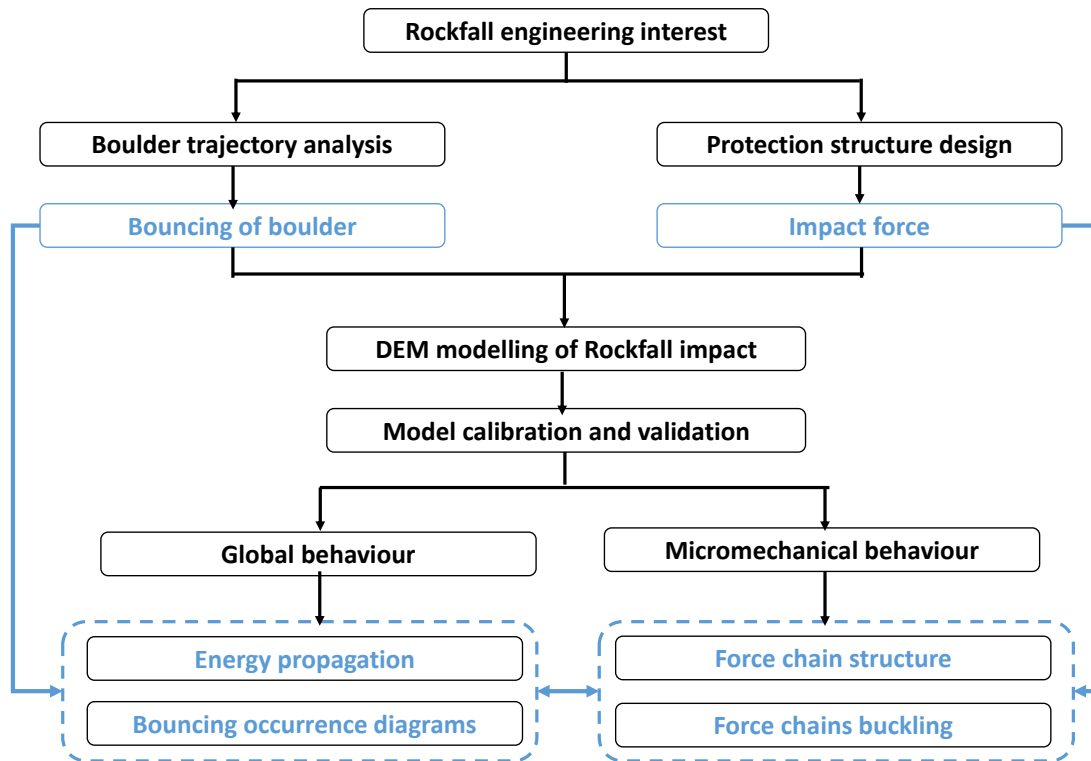


***Figure 1.5:*** *Schematic description of the thesis structure*

# Chapter 2

# State of the art

## Contents

Studies have been reported in the literature to understand the boulder-medium interaction mechanisms by analytical models (e.g. Pichler et al., 2005), experiments (e.g. Stoffel, 1998; Calvetti et al., 2005; Plassiard et al., 2009; Plassiard and Donzé, 2009) or numerical simulations (e.g. Calvetti et al., 2005; Bourrier et al., 2008, 2010). This state of the art particularly reviews the studies concerning the interaction between a falling boulder and a granular medium, including the bouncing of a boulder on a granular medium.

## 2.1 Interaction between a boulder and a granular medium

### 2.1.1 Engineering practices

Design engineers adopt easy-to-use expressions to estimate the impact force, impact duration and block penetration. The principal parameters of the expressions include:

— $M$: Boulder mass [kg];
— $W$: Boulder weight [kN];
— $R$: Boulder equivalent radius [m];
— $V_i$: Impact velocity of the boulder [m/s];
— $H_c$: Falling height of the boulder [m];

— $\varphi$: Internal friction angle of the medium [°];
— $\nu$: Poisson's ratio of the medium [-];
— $\rho$: Density of the medium [kg/m$^3$]
— $\gamma$: Unit weight of the medium [kN/m$^3$];
— $e$: Medium thickness [m];
— $M_E$: Static compression modulus of the medium [kN/m$^2$];
— $g$: Gravity acceleration [9.81 m/s$^2$];

— $T_{imp}$: Impact duration [s];
— $P$: Dynamic impact force [kN];
— $P_{max}$: Maximum impact force [kN];
— $P_{int}$: Transmitted force on the bottom [kN];
— $Z$: Penetration depth of the boulder [m];

### 2.1.1.1 Chinese design codes

Strictly speaking, Chinese design codes do not include specific sections dealing with the calculation of rockfall impact force, however, the impact force can be calculated following suggestions from "Specifications for design of highway subgrades" (JTJ013-95, 1995) and "Technical design manual for railway engineering" (China railway eryuan engineering group, 1995).

In JTJ013-95 (1995), the dynamic impact force is calculated as:

$$P = P(Z)S = 2\gamma Z(2\tan^4(45° + \frac{\varphi}{2}) - 1)S \tag{2.1}$$

$$Z = V_i \sqrt{\frac{W}{2\gamma g S} \times \frac{1}{2\tan^4(45° + \frac{\varphi}{2}) - 1}} \tag{2.2}$$

where $P(Z)$ is the unit resistance of the medium, $S$ is rockfall equivalent spherical cross sectional area.

In the "Technical design manual for railway engineering", the dynamic impact force is calculated as:

$$P = \frac{WV_i}{g\, T_{imp}} \tag{2.3}$$

$$T_{imp} = \frac{2e}{c} \tag{2.4}$$

$$c = \sqrt{\frac{1-\nu}{(1+\nu)(1-2\nu)} \times \frac{M_E}{\rho}} \tag{2.5}$$

where $c$ is the compression wave velocity inside the medium [m/s].

The impact force calculated by these two expressions are actually average impact force instead of the maximum impact force. The underestimation of the impact force might result in structural failure when subjected to impact (Ye et al., 2010). Therefore, new design codes fairly capturing the maximum impact force should be proposed.

### 2.1.1.2 Swiss design codes

Swiss federal roads office proposed to calculate the impact force $P$ and the penetration depth $Z$ in the case of a boulder impacting a granular medium resting on a rigid slab (ASTRA, 2008):

$$Z = \frac{MV_i^2}{1000P} \tag{2.6}$$

$$P = 2.8e^{-0.5}R^{0.7}M_E^{0.4} \tan \varphi \, (\frac{MV_i^2}{2000})^{0.6} \tag{2.7}$$

$$A_d = CP \tag{2.8}$$

where $A_d$ is the static equivalent force transmitted on the bottom slab [kN], $C$ is the construction coefficient whose value depends on the rupture mode of the slab.

The approach of considering a statically equivalent load for assessing the stability of the structure may not be fully appropriate. The main reason is that this approach neglects some mechanisms that work during the impact and govern the actual response of the whole structure.

### 2.1.1.3 Japanese design codes

Based on experimental data and the elastic Hertz contact theory, Japanese road association proposed to calculate the impact force as (Kawahara and Muro, 2006):

$$P = 2.108 \, (1000M)^{(2/3)} \, \lambda^{0.4} \, H_c^{0.6} \tag{2.9}$$

where $\lambda$ is the Lamé coefficient of the medium [kN/m²], the most often used value of $\lambda$ is 1000 kN/m².

This expression is proposed for the aim of rockfall protection structure design. It is assumed that the rockfall is a rigid sphere having a specific gravity of 2.65 (Kawahara and Muro, 2006). This expression allows to obtain more realistic impact force, but the effects of medium thickness, impact angle are not considered.

Even though these expressions are very simple to use from a practical point of view, they are obtained from rough analytical estimations or drawn from specific experimental results. Without considering the detail mechanics that govern the interactions between the boulder and the medium, these expressions might be inappropriate for some impact cases.

## 2.1.2  Experimental investigations

Experimental investigations of boulder-medium interaction are usually conducted in small scales, half scales, or in few cases in real scales, associated with small or big boulder incident kinetic energies. Impact experiments deal with various impact problems and impact conditions. For instance, boulder impacts on natural or man-made slopes, rockfall shelters, embankments of simple and complex configurations (e.g. Labiouse et al., 1996; Stoffel, 1998; Calvetti et al., 2005; Pichler et al., 2005; Peila et al., 2007; Peila, 2011). Measurements are set in experiments to record the acceleration of boulder, the penetration depth of the boulder, the impact time, the stresses within the granular medium. The obtained experimental results were used for improving rockfall protection structure design.

Most part of the work concerns the response of a granular layer covering a rigid structure, for the case of a boulder impacting a rock shed. Labiouse et al. (1996) conducted half-scale impact experiments of a boulder impacting a granular layer covering a concrete slab. The size of the slab is 3.2 m $\times$ 3.2 m $\times$ 0.2 m (Figure 2.1). Four essential parameters influencing the design of rock shed structures were investigated: weight of blocks (100, 500, 1000 kg), falling height (0.25 to 10 m), cushion thickness (0.35, 0.5, 1.0 m) and material of the soil cushion (three different soils). Empirical expressions are proposed based on experimental results:

$$P_{max} = 1.765 \, M_E^{0.4} \, R^{0.2} \, W^{0.6} \, H_c^{0.6} \tag{2.10}$$

In addition, Stoffel (1998) conducted similar experiments as Labiouse et al. (1996) and proposed expressions to calculate impact force, transmitted force and penetration depth during a boulder impacting a granular medium:

$$P_{max} = 1.33 \exp(\frac{R}{1.5e}) \, M_E^{\frac{1}{3}} \, (\tan \varphi)^{0.2} \, E_{pot}^{\frac{2}{3}} \tag{2.11}$$
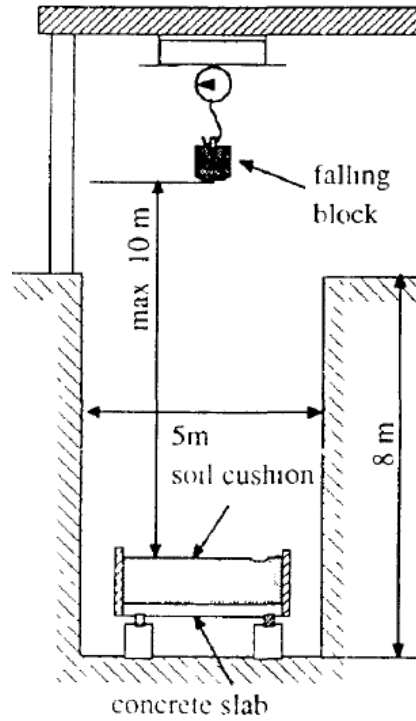
*Figure 2.1: Impact test devices (Labiouse et al., 1996)*

$$P_{int} = 2.6\, R^{-0.24}\, e^{-0.01} \exp\left(\frac{R}{2.5e}\right) M_E^{0.25}\, E_{pot}^{0.75} \tag{2.12}$$

where $P_{int}$ is the maximum transmitted force on the bottom, $E_{pot}$ is the potential energy of the boulder.

In case of a boulder impacting a medium resting on a rigid wall, the expression is:

$$P_{max} = 1.35\, R^{0.2} \exp\left(\frac{R}{3e}\right) M_E^{0.4}\, (\tan \varphi)^{0.2}\, E_{pot}^{0.6} \tag{2.13}$$

Calvetti et al. (2005) investigated experimentally the phenomenon of boulder impact-ing granular soils typically used to reduce loads on shelters. Series of full scale tests were performed to investigate the influence of geometrical and mechanical properties of the medium, as well as the effects of previous impacts (so as Stoffel (1998)). Experimental

results of Calvetti et al. (2005) show that relative density of the superficial layers of the stratum is the key factor that determines the peak value of impact force, while the inclination of the stratum plays a less significant role.

Both the experimental results of Stoffel (1998) and Calvetti et al. (2005) proved that the impact force transmitted to the rigid bottom from the impacted granular medium is much larger than the impact force on the boulder, with a ratio of 1 to 3. This ratio is inversely proportional to the layer thickness. The existence of a larger value of transmitted force on the bottom than the impact force is called dynamic effects. This phenomenon is also observed in numerical simulations (Calvetti et al., 2005). In addition, the propagation of compression waves within the medium is governed by the mechanical properties of the granular material (Calvetti et al., 2005). For a given impact, the impact force and the speed of compression waves in the granular soil are mainly affected by the elastic properties of the soil.

Pichler et al. (2005) designed real-scale experiments based on analytical relations, the corresponding results were used to conduct back-analysis to obtain the indentation resistance of gravel. This permits to estimate of penetration depths caused by rockfall events which are beyond the experimental acceleration measurements. In addition, small scale laboratory experiments of Degago et al. (2008) showed that the hemispherical impactor induced higher impact force as well as less penetration as compared to the pyramidal impact boulder.

Gerber and Volkwein (2010) conducted 54 tests with two different concrete boulders (800 kg and 4000 kg) dropped on two ground layers (0.5 m and 1.3 m). The deceleration curves show either two significant local maximum accelerations or one maximum and a plateau-like behaviour. The observations illustrated the importance of compaction in the ground layer, which is consistent with the conclusion drawn by Lorentz et al. (2006) that layer compactness has a major effect in increasing the peak value of the transmitted impact force. The results of the 4000 kg block tests show a correlation between the penetration $Z$ and the maximum deceleration $a_{max}$, which can be shown simply as:

$$\begin{cases} P_{max} = 1000M\dfrac{V_i}{T_{imp}}c \\[2ex] Z = \dfrac{V_i T_{imp}}{c} \\[2ex] a_{max} = \dfrac{V_i^2}{Z} \end{cases} \qquad (2.14)$$

where $c$ is a constant value.

### 2.1.3  Numerical modelling

An alternative approach for studying the impact mechanisms is through numerical modelling. Plassiard and Donzé (2009) modelled the impact process of a boulder on a granular medium with a discrete element method. Both quasistatic and dynamic behaviours of soil have been examined and additional contact laws were used to be representative. The impact corresponded to a 500 kg boulder hitting a 50 cm thick layer of a compacted soil, with a falling height of 10 meters. The impact force was well reproduced, while the transmitted force through the granular medium was less well modelled even with the introduction of additional dissipation laws (Figure 2.2).
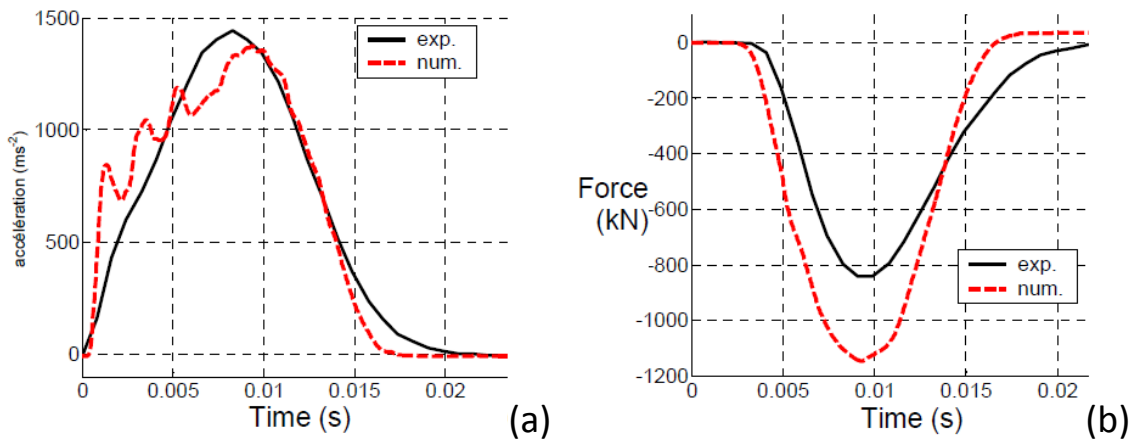


**Figure 2.2:** *Time evolution of (a) the deceleration of the boulder, (b) the force transmitted to the bottom (Plassiard and Donzé, 2009)*

Calvetti et al. (2005) performed numerical simulations with the aim of investigating loading conditions characterised by different values of stratum thickness under a wide range of impact energy. A simplified DEM model of the experimental set-up is established, the stratum is represented by a 2 m thick assembly of about 10000 spheres with uniform diameter distribution between 0.1 and 0.3 m. The results of the numerical simulations show that the peak value of impact force may be conveniently correlated to impact energy (Figure 2.3(a)), although a more refined approach should consider the individual effects of boulder mass and falling height. In addition, for a given impact force, the stresses on the plate decrease with the thickness of the stratum. A linear correlation between impact force and stresses on the plate was proposed to describe the dynamic amplification effect that characterised the wave propagation within the stratum (Figure 2.3(b)).
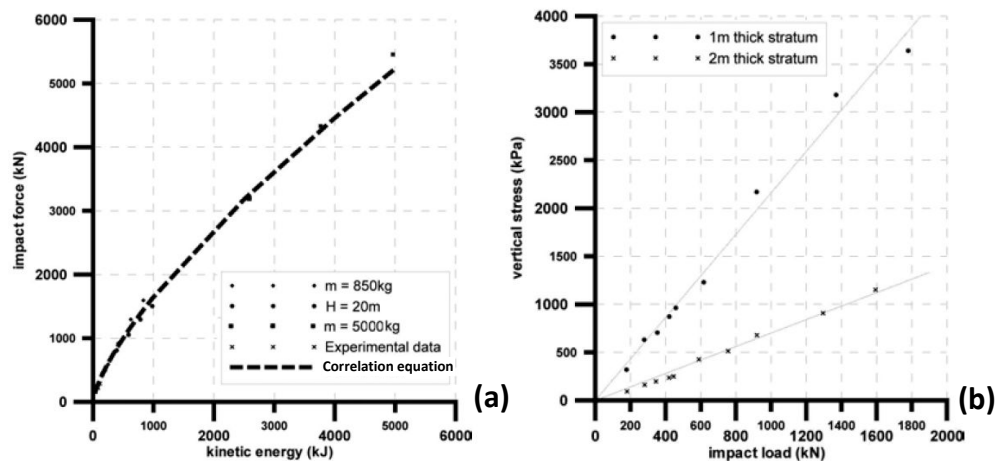


**Figure 2.3:** *(a) Impact force as a function of impact energy; (b) Stresses on the plate as function of impact force (Calvetti et al., 2005)*

## 2.2   Bouncing of a boulder on a granular medium

Among the motions of boulder (free falling, sliding, rolling, and bouncing) along the trajectory down the slope, bouncing, occurring when the falling block collides with the slope surface, is the most difficult one to predict (Dorren, 2003; Labiouse and Heidenreich, 2009). Theoretically, the motion of boulder during the interaction can be calculated

according to Newton's second law. However, the interaction is a very complex process, the force on the boulder, the contact points or surfaces evolves with time depending on the substrate properties, rock properties and the kinematics of the boulder before the impact. The use of computer programs in rockfall simulations is one of the most popular approaches for accounting for the bouncing of a boulder on a granular medium (Prisco and Vecchiotti, 2006; Bourrier et al., 2009; Lambert et al., 2013).

## 2.2.1 Experimental investigations

Most computer codes model the bouncing simply by adopting one or two restitution coefficients which are obtained by analytical, back-analysis, experimental and numerical modelling results (Wong et al., 2000; Nouguier-Lehon et al., 2003; Heidenreich, 2004; Oger et al., 2005, 2008; Bourrier and Hungr, 2011; Vijayakumar et al., 2011). The trajectory simulations are very sensitive to these restitution coefficients, and the accuracy of the simulations depends to a large extent on these parameters (Dorren et al., 2011).
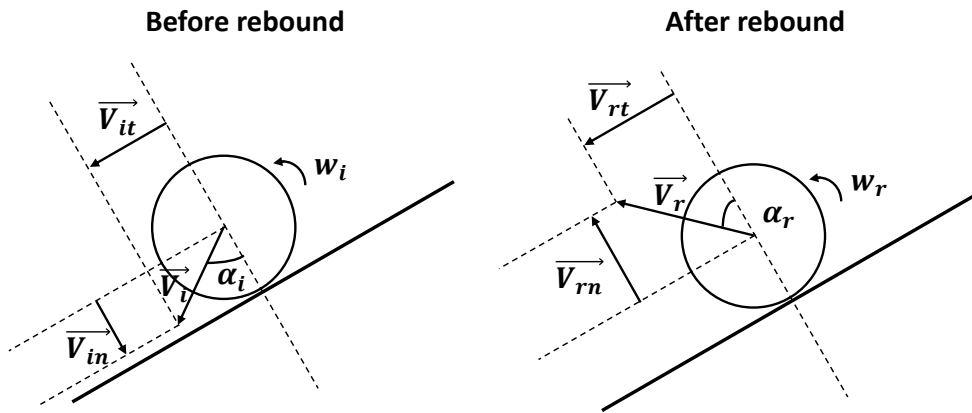


*Figure 2.4: Definition of incident (left) and rebound velocity components (right) for the rebound*

The most commonly used restitution coefficients are expressed in terms of velocity or energy, indicating the amount of velocity or energy dissipated during the impact (Figure 2.4):

$$R_V = \frac{V_r}{V_i} \tag{2.15}$$

$$R_E = \frac{V_r^2}{V_i^2} \tag{2.16}$$

$$R_n = -\frac{V_{rn}}{V_{in}} \tag{2.17}$$

$$R_t = \frac{V_{rt}}{V_{it}} \tag{2.18}$$

where $V_r$ and $V_i$ are the incident and reflected velocity of the boulder respectively, $V_{in}$ and $V_{rn}$ are the normal components of incident and reflected velocity respectively, $V_{it}$ and $V_{nt}$ are the tangential components of incident and reflected velocity respectively.

Initially, the restitution coefficients are adopted as constant values irrespective the various impact conditions and the properties of boulder. For instance, restitution coefficient used in Rocscience software are originally derived from analytical research results and back-analysis. Afterwards, more researches were conducted to investigate the effects of the properties of the boulder and the medium, as well as the boulder kinematics on restitution coefficients (Wong et al., 2000; Nouguier-Lehon et al., 2003; Heidenreich, 2004; Oger et al., 2005, 2008; Bourrier and Hungr, 2011; Vijayakumar et al., 2011). Table 2.1 lists the parameters that influence the restitution coefficients.

*Table 2.1: Parameters that influence the bouncing of block*

| Substrate properties | | Block properties | |
|---|---|---|---|
| Material properties | Slope characteristics | Block characteristics | Block kinematics |
| Strength | Slope angle | Mass | Translational velocity |
| Rheology | Roughness | Shape | Rotational velocity |
| | Surface fitting | Size | Incidence angle |
| | Thickness | Strength | Orientation |

The restitution coefficients are influenced by the mass of the block (Asteriou et al., 2012, 2013a), the impact velocity (Asteriou et al., 2012, 2013a), the impact angle (Asteriou et al., 2012), the shape of boulder (Chau et al., 1999; Wong et al., 2000). More specifically, the experimental results of Asteriou et al. (2013a) show that the coefficients decrease with both the increase of the block mass and the impacting velocity. The results of Azzoni et al. (1995) shows that there is generally an increase trend in rolling velocity with increase in dimension of the falling blocks, but little relationship between rolling velocity and shape parameter based on experiments conducted on debris slopes. Those studies pointed out that normal impacts result in less rebounds (Labiouse and Heidenreich, 2009). The study

of Chau et al. (1999) found that $R_n$ increases with the angularity of the boulders, a more angular boulder will lead to lower rebound amplitude with rotation, with this induced rotation, the normal rebound velocity is reduced but the tangential velocity is increased (Wong et al., 2000). Experiments emphasize a clear dependency of restitution coefficients on parameters characterizing the kinematics as the impact velocity. The observation of Chau et al. (2002) indicates that $R_n$ increases with the slope angle, while there appears to have no clear correlation between $R_t$ and the slope angle. On the other hand, a very clear increasing trend in the $R_V$ and $R_E$ with slope angle is observed.

Mechanical properties of the boulder are shown to have influence on the restitution coefficients. The results of Asteriou et al. (2013b) shows that the kinematic restitution coefficients $R_E$ increases with increasing hardness and shows also an increasing trend with the uniaxial compressive strength and the tensile strength.

In addition, the study of Wong et al. (2000) found that the restitution coefficients are strongly affected by the elastic modulus of the platform: slopes with smaller value of Young's modulus result in lower restitution coefficients. Azzoni et al. (1995) shows that the restitution coefficient ranges between 0.51 and 0.92 for rock and between 0.32 and 0.65 for debris.

Restitution coefficients that characterize the bouncing of boulder during rockfall events should not be considered as constant. The normal ($R_n$), tangential ($R_t$) and energetic ($R_E$) coefficients of restitution measured during half-scale experimental study range between the following values (Labiouse and Heidenreich, 2009): $R_n$ is between 0.003 to 0.257 (mean value of over all tests is 0.04), $R_t$ is between 0.07 to 1 (the mean value over all tests is 0.48); $R_E$ is between 0.0003 to 0.336 (the mean value over all tests is 0.03).

Although the rough classification of restitution coefficients is relevant from a practical point of view, it is nevertheless not very satisfactory from a scientific point of view. The main limitations of these trajectory models include two aspects. First of all, these restitution coefficients are usually obtained from field tests (Evans and Hungr, 1993; Zhang et al., 2011), by back analysis (Budetta and Santo, 1994) or by analytical estimations (Bozzolo and Pamini, 1986; Azzoni et al., 1995). On one hand, they are just rough estimations. On the other hand, they are usually obtained subjectively based on specific cases and cannot be generalized. Second, the restitution coefficients used in the models are mainly obtained based on global approaches, without detail consideration

of interactions between the boulder and the impacted granular medium. There are not enough investigation linking the restitution coefficients to the soil mechanisms. The bouncing of boulder on a granular medium is still poorly understood.

## 2.2.2   Numerical modelling

Hungr and Evans (1988) divided the existing computer models into two categories: "rigorous" methods and lumped-mass methods. In the lumped mass analysis method, the block is considered to be a simple point with mass and translational velocity, rotational velocity is also considered in some cases. The advantage of lumped mass analysis method is the high efficiency in calculation and limited number of parameters to be calibrated. However, the parameters of such models are not very reproducible from one test site to another, besides, the model should be well calibrated by back-analysis method before being used for a given site (Bourrier and Hungr, 2011). In the "rigorous" models, the size and shape of the blocks are assumed to be known "a priori" and all the block movements, including those involving the block rotation, are considered (Stoffel, 1998; Descoeudres et al., 1999; Bourrier and Hungr, 2011).

Among the "rigorous" modelling dealing with the bouncing of boulder, Bourrier et al. (2008, 2010) conducted simulations to investigate the energy propagation process inside the granular medium subjected to a normal projectile impact based on a 2D discrete element method. The interactions between particles are governed by a contact model based on an approximation of the Hertz-Mindlin theory with the consideration of only frictional energy dissipation.

In order to characterize energy propagation, the evolution of all energy items during the impact process are observed on concentric crowns centred around the impact point. The concentric crowns are located at distances $h$ from the impact point with a layer thickness of approximate 3 particle diameters (Figure 2.5). The micromechanical process occurring inside the impacted granular medium were investigated in short and long durations.
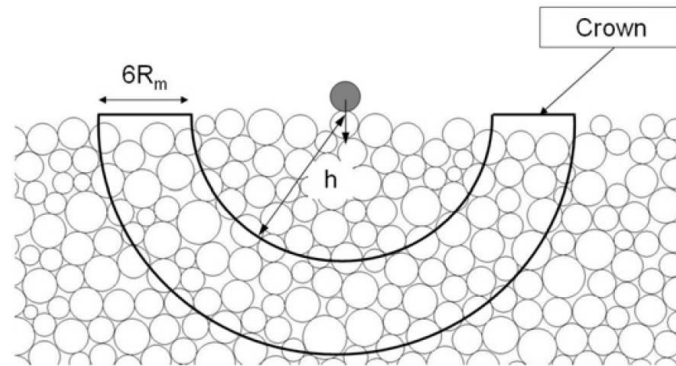
*Figure 2.5: Concentric crown (Bourrier et al., 2010)*

The investigation shows that impact process starts with the partial energy exchange from the impacting boulder to the soil. This phase is followed by the propagation of a compression wave from the impact point to bottom wall of the sample. The initial stage can be divided into two successive phases: a compression phase associated with a local strain energy peak on the central crown, a restitution phase inducing a kinetic energy peak near the impact point. A second energy exchange from soil particles to the impacting particle can occur if the reflected wave reaches the soil surface before the end of the impact. The bouncing of the boulder is related to this second energy exchange.

In addition, Bourrier et al. (2008) conducted extensive 2D numerical simulations and a boulder bouncing occurrence diagram was obtained (Figure 2.6). The local bouncing occurrence criterion is the change in the impacting particle's vertical velocity sign after the interaction with the soil. The global bouncing criterion is defined as a percentage of local bouncing occurrences for varying impact points and fixed incident conditions. The diagram indicates that the rebound of boulder depends not only on the size of the boulder itself, but also on the medium thickness. By dividing the $(H, R_b)$ plane into rebound and non-rebound domains, three impact regimes are observed (Figure 2.6):

- For a small boulder (regime I), bounce occurs for any sample height;
- For a medium size boulder (regime II), bounce does not occur in all cases, the curve decreases as $R_b$ increases;
- For a big boulder (regime III), on the contrary, the curve increases as $R_b$ increases.

In addition, boulder always rebounds if $H$ and $R_b$ are sufficiently small.
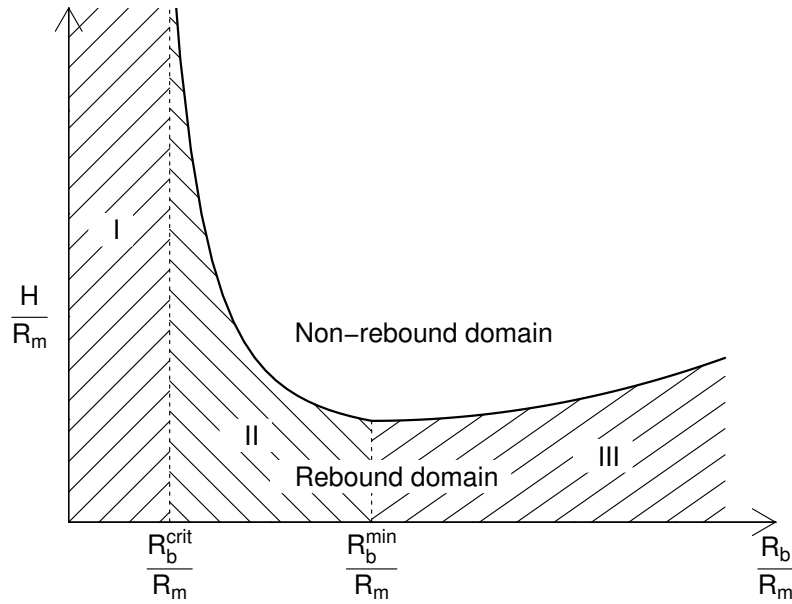
**Figure 2.6:** *Definition of the impact regimes, where H is the height of the impact granular medium, $R_b$ is the radius of the boulder, $R_m$ is the mean size of the grains, $R_b^{crit}$ is the asymptotic value between regime I and II, $R_b^{min}$ is the critical value between regime II and III (Bourrier et al., 2008).*

This diagram was interpreted by Bourrier et al. (2008) from an energy exchange point of view. The bouncing is closely related to energy transfers between the projectile and the soil. For a small impacting particle, the impact is mainly determined by the first interaction between the impacting particle and the soil. For an intermediate-sized impacting particle, the compression wave propagation through the sample is the leading phenomenon. Impacting particle bouncing is attributed to a second energy supply from the soil after the compression wave's round trip through the sample. For a large impacting particle, bouncing is associated with the formation of a compact layer below the impacting particle.

The studies of Bourrier et al. (2008) provide new insights into the bouncing and energy propagation processes, however, a more detailed layer division can be conducted since the behaviours of different parts of the same crown should be different due to different loading and boundary conditions. In addition, while the bouncing occurrence regime is obtained in 2D impact cases, the limitation is the difference between 2D simulations and 3D reality. Specially, energy dissipation in 3D simulations might lead to the

restriction of the second regime because this regime is mainly caused by energy transfers associated with elastic strain energy propagation and small-particle rearrangements. In addition, the microstructure of the medium and micromechanics taking place at grain scales were proven to be key parameters that influence the response of the granular medium (Oda and Kazama, 1998; Radjaï et al., 1998; Tordesillas et al., 2014). Therefore, further identification and quantification of the micromechanisms involved in the load transfer inside the impacted granular medium should be conducted.

## 2.3 Micromechanical properties of granular materials

The granular material, as a discontinuous medium, is heterogeneous with a disordered texture. The mechanical response of the granular medium generally depends on two aspects, one is the grain properties: size, shape, rigidity, friction, the other is their aggregation: packing, void ratio, loading path, fabric tensor (Bardet, 1994; Nouguier-Lehon et al., 2003; Antony and Kuhn, 2004; Ciamarra et al., 2005; Calvetti et al., 2005; Bourrier et al., 2008; Kondic et al., 2012; Cambou et al., 2013). Particularly, Kondic et al. (2012) modelled the impact of an intruder on a dense granular material based on a 2D discrete element method. The results indicate that polydispersity and related structural order, as well as frictional properties of the granular particles, play crucial roles in determining the impact dynamics.

### 2.3.1 Bimodal character of load transmission in granular materials

Experimental and numerical studies of the probability density distribution of contact forces show that, in all cases, the distribution decays exponentially at large forces and shows a plateau or possibly a small peak near the average force (Figure 2.7). Particularly, the simulations of Ciamarra et al. (2005) show that the exponential decrease trend is time-independent during a projectile's deceleration in the medium. Compared to a Gaussian profile, the exponential tail indicates a significantly higher probability of an individual contact force greatly exceeding the mean force.
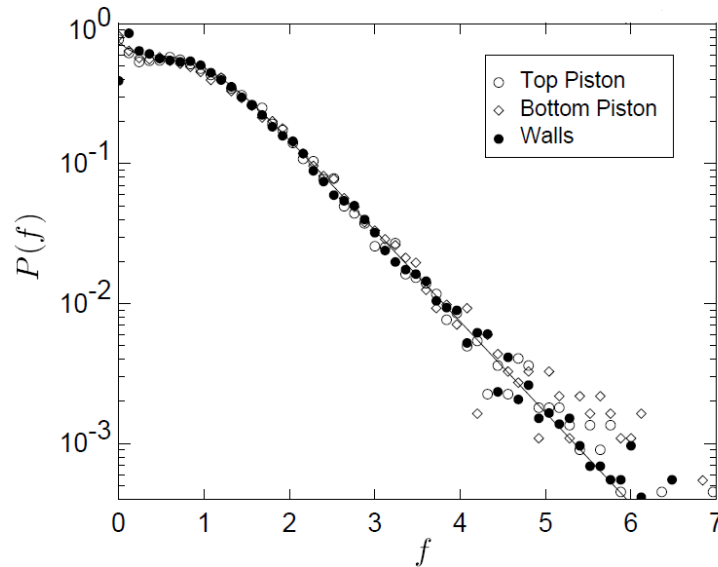
***Figure 2.7:*** *Probability density distribution of normalized force in Mueth's experiments (Mueth et al., 1998)*

Consequently, the transmission of forces in the granular medium reflects the bimodal character of the granular medium which involves a strong percolating network of contacts carrying a force larger than the average force, and a weak network of contacts carrying a force smaller than the average force (Radjaï et al., 1998; Antony and Kuhn, 2004; Majmudar and Behringer, 2005). Preferentially oriented parallel to the main loading direction, the strong force network is mainly the load bearing system, while oriented mainly perpendicular to the main loading direction, the weak network is mainly responsible for the stability of the loading-bearing strong network as well as the energy dissipation (Figure 2.8).

Particularly, the experiments of Iwashita and Oda (1998, 2000) showed that the highly stressed particles are aligned, like columns, parallel to the loading direction in each of the tests. The generation of column-like structures during the hardening process, and the collapse of the column-like structures during the softening process are observed in DEM simulations (Iwashita and Oda, 1998, 2000; Majmudar and Behringer, 2005). The fact that the grain-grain contacts which support large forces are usually correlated in a line-line mode over distances of several particle diameters leads to the so called "force chains". Force chains vary in size from a few to many grains that can percolate through the whole sample. Supporting most of the external load, effectively shielding large regions of the
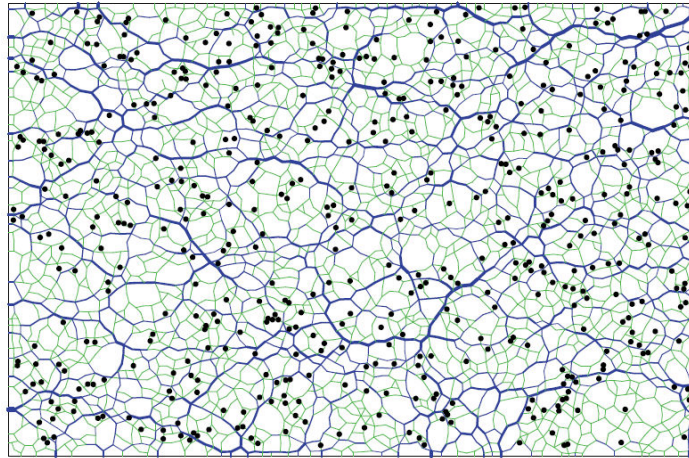
*Figure 2.8:* *The force-bearing network of contacts in a biaxially compressed system of 4000 disks. The line thickness is proportional to the normal force. The strong and weak forces are shown in dark and light colors, respectively. The sliding contacts are marked by small filled circles (Radjaï and Lanier, 2009)*

material, force chains are responsible for material strength. The deformation of granular medium is a process of force chain self-organizations (Iwashita and Oda, 1998, 2000; Majmudar and Behringer, 2005; Tordesillas et al., 2009; Cambou et al., 2013; Tordesillas et al., 2014; Nordstrom et al., 2014; Zhu et al., b,a).

Force chain networks can be visualized in 2D experiments by using photo-elastic particles and in 3D experiments by using fluorescence techniques coupled with laser-sheet scanning. Photoelasticity is based on the idea that stresses within a material affect the way light propagates depending on the polarization of the light and the forces. By placing a stressed photoelastic object between crossed polarizers, it is possible to deduce the forces that the object bears. Figure 2.9 shows the distribution and evolution of force chains inside shear test by using photoelastic grains (Zhang et al., 2010).

## 2.3.2   The role of force chains in granular materials

The bimodal character of the granular material and force chains are the key points for understanding the behaviour of granular materials. The force chain related mechanisms have been mainly investigated in quasi-static cases (Peters et al., 2005; Tordesillas et al., 2009; Zhang et al., 2010; Tordesillas et al., 2014). For instance, in quasi-static bixial tests,
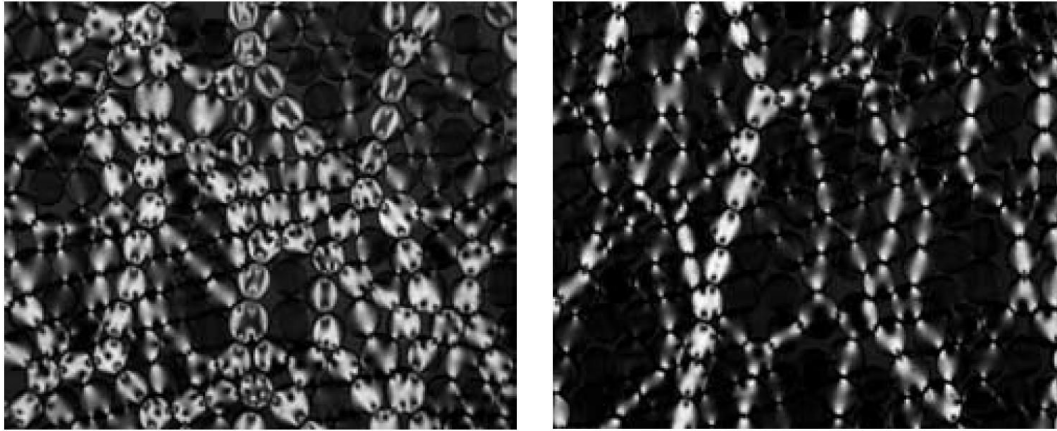
*Figure 2.9:* *Photoelastic particles force chains obtained by Majmudar and Behringer (2005): a low-force sheared state(left), a high-stress isotropically compressed state (right)*

force chains are responsible for the strength and the microstructure of the medium: the establishment and buckling of force chains are responsible for the mechanical response of the specimen in terms of deviatoric stress, the buckling of force chains is shown mainly locating inside the shear band, and is related to the increase of local void ratio around the buckling point as well as the increase of kinetic energy inside the sample (Tordesillas et al., 2009; Zhang et al., 2013; Zhu et al., b,a). In case of a dense granular material submitted to indentation by a rigid flat punch, the deformation of the material is shown to be governed by force chains and the surrounded contact loops (Tordesillas et al., 2014).

However, in dynamic cases such as rockfall impact characterized by strong energy exchanges and particle reorganizations, force chains related mechanisms have not been well investigated. Force chains might play an important role in both the impact force and the bouncing of boulder, as well as the load transfer inside the medium, the deformation and the microstructure evolution of the material. Force chain investigation has great potentials, the corresponding investigation of load bearing systems, force networks, and the evolution of force chain distribution is still required.

## 2.4   Numerical modelling based on a discrete element method

Benefit from the development of computer science, numerical modelling has become a very popular approach to study scientific and engineering problems. In the domain of civil engineering, the commonly used numerical modelling tools include Finite Element Method (FEM), Finite Difference Method (FDM), Discrete Element Method (DEM). Although few works using FEM modelling the impact of a boulder on a soil cushion were conducted (e.g. Degago et al., 2008), DEM is more relevant for modelling the discrete properties of granular materials by modelling the granular assembly as an aggregation of particles. Today DEM is becoming widely accepted as an effective method for addressing problems in granular and discontinuous materials, especially in dynamic impact cases involving rapid loading and unloading, large deformations related to grain rearrangements (e.g. Dolezalova et al., 2002; Ciamarra et al., 2005; Calvetti et al., 2005; Bourrier et al., 2008).

DEM simulations have great advantages compared to experiments. DEM simulations allow to simulate the behaviour of granular medium at different scales, from macroscopic scales to microscopic scales. The macroscale corresponds to the boundary scales, the bouncing of the boulder, the deformation of the medium. The mesoscale corresponds to the scale of group of particles, force chains or grain loops for instances. The microscale corresponds to the local contact of two grains. Variables such as the kinetic energy, energy dissipation, number of contacts, contact forces between particles, energy transfers, force chains can be much more easily addressed compared to experimental approaches. Besides, DEM modelling can vary easily the impact conditions to conduct parametric studies.

### 2.4.1   Introduction of discrete element method

#### 2.4.1.1   Calculation cycle

The macroscopic response of the granular medium is governed by the contacts between adjoining particles. The relative displacements of the particles are controlled by the force - displacement law (contact law). Each two adjacent elements can contact or separate, which allows to model large deformations taking place inside the medium.
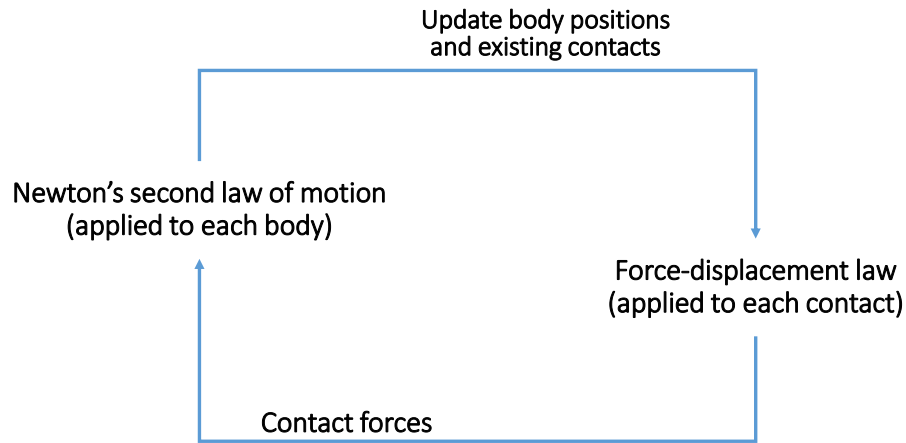
*Figure 2.10:* *Calculation cycle of DEM method*

Figure 2.10 shows the calculation cycle in DEM. In each calculation cycle, the positions of particles are first detected and contact forces are computed according to the contact law, then Newton's second law is solved to update the positions of the particles. The calculation is processed in a given time step $\Delta t$, in which the velocities and the accelerations are constant.

### 2.4.1.2   Principle of the calculation

The motion of a particle is determined by the resultant force and moment acting upon it which can be described in terms of the translational and rotational motion of the particle. The translational movement of a particle can be characterized by its position $x_i$, velocity $\dot{x}_i$ and acceleration $\ddot{x}_i$. Correspondingly, the rotational movement can be characterized by the angular velocity $\omega_i$ and the acceleration $\dot{\omega}_i$.

The resultant force $F_i$ and moment $M_i$ on a particle $i$ are calculated as:

$$F_i = m\ddot{x}_i \quad \text{and} \quad M_i = I\dot{\omega}_i \tag{2.19}$$

where $m$ denotes the mass of the particle, $I$ denotes the moment of inertia of the particle, for spherical particles with a radius $R$, $I = \dfrac{2}{5}\pi m R^2$.

Equation (2.19) can be integrated using a centred finite difference procedure involving a time step $\Delta t$. The quantities $\dot{x}_i$ and $\omega_i$ are computed at the mid-intervals of $t \pm \Delta t/2$, while the quantities $x_i$, $\ddot{x}_i$, $\dot{\omega}_i$, $F_i$ and $M_i$ are computed at the primary intervals of $t \pm \Delta t$. The translational and rotational accelerations at time $t$ can be calculated as:

$$\ddot{x}_{i,t} = (\dot{x}_{i,t+\Delta t/2} - \dot{x}_{i,t-\Delta t/2})/\Delta t \tag{2.20}$$

$$\dot{\omega}_{i,t} = (\omega_{i,t+\Delta t/2} - \omega_{i,t-\Delta t/2})/\Delta t \tag{2.21}$$

Inserting these equations into equation (2.19) results in:

$$\dot{x}_{i,t+\Delta t/2} = \dot{x}_{i,t-\Delta t/2} + (F_{i,t}/m)\Delta t \tag{2.22}$$

$$\omega_{i,t+\Delta t/2} = \omega_{i,t-\Delta t/2} + (M_{i,t}/I)\Delta t \tag{2.23}$$

Finally, the velocities are used to update the positions of the particle as:

$$x_{i,t+dt} = x_i + \dot{x}_{i,t+dt/2}dt \tag{2.24}$$

### 2.4.1.3  Contact laws

The overall constitutive behaviour of a material is simulated in DEM by associating a contact model to each contact (Cundall and Strack, 1979). Different contact models can be used in DEM to model different materials, such as soil (Bourrier et al., 2013), concrete (Hentz et al., 2004) or snow (Nicot, 2004).

In soil mechanics, the interaction between two particles can be expressed as elastic in the normal contact direction and elastic-plastic in the shear direction:

$$F^n = k^n u^n \tag{2.25}$$

$$dF^s = k^s du^s \quad \text{and} \quad F^s \leq F^n \tan \varphi \tag{2.26}$$

where $F^n$ is the normal contact force, $dF^s$ is the incremental shear contact force, $k^n$ and $k^s$ are the normal and shear stiffness respectively, $u^n$ is the normal displacement, $du^s$ is the shear incremental displacement, $\varphi$ is the inter particle friction angle.

Two kinds of elastic contact models are commonly used in the literature: linear models and the Hertz-Mindlin model. Linear models assume that the displacement is directly proportional to the force, which allows a larger time step to be used in calculations. Linear elastic model is the most simple and the most frequently used model in DEM. Studies in literature have proven that the simple linear contact law is sufficient to capture the main features of granular materials, see Bardet (1994); Belheine et al. (2009); Calvetti et al. (2005); Iwashita and Oda (1998); Oda et al. (1982); Olmedo et al. (2015); Zhang et al. (2014); Tordesillas et al. (2014).

Contrary to linear models, the Hertz-Mindlin model includes non linear elasticity in the normal direction (Bourrier et al., 2008). The model is described as follows:

$$k^n = \left(\frac{2G\sqrt{2R}}{3(1-\nu)}\right)\sqrt{u^n} \tag{2.27}$$

$$k^s = \left(\frac{2(G^2 3(1-\nu)R)^{1/3}}{2-\nu}\right)|F_i^n|^{1/3} \tag{2.28}$$

where $G$ is the elastic shear modulus, $\nu$ is the Poisson's ratio, $R$ is the sphere radius.

Hertz-Mindlin model tends to produce more accurate stress strain behaviours, however can be computationally expensive to implement due to the smaller time step requirement. This thesis adopts the linear elastic contact law to model particle contacts. The DEM contact laws will be demonstrated in chapter 3.

#### 2.4.1.4 Critical time step

The choice of time step is very important in DEM modelling. It should be carefully chosen to maintain a stable numerical solution on one hand and to optimize the computation time on the other hand. In addition, the time step must be low to make sure the movement in a time step is much smaller than the grain size.

The shortest time scales arise from the oscillation of one or two grains. If we consider each element of the assembly as a oscillator of mass $m$ connected via a spring stiffness $k$ to a fixed body, time step is generally determined according to the characteristic period of oscillation. The critical time step $t_{crit}$ is finally obtained by taking a fraction of the smallest time period obtained on all particles. Considering both the translational and rotational motion of the particles inside the medium, the critical time step is calculated as:

$$t_{crit} = \min(\sqrt{m/k^n}, \sqrt{I/k^r}) \tag{2.29}$$

where $I$ is the moment of inertia of a particle, $k^r$ is the rolling stiffness.

### 2.4.1.5   Yade-DEM code

Yade is an open-source platform running in Linux systems for discrete numerical modelling. The computation parts are written in C++ using flexible object model, allowing independent implementation of new algorithms and interfaces. Python is used for rapid and concise construction, simulation control, post-processing and debugging (Šmilauer et al., 2010). Implemented with various contact laws, Yade is capable of modelling various materials and loading conditions, such as rockfall impact (e.g. Zhang et al., 2014), conventional soil mechanics testing, debris flow (e.g. Albaba et al., 2015b), snow avalanche (e.g. Hagenmuller et al., 2014).

## 2.4.2   Modelling of particle shape

Spherical particles are the most simple to be handled in DEM simulations, since its geometry is only determined by the radius. However, real particles have various shapes. Studies reported in the literature have shown that the mechanical behaviour of granular material is significantly influenced by particle shape effects (Nouguier-Lehon et al., 2003; Antony and Kuhn, 2004; Pena et al., 2007).

Particularly, Nouguier-Lehon et al. (2003) analysed the influence of grain shape and angularity on the behaviour of granular materials from a two-dimensional analysis by means of a discrete element method (Contact Dynamics). Different shapes of grains have been studied (circular, isotropic polygonal and elongated polygonal shapes, Figure 2.11). The results show that the behaviour of granular materials is significantly influenced by the shape. In fact, particle shape influences the fabric anisotropy of the specimen and therefore, it also has effects on the occurrence of the steady static.
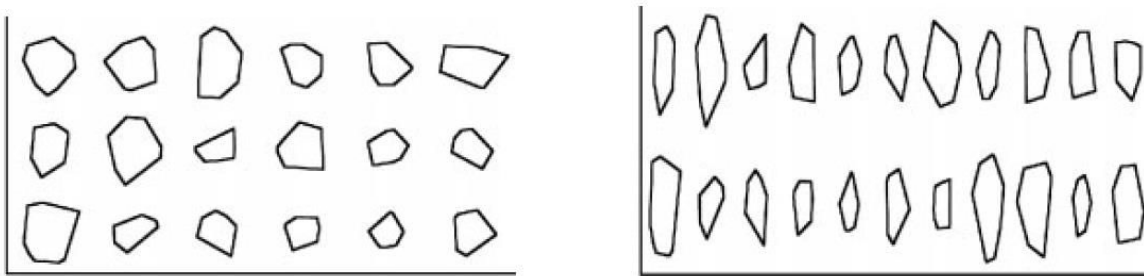


*Figure 2.11:*  *Isotropic polygonal grains (left) and elongated polygonal grains (right) (Nouguier-Lehon et al., 2003)*

In order to realistically account for the particle shapes of geo-composite structures used in civil engineering, Nicot et al. (2007) created unbreakable agglomerates of spheres to model the complex shapes of rocky particles. Particularly, parallelepiped-like clumps and ellipsoidal clumps were generated. Each clump was composed of roughly 500 spherical elements to ensure the acceptable computational times (Figure 2.12). By successfully reproducing the grain size distribution and the initial porosity of the experimental samples, Nicot et al. (2007) claimed that the modelling procedure made it possible to describe a wide range of assembles of variously shaped rocky particles, while reproducing the grain size distribution fairly well.

Iwashita and Oda (1998) modelled particle shape effects by adopting rolling resistance in DEM simulation of biaxial tests. The results showed that with the consideration of rolling resistance, not only the generation of large voids inside a shear band but also the high gradient of particle rotation along the shear band boundaries were reproduced, in a quite similar manner to those observed in natural granular soils. Iwashita and Oda (1998) concluded that the rolling resistance allows to yield better results for simulating the
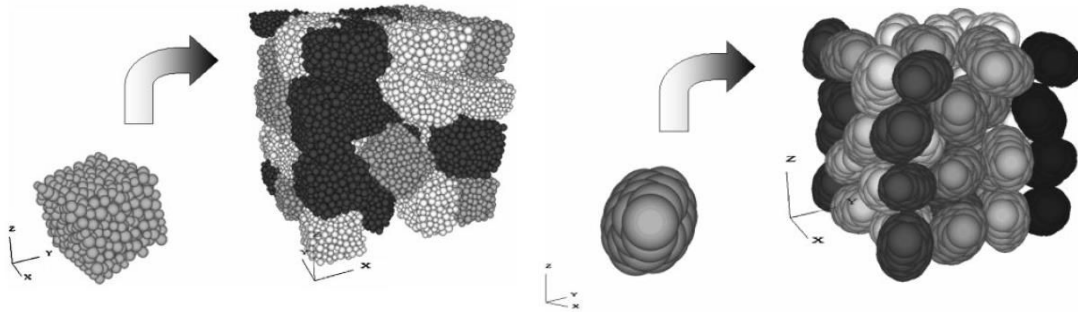
*Figure 2.12:* *Parallelepiped-like clumps (left) and ellipsoidal clumps (right) (Nicot et al., 2007)*

micro-structure developed inside the shear band. In addition, the study of Estrada et al. (2011) indicated that rolling resistance may be employed to imitate the effect of angular shape in DEM simulations of granular materials. More importantly, the results suggest that the hindrance of particle rotations is a major effect of angular particle shape. Rolling resistance can model different materials by adjusting rolling resistance parameters. This thesis adopts the rolling resistance to model particle shape effects. The implementation of rolling resistance in DEM contact laws together with the calculation of energy items will be demonstrated in chapter 3.

### 2.4.3   Energy dissipation in granular materials

It is known that energy can be dissipated inside granular materials through particle friction, damping, particle fragmentation and crushing. Frictional energy dissipation occurs when grains have relative sliding or relative rolling displacement. Concerning damping, Newton damping (Šmilauer et al., 2010) and viscous damping are two kinds of damping that are most often used in DEM simulations. Newton damping is an artificial numerical damping approach, which is adopted for dissipating energy and fast stabilizing the sample. This artificial damping has little influence in the mechanical response of the sample under quasi-static loading but has big influences in dynamic loading (Shiu et al., 2005; Plassiard et al., 2009). Viscous damping is usually characterized by damping coefficients. The calibration of damping coefficients is usually based on experimental results. In case of energy dissipation due to particle fragmentation and crushing effects,

the fracture of the aggregates is usually modelled as the breakage of bounded aggregates (Hardin, 1985; Plassiard et al., 2005; Wang and Yan, 2012). Particularly, the study of (Wang and Yan, 2012) indicates that the major roles of particle breakage, which itself only dissipates a negligible amount of input energy, are to advance changes in the soil fabric and to promote the interparticle friction dissipation by increasing the number of particles and densifying the specimen.

The issue that which energy dissipation approach plays a more important role between viscous damping and frictional displacement is not clear. The investigations of Kondic et al. (2012) and Nordstrom et al. (2014) suggest that static friction between grains does play a substantial role in the energy dissipation. Particularly, Tsimring and Volfson (2005) simulated penetration of large projectiles into dry granular media by using molecular dynamics discrete element method. The simulation results indicate that most of the ball energy is dissipated through the frictional contacts among the grains (about 70%), about 20% is lost due to inelastic collisions (viscous damping), and about 10% is spent on the change in the gravitational energy of the grains. However, Hou et al. (2005) investigated the dynamics of a projectile penetrating in granular systems in 2D and 3D cases, the drag force on the projectile suggested that fluidlike viscous dissipations in the bed can be neglected in 3D experiments, however cannot be neglected in quasi-2D granular beds due to the boundary conditions inducing a strong kinematical constraint.

In addition, the issue that which frictional energy dissipation mode is more important between frictional sliding and frictional rolling is not clear. The studies of Oda et al. (1982), Bardet (1994) and Shodja and Nezami (2003) found that rolling motions are more important than sliding in the case of using oval particles. However, biaxial simulation results of Zhang et al. (2013) from a comprehensive DEM study indicate that interparticle sliding and rolling are the two competing particle-scale deformation mechanisms that work together to dissipate a minimum amount of external input work and advance the material fabric evolution. The amount of energy dissipation by frictional sliding is larger than frictional rolling. Therefore, the role of frictional energy dissipations in granular materials still needs further investigations.

## 2.5 Conclusion

Both rockfall trajectory analysis and protection structure design in rockfall engineering require a thorough knowledge of the mechanisms that govern the bouncing of boulder and the response of the granular medium. Studies reported in the literature concerning the interaction of a boulder and a granular medium as well as bouncing of boulder on a granular medium are reviewed from engineering practices, experiments and numerical modelling points of view.

The studies in the literature show that the response of the medium and the bouncing of boulder depend not only on the properties of the boulder (mass, shape, incident velocity and angle), but also on the properties of the granular medium (material, layer thickness, compaction, inclination angle). Analytical approaches and experiments propose easy-to-use expressions to calculate the impact force, penetration depth and the transmitted force inside the granular medium as well as recommend values of restitution coefficients to characterize the bouncing of the boulder. However, those obtained results are limited to only specific cases and cannot be generalized because the mechanisms that govern the bouncing of boulder and the response of the granular medium are not well understood and accounted for.

Calibrated based on experiments, numerical simulations are relevant to model the boulder-medium interactions. However, micromechanisms that govern the behaviour of the granular medium are still required. Particularly, the role of force chains and force chain microstructure in the the bouncing of the boulder and the response of the granular medium are missing. Together with the energy propagation process inside the medium and the effects of particle shapes, further investigations are encouraged. This is the main motivation of Chapter 5.

# Chapter 3

# DEM modelling of the impact process

## Contents

## 3.1   Introduction

The objective of this chapter is to develop a 3D numerical model to simulate the interaction between a granular medium and a falling boulder. The model should not only be able to take into account the particle shape effects of the medium but also be able to reproduce experimental results for model validation purpose. After being validated, the 3D model allows to further investigate the response of the medium and the boulder in different impact conditions.

To achieve these goals, the first task is to select a relevant DEM contact law. Correspondingly, a simple elastic-plastic contact law implemented with rolling resistance is adopted to model the granular medium. The second task is to take appropriate contact parameters. Accordingly, a special procedure is adopted that the contact law is first calibrated under quasi-static triaxial tests and further used into dynamic impact modelling. We suppose it is acceptable to model dynamic impacts based on contact law calibrated under quasi-static tests due to the fact that, first of all, very few impact experiments are available for model validation, second, the rockfall impacts are concerning low dynamic cases (in this work, the maximum impact velocity of boulder is 20 m/s).

## 3.2   Contact model description

Concerning the DEM modelling of the interaction between a falling boulder and a granular medium, there is no general consensus on which contact model is the best one, the choice among available contact laws is still an open question. In our simulations, computational time constraints lead us to employ linear elastic models instead of the Hertz-Mindlin contact law. Moreover, in the context of dynamic impact, linear contact models are able to produce non-linear waves inside the impacted granular medium due to the discrete nature of granular materials (Goddard, 1990).

### 3.2.1   Description of Cundall-Strack contact law

The Cundall-Strack contact law considers a linear relation between the inter-particular penetration and the force in the normal direction, while follows an elastic-plastic relation in the shear direction including the Mohr-coulomb criterion (Cundall and Strack, 1979).
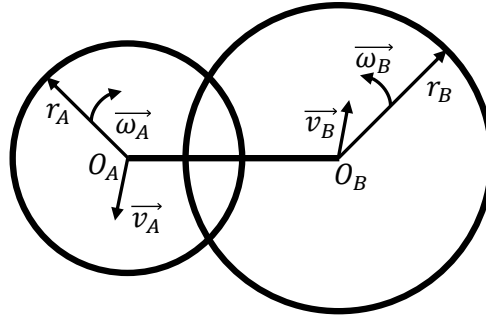


*Figure 3.1:  Two spheres in contact*

In case two spherical particles $A$ and $B$ are in contact (Figure 3.1), the normal and shear contact behaviours are described by the following equations:

$$\vec{F_n} = k_n \vec{u_n} \qquad \text{and} \qquad F_n > 0 \tag{3.1}$$

$$d\vec{F_s} = k_s d\vec{u_s} \qquad \text{and} \qquad F_s \leq \mu F_n \tag{3.2}$$

$$k_n = 2 \frac{E_A^n r_A E_B^n r_B}{E_A^n r_A + E_B^n r_B} \tag{3.3}$$

$$k_s = 2 \frac{E_A^s r_A E_B^s r_B}{E_A^s r_A + E_B^s r_B} \tag{3.4}$$

where,

- $\vec{F_n}$ is the normal contact force between the two particles;
- $d\vec{F_s}$ is the incremental shear force between the two particles;
- $\vec{u_n}$ is the inter-particular displacement between the two particles;
- $d\vec{u_s}$ is the shear incremental displacement between the two particles;
- $E_A^n$ and $E_B^n$ are the normal local modulus of particle $A$ and $B$;

- $E_A^s$ and $E_B^s$ are the shear local modulus of particle $A$ and $B$. In our simulations, the particles have the same mechanical properties, therefore, $E_A^n = E_B^n = E^n$, $E_A^s = E_B^s = E^s$, $\alpha = E^s / E^n$.

- $r_A$ and $r_B$ are the radii of two contact particles $A$ and $B$ respectively;

- $k_n$ is the normal stiffness; $k_s$ is the shear stiffness; In the case of a spherical particle $A$ contacts with a wall boundary, $k_n = E^n \, r_A$, $k_s = \alpha \, k_n$;

- $\mu$ is the local friction of the contact, it takes the minimum friction value of the two particles, $\mu = \tan \phi = \tan(\min(\phi_A, \phi_B))$. In our simulations, $\phi_A = \phi_B$.

The following equations illustrate how the relative velocity and the incremental shear displacement are calculated in DEM:

$$
\begin{cases}
a = \dfrac{r_A + r_B}{r_B + r_B - u_n} \\
\vec{v} = a \cdot (\vec{v_B} - \vec{v_A}) + \vec{\omega_B} \times (-r_B \cdot \vec{n}) - \vec{\omega_A} \times (r_A \cdot \vec{n}) \\
\vec{v_n} = (\vec{n} \cdot \vec{v}) \cdot \vec{n} \\
\vec{v_s} = \vec{v} - \vec{v_n} \\
\vec{du_s} = \vec{v_s} \cdot \Delta t
\end{cases}
\tag{3.5}
$$

where,

- $\vec{v_A}$ and $\vec{v_B}$ are the translational velocities of particle $A$ and $B$, $\vec{\omega_A}$ and $\vec{\omega_B}$ are the rotational velocities of $A$ and $B$;
- $\vec{n}$ is the contact normal, and is particularly defined from the vector joining the center of particle $A$ to the center of particle $B$;
- $\vec{v}$ is the relative velocity between $A$ and $B$, with normal component $\vec{v_n}$ and shear component $\vec{v_t}$;
- $\Delta t$ is the time step;

In order to insure the accuracy and the stability of calculations, a small time step should be used so that the relative displacement during each time step is sufficiently small with respect to the particle sizes.

### 3.2.2   Rolling resistance

In reality, particles have rough surface textures and are sometimes covered with a thin film of weathered products (Mitchell and Soga, 1976). Particles do not roll freely over each other, especially for angular grains. Moreover, particle shape is one of key parameters that influences the mechanical response of granular materials: studies in the literature reveal that particle shape affects not only the micro-mechanical properties (contacts, fabrics, etc) but also the macromechanical response (bulk strength, deformation, etc), see Nouguier-Lehon et al. (2003), Antony and Kuhn (2004) and Pena et al. (2007).

In discrete element modelling, the use of spherical grains can keep calculation costs low to maintain a fast calculation, however, the major drawback is that excessive rolling occurs (Radjaï and Dubois, 2011). Instead, particle shapes can be accomplished in DEM by polygons (Nouguier-Lehon et al., 2003; Pena et al., 2007), clumped disks or spheres (Szarf et al., 2011; Albaba et al., 2015a), and rolling resistance (Iwashita and Oda, 1998). Among which, rolling resistance is considered in DEM by adding a resistant moment in the contact to limit the relative rotation between the grains.

Even though rolling resistance is an artificial approach, it has been proven to be efficient in accounting for the particle shape effects. For instance, Iwashita and Oda (1998) considered a rolling resistance law between contacting particles with the aim of modelling the roughness effect. They succeeded in reproducing large voids inside a shear band as well as the high gradient of particle rotation along the shear band boundaries. This approach has also been considered by authors such as Plassiard et al. (2009), Belheine et al. (2009), Tordesillas et al. (2009, 2014), Zhou et al. (2013), Zhao and Guo (2014).

Rolling resistance has already been implemented into the elastic-plastic contact law and used to model triaxial tests. It allows the simulation to use the most simple spherical shape to improve modelling efficiency. In addition, different materials can be produced by simply adopting different rolling parameters.

In our simulations, rolling resistance is adopted to model the particle shape effects. An elastic-plastic relation between the resistant moment and the relative rotation within a contact is considered (Iwashita and Oda, 2000). In this 3D context, rolling resistance considers both the resistance against the relative bending and twisting rotations. The implementation of rolling resistance in DEM code is given as follows:

$$d\vec{M_b} = k_b d\vec{\theta_b} \qquad \text{and} \qquad M_b \le \eta_b F_n \tag{3.6}$$

$$d\vec{M_{tw}} = k_{tw} d\vec{\theta_{tw}} \qquad \text{and} \qquad M_{tw} \le \eta_{tw} F_n \tag{3.7}$$

$$k_b = \beta_b k_s r_A r_B \tag{3.8}$$

$$k_{tw} = \beta_{tw} k_s r_A r_B \tag{3.9}$$

$$\eta_b = \eta_{tw} = \min(\eta_A r_A, \eta_B r_B)) \tag{3.10}$$

$$\begin{cases} d\vec{\theta} = (\vec{\omega_B} - \vec{\omega_A}) \cdot \Delta t \\ d\vec{\theta_{tw}} = (\vec{n} \cdot d\vec{\theta}) \cdot \vec{n} \\ d\vec{\theta_b} = d\vec{\theta} - d\vec{\theta_{tw}} \end{cases} \tag{3.11}$$

where,

- $dM_b$ and $dM_{tw}$ are the incremental bending and incremental twisting moments respectively;

- $k_b$ and $k_{tw}$ are the bending stiffness and the twisting stiffness respectively;

- $d\theta$ is the relative rotation between the contact; $d\theta_b$ is component for bending, $d\theta_{tw}$ is the component for twisting;

- $\beta_b$ and $\beta_{tw}$ are the bending and twisting stiffness coefficients respectively;

- $\eta_b$ is the elastic limit coefficient of rolling resistance and is calculated according to parameters $\eta_A$ and $\eta_B$, as well as the geometry of the particles.

In the above equations, the bending and twisting stiffness $k_b$ and $k_{tw}$ are determined to be a function of $k_s$ (see equations 3.8, 3.9) based on an assumption that both of the moments contributed by shear and by rolling have the same order of magnitudes (Iwashita and Oda, 1998). The elastic limit coefficient of rolling resistance $\eta_r$ or $\eta_{tw}$ has similar physical meaning to the inter-particle friction $\mu$, even though it has a dimension of length (Iwashita and Oda, 2000).

Although the mechanisms for rolling and twisting are not exactly the same in reality, here we assume they follow the same plastic criterion and share the same contact parameters for simplification (see equations 3.6, 3.7, 3.8, 3.9, 3.10). In our simulations, $\beta_b = \beta_{tw} = \beta$, $\eta_A = \eta_B = \eta$, $\beta$ is the rolling stiffness coefficient, $\eta$ is the rolling elastic limit.

Indicated by the above equations, the angular velocity can contribute to sliding, rolling and twisting, meanwhile, sliding and rolling or twisting can occur at the same contact. In addition, since no energy dissipation algorithms have been well established for real systems, and no clear guidelines for contact models to be used in DEM simulations, an assumption is made that the energy dissipation in dynamic impact loading involved in this work is mainly due to particle rearrangements. Therefore, energy dissipation is only due to friction between the contacts, no viscous damping nor particle crushing effects are considered (In section 3.3, Newton damping is used during quasi-static triaxial tests).

To sum up, the complete contact model is composed of normal, tangential and rolling contact components. The description of the implemented contact law is shown in figure 3.2.

### 3.2.3   Calculation of energy items

Different sorts of energies involved in the impact process can be calculated, so that energy conservation can be checked at any time. In addition, the investigation of propagation and exchange between different kinds of energies is an important approach to understand the kinematics occurring inside the granular material.
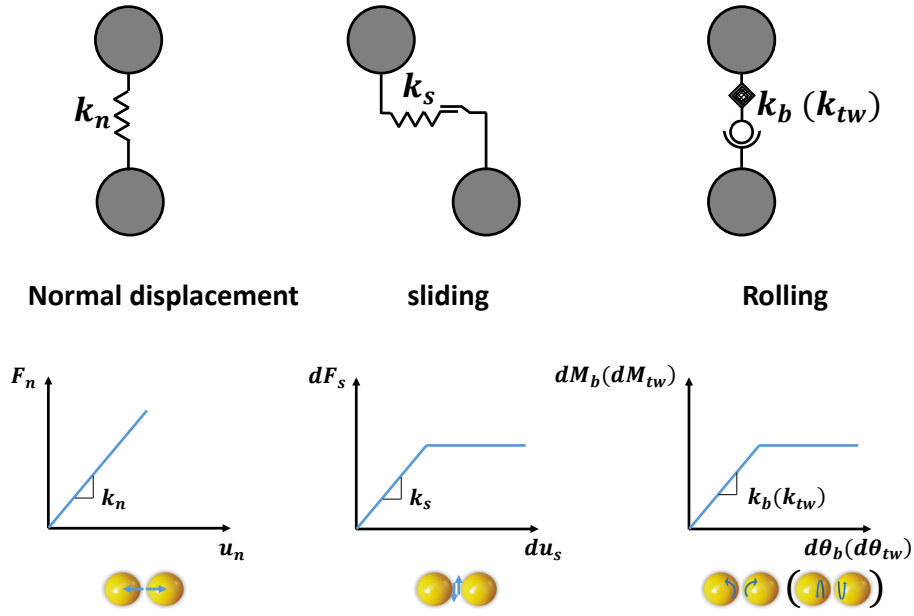
*Figure 3.2: Description of the contact model*

At a time $t$, all energy types involved in the impact process include kinetic energy of the boulder $E_{kb}$, kinetic energy of the medium $E_k$, elastic strain energy $E_s$ (include grain-grain and boulder-grain elastic strain energies), gravity potential energy $E_{mgh}$, and frictional energy dissipation $E_d$. The sum of all energies $E_t$ is given as:

$$E_t = E_k + E_{kb} + E_s + E_{mgh} + E_d \tag{3.12}$$

The kinetic energy of boulder $E_{kb}$ is calculated as:

$$E_{kb} = \frac{1}{2}M_b v_b^2 + \frac{1}{2}I_b \omega_b^2 \tag{3.13}$$

where $M_b$ is the boulder mass, $I_b$ is the boulder inertia, $v_b$ and $\omega_b$ are the translational and angular velocity of the boulder respectively.

A domain $D$ which includes $n$ particles and $m$ contacts is considered, in case we want to investigate the energy propagations inside this domain. This domain is artificially chosen and can locate at any parts of the granular medium. The kinetic energy, elastic strain energy, gravity potential energy, and energy dissipation inside this domain are $E_k(D)$, $E_s(D)$, $E_{mgh}(D)$, $E_d(D)$ respectively.

The kinetic energy $E_k(D)$ is calculated as:

$$E_k(D) = \sum_{i=1}^{n} (\frac{1}{2} m_i v_i^2 + \frac{1}{2} I_i \omega_i^2) \tag{3.14}$$

where $M_i$ and $I_i$ are the mass and inertia of the $i^{th}$ particle of the medium respectively; $v_i$ and $\omega_i$ are the translational and angular velocity respectively.

The gravity potential energy of the domain $E_{mgh}(D)$ is calculated as:

$$E_{mgh}(D) = \sum_{i=1}^{n} (M_i g y_i) \tag{3.15}$$

where $M_i$ is the mass of the $i^{th}$ particle of the medium, $g$ is the gravity acceleration, $y_i$ is the vertical coordinate of particle $i$ with respect to a fixed frame.

The elastic strain energy inside the domain $E_s(D)$ is calculated as:

$$E_s(D) = \frac{1}{2} \sum_{j=1}^{m} (\frac{(F_{j,n})^2}{k_{j,n}} + \frac{(F_{j,s})^2}{k_{j,s}} + \frac{(M_{j,b})^2}{k_{j,b}} + \frac{(M_{j,tw})^2}{k_{j,tw}}) \tag{3.16}$$

where $F_{j,n}$, $F_{j,s}$, $M_{j,b}$, $M_{j,tw}$ are the normal force, shear force, bending moment, twisting moment of the $j^{th}$ contact respectively; $k_{j,n}$, $k_{j,s}$, $k_{j,b}$, $k_{j,tw}$ are the normal, shear, bending, twisting stiffness of the $j^{th}$ contact respectively;

No viscous damping is considered in this work. Therefore, energy dissipation is only due to friction, induced by plastic shearing, bending and twisting displacements. The total friction energy dissipation inside the domain $D$ is calculated as:

$$E_d(D) = E_{ds}(D) + E_{db}(D) + E_{dtw}(D) \tag{3.17}$$

where, $E_{ds}(D)$, $E_{db}(D)$ and $E_{dtw}(D)$ are energy dissipation due to frictional sliding, frictional bending and frictional twisting respectively.

The energy dissipation is defined from an incremental expression. A small enough time step helps improving the energy calculation accuracy. Upon a step increment, the shear displacement increment of a contact $du_{j,s}$ can be divided into an elastic component $du_{j,s}^e$ and a plastic component $du_{j,s}^p$. Only the plastic relative shear displacement leads to energy dissipation. So, energy dissipation due to frictional sliding is calculated as:

$$
\begin{cases}
dF_{j,s} = \min \left( F_{j,s} + k_{j,s}du_{j,s}, \ \tan \phi(F_{j,n} + k_{j,n}du_{j,n}) \right) - F_{j,s} \\
du_{j,s}^p = du_{j,s} - du_{j,s}^e \\
du_{j,s}^e = \dfrac{dF_{j,s}}{k_{j,s}} \\
E_{ds}(D) = \sum\limits_{j=1}^{m} (F_{j,s} + dF_{j,s})du_{j,s}^p
\end{cases}
\tag{3.18}
$$

Similarly, the relative rotation angle contributed by relative bending $d\theta_{j,b}$ can be divided into an elastic component $d\theta_{j,b}^e$ and a plastic component $d\theta_{j,b}^p$. Energy dissipation due to frictional bending is calculated as:

$$
\begin{cases}
dM_{j,b} = \min \left( M_{j,b} + k_{j,b}d\theta_{j,b}, \ \eta_{j,b}(F_{j,n} + k_{j,n}du_{j,n}) \right) - M_{j,b} \\
d\theta_{j,b}^p = d\theta_{j,b} - d\theta_{j,b}^e \\
d\theta_{j,b}^e = \dfrac{dM_{j,b}}{k_{j,b}} \\
E_{db}(D) = \sum\limits_{j=1}^{m} (M_{j,b} + dM_{j,b})d\theta_{j,b}^p
\end{cases}
\tag{3.19}
$$

Similarly, the relative rotation angle contributed by relative twisting $d\theta_{j,tw}$ can be divided into an elastic component $d\theta_{j,tw}^e$ and a plastic component $d\theta_{j,tw}^p$. Energy dissipation due to frictional twisting is calculated as:

$$
\begin{cases}
dM_{tw} = \min\left(M_{j,tw} + k_{j,tw}d\theta_{j,tw},\ \eta_{j,tw}(F_{j,n} + k_{j,n}du_{j,n})\right) - M_{j,tw} \\
d\theta^p_{j,tw} = d\theta_{j,tw} - d\theta^e_{j,tw} \\
d\theta^e_{j,tw} = \dfrac{dM_{j,tw}}{k_{j,tw}} \\
E_{dtw}(D) = \sum_{j=1}^{m} (M_{j,tw} + dM_{j,tw})d\theta^p_{j,tw}
\end{cases}
\tag{3.20}
$$

## 3.3   Contact law calibration and validation

The aim of this section is to calibrate the contact parameters of the implemented contact law based on quasi-static experimental tests. First of all, experimental data of a quasi-static triaixal test on Ticino sand (Salot et al., 2009) is chosen based on an assumption that Ticino sand can represent the granular medium involved in rockfall impact problems. Second, the calibration of the contact parameters is first conducted by reproducing the experimental stress and strain behaviours under confinement of 100 kPa. The calibration follows a procedure based on the studies of Belheine et al. (2009) and Plassiard et al. (2009). Finally, triaxial loading under confining pressure of 200 kPa and 300 kPa are conducted using the calibrated parameters, the corresponding results are compared with experimental results for validation purpose.

### 3.3.1   Triaxial experimental test

The experimental data shown in this section comes from a series of triaixal compression tests performed on Ticino river sand (Salot et al., 2009). Figure 3.3 shows the grain size distribution and the main characteristics of the Ticino sand. This sand is angular (20 and 50% by mass of the particles are angular and sub-angular respectively, Figure 3.3). The Mohr circles obtained according to experimental data of triaxial tests reveals the global friction angle at peak is 41.8° (Figure 3.4).

This sand is chosen for our model calibration since its angularity allows us to assume that Ticino sand can represent the granular medium involved in rockfall impact problems, such as part of the soil of natural or man-made slopes, or part of rockfall protection structures, such as rock sheds or embankments.
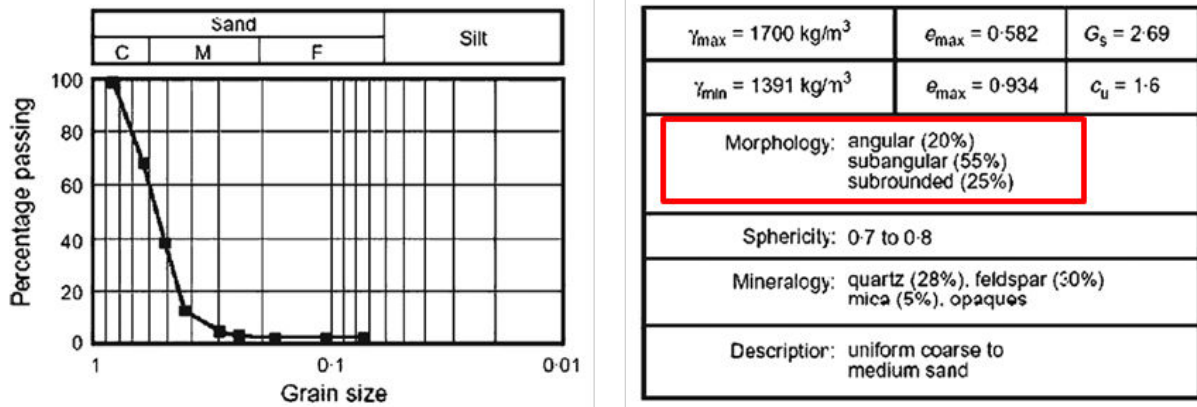


**Figure 3.3:** *Grain size distribution (left) and main characteristic (right) of the Ticino sand used in the experiments (Salot et al., 2009)*
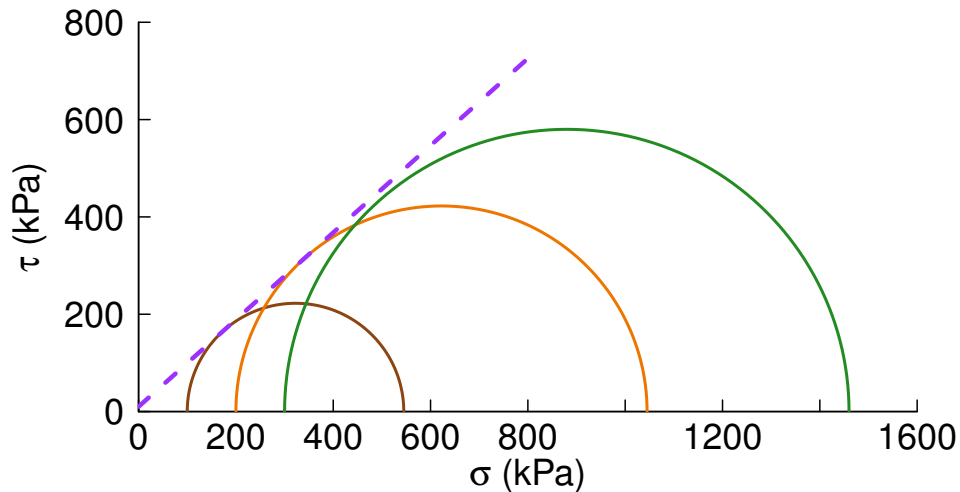


**Figure 3.4:** *Mohr circles obtained based on experimental data of triaxial tests (Salot et al., 2009)*

## 3.3.2 Contact law calibration

### 3.3.2.1 Modelling of the triaxial test

Numerical triaxial test is conducted in DEM to reproduce the mechanical behaviour of the sand for model calibration purpose. The numerical triaxial test is conducted following a three-step procedure (Chareyre and Villard, 2005; Nicot et al., 2011). The procedure is shown in figure 3.5:

1. Generation of a loose poly-disperse particle assembly within six wall boundaries;

2. Increase of particles radii proportionally until the isotropic confinement is reached (The positions of the six wall boundaries are fixed during this stage).

3. Maintain the confining pressures on the four lateral boundaries and conduct deviatoric loading to get the stress-strain behaviour of the sand.
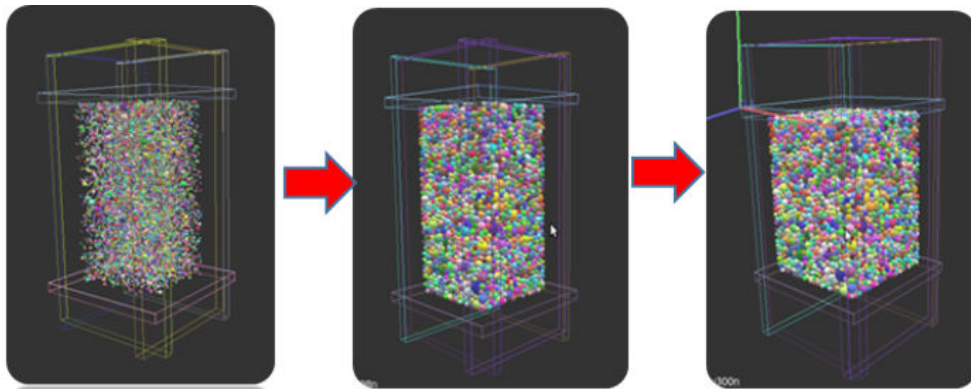


**Figure 3.5:** *Procedure of numerical triaxial test*

The size of the specimen is 2.9 m, 5.8 m, 2.9 m in the $x$, $y$, $z$ direction respectively. The grain size distribution during the whole test procedure always follows a uniform distribution, with a variability of 33% around the mean grain size. In addition, the local friction angle is set as $0°$ during the confinement in order to generate a dense sample.

### 3.3.2.2 Calibration methodology

The calibration of contact parameters is based on reproducing both macroscopic deviatoric stress and volumetric strain behaviours of the sand. The objectives of the calibration aim at reproducing:

- the Young modulus, characterized by the initial slope of stress-strain curve;
- the Poisson's ratio, characterized by the initial slope of volumetric strain;
- the peak value of deviatoric stress and the corresponding axial strain value;
- the dilatancy angle, characterized by the slope of the volumetric strain in dilatancy regime.

The match of stress-strain behaviour is prior to the volumetric strain behaviour during the calibration. Calibration concerns parameters of:

- normal local Modulus $E^n$,
- local stiffness ratio $\alpha$,
- internal friction angle $\phi$,
- rolling stiffness coefficient $\beta$,
- rolling elastic limit $\eta$.

Studies in the literature show that assemblies of circular particles are characterized by very low global friction angles (smaller than $30°$). In case particles have free rotations, when local friction angle is smaller than $20°$, local friction angle is smaller than global friction angle, otherwise, local friction angle is larger than global friction angle (Bardet, 1994; Calvetti, 2008). In case relative rotations of particles are prevented, the global friction angle of the DEM assembly is a linear function of the interparticle friction angle, generally, the global peak and residual friction angles become larger than the local friction angle (Bardet, 1994; Shodja and Nezami, 2003). These studies prove that rolling resistance has effects in improving the deviatoric strength of an assembly.

In our simulations, the rotation of particles is not totally prevented, relative rolling between particles is allowed when rolling plastic regimes is full-filled. Therefore, the situation is between the free rolling and non-rolling cases. In addition, Ticino sand shows a high friction (the global friction angle at peak for Ticino sand obtained by triaxial tests is 41.8°). Therefore, a maximum local friction angle of 45° is allowed to model the friction of the Ticino sand, values exceeding 45° are supposed not to be relevant.

Research of Plassiard et al. (2009) shows that $E^n$ and $\alpha$ control the global Young modulus and Poisson's ratio; $\phi$ influences the peak strength and the dilatancy; $\beta$ has similar effects as $\phi$. Due to the fact that rolling resistance has no effect on the initial slope of stress-strain curve (Bardet, 1994; Plassiard et al., 2009), the calibration starts by reproducing the stress-strain slope without the consideration of rolling resistance.

The calibration procedure adopted in this work is: First, the influence of particle numbers is checked. Second, $E^n$ and $\alpha$ are calibrated by matching with the macroscopic Young modulus and Poisson's ratio. Third, $\phi$ is adjusted to reproduce the volumetric strain while keeping other parameters constant. Finally, $\beta$ and $\eta$ are calibrated to match the stress-strain curve. During deviatoric loading, the axial strain rate is set at the minimum value (smaller than $0.01 \ s^{-1}$) to eliminate the effects of loading rate and insure the quasi-static loading process. An initial series of parameters are chosen before the calibration: $E^n = 2e8$ MPa, $\alpha = 0.3$, $\phi = 45°$, $\beta = 0.01$, $\eta = 0.5$.

### 3.3.2.3   Effects of particle number

In order to analyse the effects of particle numbers and to chose appropriate number to model the sand, three samples composed of 5000, 10000 and 20000 grains are generated respectively. Although the mean sizes of particles are different, the grain size distributions of these three samples all follow uniform distributions. The porosities of the three samples after isotropic confinement are 0.381, 0.375, 0.369 respectively.

Deviatoric loading tests are carried out on each sample without adopting rolling resistance within the contacts. The evolution of deviatoric and volumetric strain point out the following information (Figure 3.6):

- First of all, the difference between the curves are rather small, especially for the curves corresponding to 10000 and 20000 particles. The curve corresponding to 5000 particles has a slightly lower peak value of deviatoric stress. Therefore, a number of 10000 particles seems to be adequate to simulate the macroscopic behaviour of the samples under quasi-static loading.

- Second, the initial slope of stress strain curve is well matched with experimental data. The match of volumetric strain is slightly less good.

- Third, the peak value of the stress is far away from being reached, even the local friction angle is as high as 45°. Moreover, the peak value of the deviatoric stress arrives around a 1% axial strain, which is quite different from experimental results (the peak is arrived around 5% of axial strain).
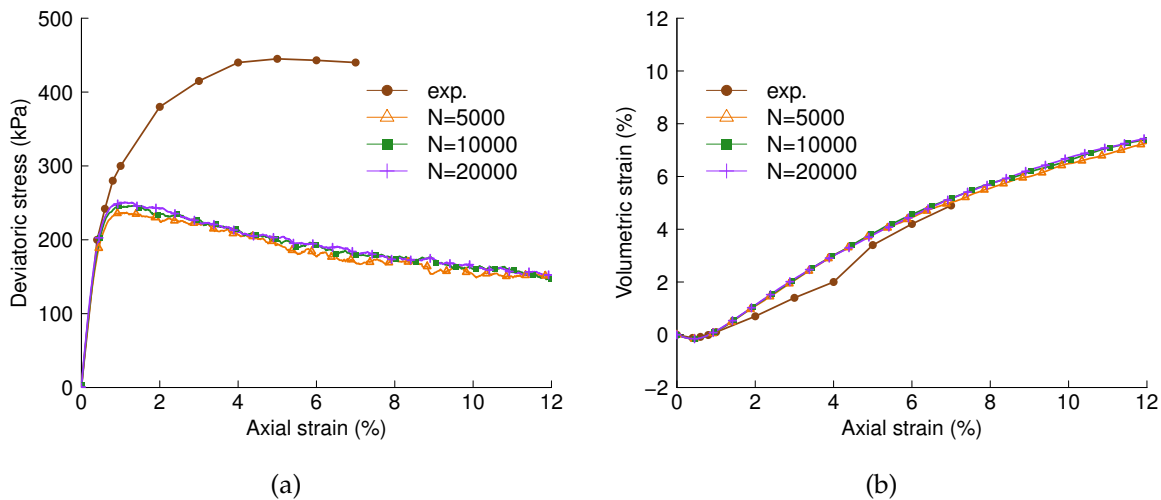


*Figure 3.6: Effects of the number of particles on (a) Deviatoric stress, (b) Volumetric strain*

The nearly negligible differences between the three curves indicate that the number of the grains does not have big influence on the macroscopic stress-strain behaviour under quasi-static triaxial loading. This is mainly due to the fact that no inertia effects exist in quasi-static loading (Plassiard et al., 2009). Therefore, it is sufficient to use 10000 particles modelling the soil sample.

#### 3.3.2.4 Effects of normal local modulus

The effects of normal local modulus are investigated. The objective is to find the best match between simulations and experiments in terms of the initial slope of stress-strain curve as well as the volumetric strain behaviours. Triaxial loading tests are conducted on three samples whose normal local modulus are $1 \times 10^8$ Pa, $2 \times 10^8$ Pa and $3 \times 10^8$ Pa respectively (the other parameters are kept as original values).
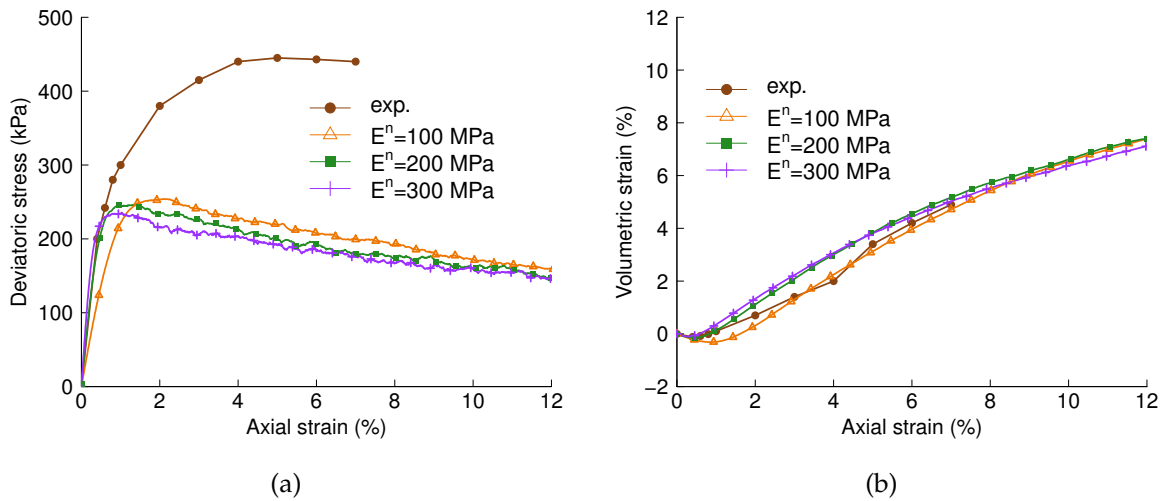


*Figure 3.7:* *Effects of the local modulus on (a) Deviatoric stress, (b) Volumetric strain.*

Figure 3.7 shows that the higher the normal local modulus, the steeper the initial slope of stress-strain curves, as well as the stronger the dilatancy. The lower the value of normal local modulus, the stronger the contraction at the initial stage of triaxial loading. However, the peak value of stress slightly decreases with the increase of local Young modulus. The trends of the results are consistent with results of Plassiard et al. (2009). Illustrated by the results, the initial slope of the stress-strain curve is best captured when the normal local modulus $E^n$ is set as $2 \times 10^8$ Pa.

#### 3.3.2.5 Effects of local stiffness ratio

The effects of local stiffness ratio are studied in this part. The local stiffness ratios are set 0.1, 0.3, 0.6 respectively. Figure 3.8 shows that under the same normal local modulus, the smaller the local stiffness ratio, the smaller the initial slope of stress-strain curve. The difference between curves corresponding to 0.3 and 0.6 is much smaller than the difference between 0.1 and 0.3. Besides, the influence of local stiffness ratio on volumetric behaviour is much smaller than that on the stress behaviour. The simulation results obtained by using a value of 0.3 local stiffness ratio fits best with the experimental data (Figure 3.8(c)).
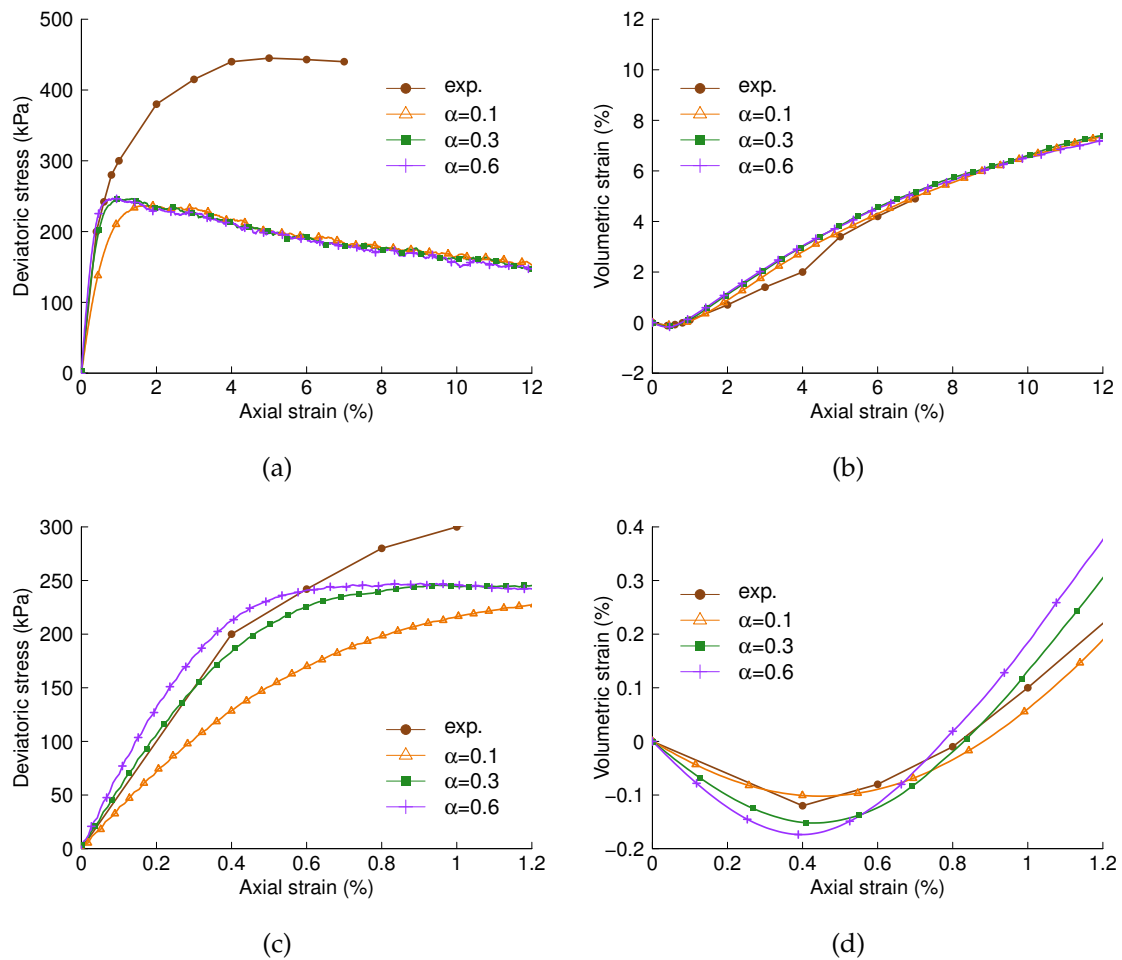


***Figure 3.8:*** *Effects of the local stiffness ratio on (a) Deviatoric stress, (b) Volumetric strain, (c) Zoom of deviatoric stress, (d) Zoom of volumetric strain*

### 3.3.2.6   Effects of rolling stiffness parameter

Known from previous work (Belheine et al., 2009; Plassiard et al., 2009), both local friction angle and rolling resistance have effects of increasing the peak value of deviatoric stress. The higher the local friction angle, the bigger the peak value of deviatoric stress. However, in these simulations, the peak value of the deviatoric stress obtained by experiments is hardly reached even though the internal friction angle is as high as $60°$ (data not shown), therefore, the increase of deviatoric stress is relied on rolling resistance. The effects of rolling stiffness parameter are investigated in this part. As mentioned before, a simplification is made to allow the bending and twisting resistance to take the same parameters.
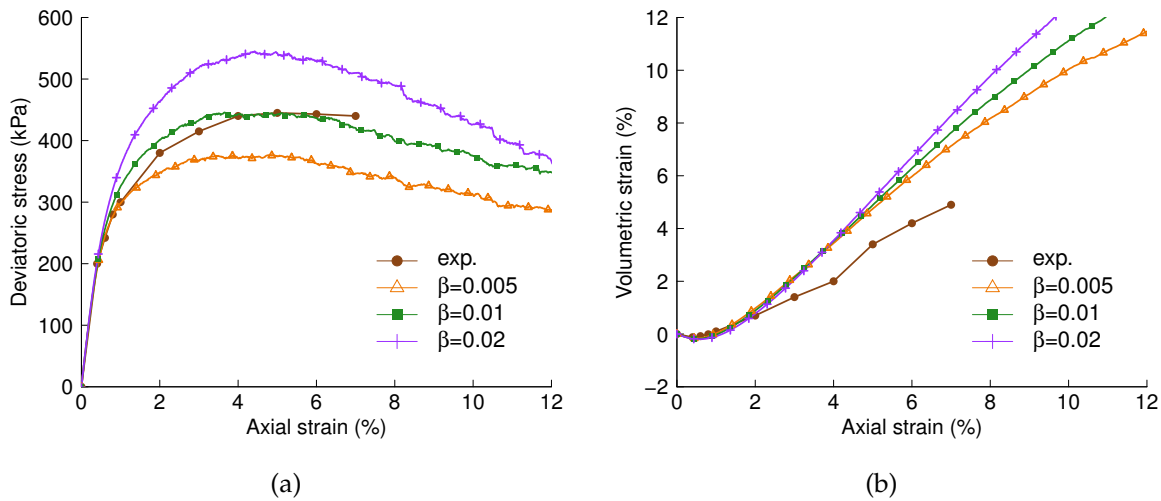


*Figure 3.9:* *Effects of the rolling stiffness coefficient β on (a) Deviatoric stress, (b) Volumetric strain*

Figure 3.9 shows that rolling resistance has no influence on the initial slope of the stress-strain curve, while on the contrary, it is very powerful in changing the peak value of deviatoric stress. Under the same value of rolling elastic limit ($\eta=1.0$), the higher the rolling stiffness parameter, the higher the peak value of the deviatoric stress. On the other hand, the difference of volumetric strains in terms of different $\eta$ is less significant. In addition, the contraction of the volumetric strain at the initial stage of triaxial loading is well captured.

Even though the volumetric strain increases due to the implementation of rolling resistance, the peak value of the deviatoric stress is well captured by adopting a rolling stiffness parameter of 0.01. Due to the fact that capturing the peak value of deviatoric stress is the first priority, the value of 0.01 is taken as the calibrated value of rolling stiffness parameter.

### 3.3.2.7 Effects of rolling elastic limit

The effects of rolling elastic limit are investigated in this part. When $\eta$ takes the value of 0.1, the peak value of deviatoric stress is not reached (Figure 3.10). However, when the value of $\eta$ exceeds the value of 0.5, the influence on the peak stress is very small. This might be due to moment calculation algorithms. For instance, in equation (3.6), the value of bending moment is controlled by both the relative rotation and the normal contact force. Therefore, $eta_b$ has no more effects when it's value is too large. On the other hand, the influence of $\eta$ on volumetric strain is much smaller compared to its effects on deviatoric stress. Therefore, the value of 0.5 is chosen as the calibrated value.
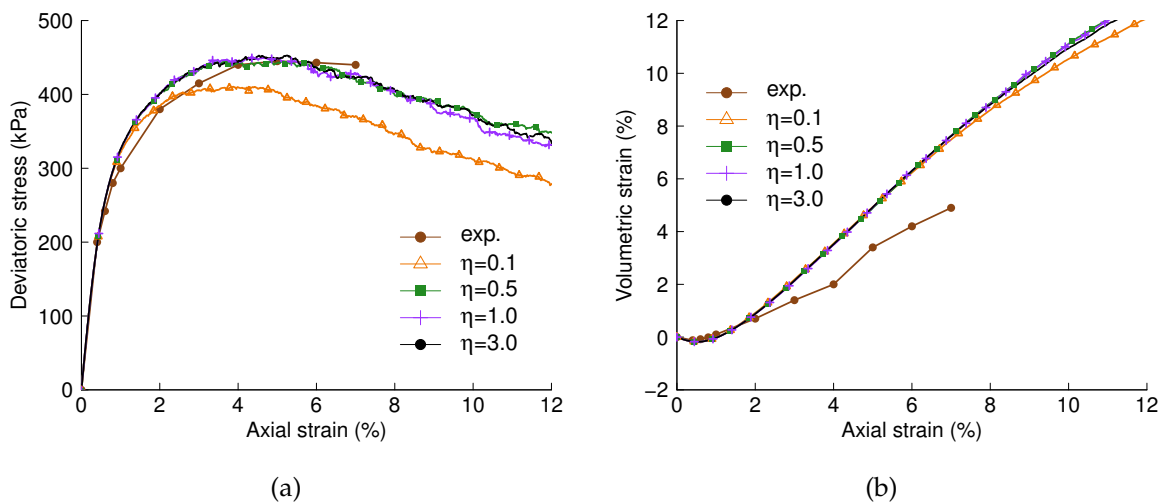


*Figure 3.10: Effects of the rolling elastic limit coefficient $\eta$ on (a) Deviatoric stress, (b) Volumetric strain*

Therefore, by conducting series of tests and varying parameter values, we can understand that the elastic and plastic behaviour of triaxial tests are controlled by different parameters. Normal local modulus $E^n$ and ratio $\alpha$ mainly influence the elastic behaviour of the triaxial test (characterized in terms of the initial slopes of modulus and volumetric strain). Internal friction angle $\phi$, rolling stiffness coefficient $\beta$ and rolling elastic limit coefficient $\eta$ mainly influence the plastic behaviour of the triaxial test (characterized in terms of the peak values of deviatoric stress and the corresponding arriving axial strains, the dilatancy of volumetric strain).

### 3.3.2.8   Calibrated contact parameters

All the parameters have been calibrated based on triaxial test under confining pressure of 100 kPa. The local modulus is $2 \times 10^8$ Pa, the local stiffness ratio is 0.3, the local friction angle is 45°, the rolling stiffness coefficient is 0.01, and the rolling elastic limit coefficient is 0.5 (Table 3.1).

**Table 3.1:** *Values of the calibrated local contact parameters*

| Parameters | Values |
| --- | --- |
| Normal local modulus $E^n$ (MPa) | 200 |
| Ratio $\alpha$ (-) | 0.3 |
| Internal friction angle $\phi$ (°) | 45 |
| Rolling stiffness coefficient $\beta_b(\beta_{tw})$ (-) | 0.01 |
| Rolling elastic limit coefficient $\eta$(-) | 0.5 |

Figure 3.11 shows the curves of deviatoric stress and volumetric strain as functions of axial strain, using the calibrated parameters (Table 3.1). Curves corresponding to the case of without rolling resistance ($\beta = 0$) are plot together to highlight the effects of rolling resistance. Results corresponding to the case of without rolling resistance were obtained using the same $E^n$, $E^s$ and $\phi$ as the case of with rolling resistance.
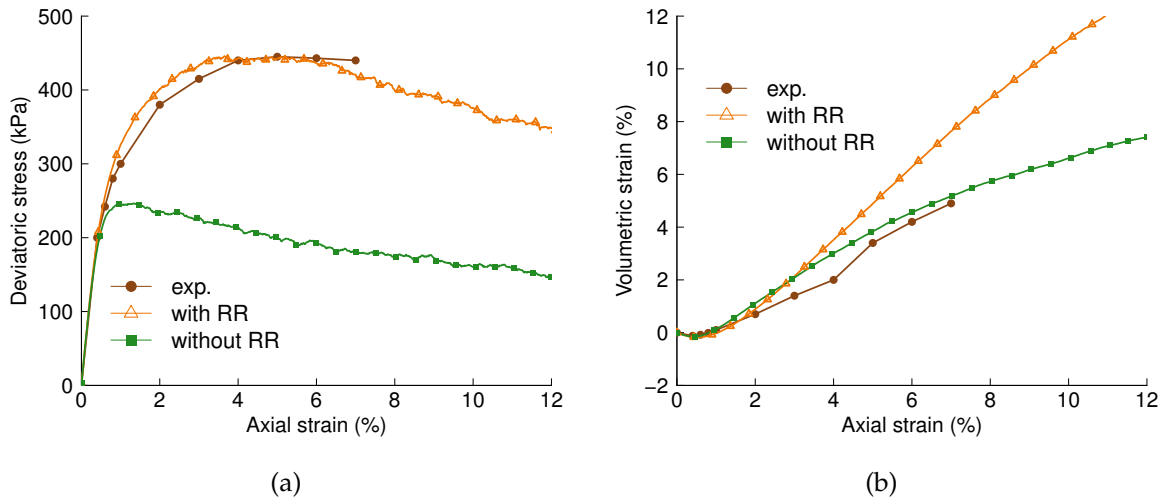
*Figure 3.11: Comparison between the cases of "with" and "without RR" (rolling resistance) in terms of (a) Deviatoric stress, (b) Volumetric strain*

The agreement between simulation results and experiments are good when rolling resistance is considered. While without rolling resistance, the deviatoric stress peak is reached at a smaller axial strain around 2%, and the corresponding deviatoric stress is reduced by about 40% compared to the case with rolling resistance.

The comparison highlights the impressive effects of rolling resistance in increasing the strength and dilatancy behaviour of the soil in classical triaxial tests. In fact, by limiting the relative rotations through rolling resistance, particles are forced to enhance their ability of storing elastic strain energies (Zhou et al., 2013), which improves the stress on the boundaries, and therefore leads to the increase of deviatoric stress and the dilatancy behaviours.

One thing to keep in mind is that the results without rolling resistance shown here are only to demonstrate the important effects of the rolling resistance in improving the deviatoric stress of the sand. The sand without rolling resistance is not calibrated to fit best with the experimental results, in fact, the peak stress can be improved by changing the grain size distribution of by improving the relative density (Salot et al., 2009).

### 3.3.3  Contact law validation

The calibrated parameters are used to conduct triaxial tests under confining pressure of 200 kPa and 300 kPa for validation. Figure 3.12 shows that the peak values of deviatoric stresses under 200 and 300 kPa of confining pressures are well captured. The dilatancy produced in the modelling is bigger than experimental results. This might be due to the fact that the sample produces large pressure in the lateral boundaries. Therefore, the lateral boundaries have to move outward in order to maintain the constant lateral confining pressures. Anyway, the calibrated parameters are considered satisfying enough to model of a sand specimen response.



(a)                                        (b)
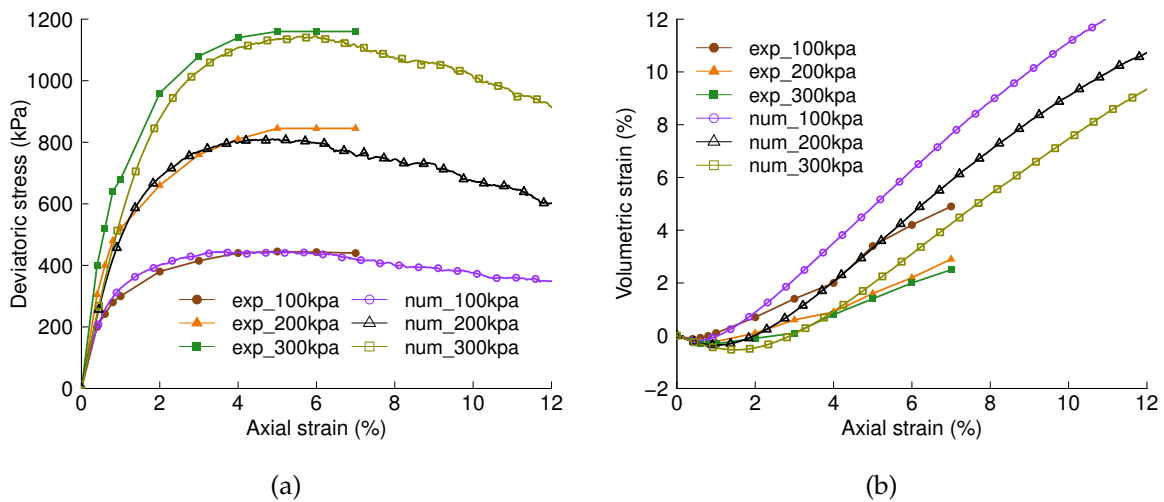
***Figure 3.12:*** *Evolution of (a) Deviatoric stresses, (b) Volumetric strains under the confining pressures of 100 kPa, 200 kPa and 300 kPa*

## 3.4  Impact simulation

This section focuses on modelling the dynamic interaction of a boulder falling on a granular layer. The dynamic modelling uses the same contact law and same contact parameters as the one calibrated under quasi-static triaxial loading. Since no exhaustive energy dissipation theories have been well established in real systems, frictional processes is considered to be the most important approach to dissipate energies, only

frictional energy dissipation is considered thereafter. The numerical results will be compared with results from literature for model validation purpose. The validation of the model permits us to conduct further investigations to understand the mechanisms that govern the reaction of the boulder and the response of the granular medium.

At a first approach, the model is simplified by allowing a boulder vertically impacting a granular medium with an initial incident velocity. This granular medium is relevant for part of a slope (natural or man-made) or a protection structure (earth embankment for instance), characterized by highly heterogeneous and weakly cohesive properties. For evident computational reasons, the medium only represents parts of a slope or a protection structure that is influenced by the impact, instead of the whole slope or the whole structure. At the same time, the sample is generated large enough to avoid lateral boundary effects on the reaction of the boulder. The effects of bottom boundary will be discussed in chapter 4.

### 3.4.1   Modelling of a falling boulder interacting with a granular medium



(a)                                                                 (b)
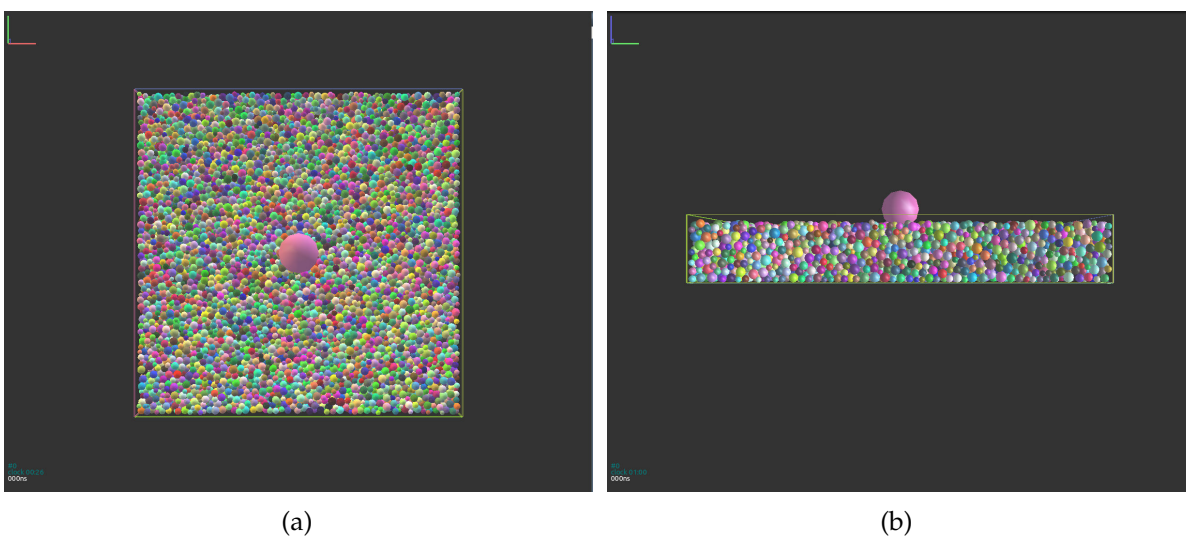
*Figure 3.13: Modelling of the boulder and the granular medium*

Figure 3.13 shows the modelling of the granular medium and the falling boulder in DEM. The boulder is modelled as a sphere with a radius of 1.17 m. It is positioned just above the center surface of the medium, with an initial vertical velocity of 19.23 m/s.

The granular medium is modelled as an assembly of grains obtained by gravity deposition. The grain sizes follow a uniform distribution, with a variability of 33% around the mean value. Sample composed of small grains requires not only large population of grains but also a tiny time step, therefore, in a first modelling approach, particles of big sizes are adopted in order to save computation time. The mean radius of the grain is 0.2 m, thus the ratio of the boulder radius to the average grain radius is 5.85.

During the gravity deposition process, the local friction angle is set at $10°$, and rolling resistance is not considered within the contacts to generate a moderately dense sample. The density of the medium is 1605 kg/m$^3$ when gravity deposition is finished. During the impact process, the granular medium adopts parameters calibrated based on the quasi-static triaxial tests.

The medium leans on a rigid surface, referred as "bottom" hereafter. The size of the sample is 20 m in length and width, 3 m in height (i.e. typically 6-8 particles along the vertical axis). Large enough values of sample length and width are chosen to avoid lateral boundary effects (see section 3.4.2.3). In dynamic impact modelling, we use rigid fixed wall boundaries. No periodic boundary conditions are considered. The parameters of the boulder and the granular medium are given in table 3.2.

## 3.4.2   Validation of the impact modelling

The reaction of the boulder and the response of the medium during the impact are investigated and compared with results from literature for model validation purpose. Under the conditions of normal impact, the main attentions are put on the vertical component of the impact force on the boulder $F_{boul}$, the impact duration $T_{imp}$, the vertical incremental transmitted force on the bottom boundary $\Delta F_{bott}$, the vertical velocity of the boulder $V_{boul}$ and the vertical penetration depth of the boulder $Z_{boul}$.

*Table 3.2: Parameters of the boulder and the granular medium*

| Parameter | Value |
|---|---|
| Sample $length \times width \times height$ | $20\,\text{m} \times 20\,\text{m} \times 3\,\text{m}$ |
| Grain size distribution | $R_{min}/R_{mean}/R_{max}$ |
| | $=0.133\,\text{m}/0.2\,\text{m}/0.267\,\text{m}$ |
| Unit mass of grains | $2700\,\text{kg}/m^3$ |
| Unit mass of boulder | $2700\,\text{kg}/m^3$ |
| Boulder radius | 1.17 m |
| Boulder mass | 18260 kg |
| Boulder impact velocity | 19.23 m/s |
| Boulder impact energy | 3376 kJ |

### 3.4.2.1 Impact force and impact duration
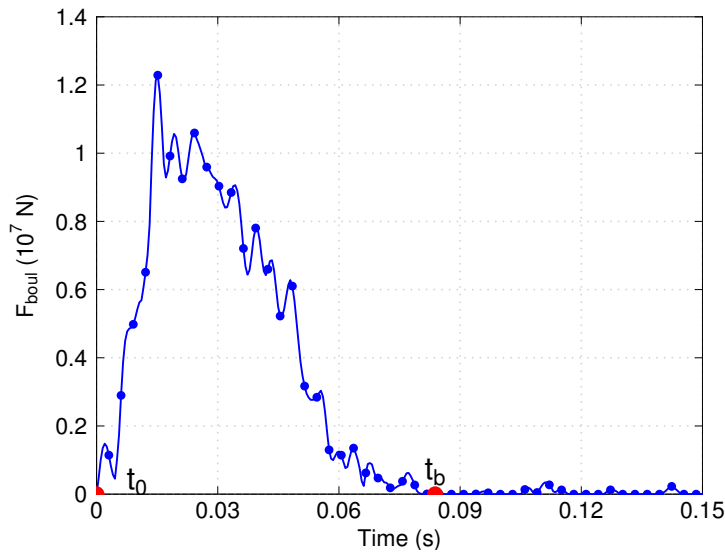


*Figure 3.14: Time evolution of impact force on the boulder $F_{boul}$*

Figure 3.14 shows the evolution of the impact force $F_{boul}$ on the boulder: at the time $t_0 = 0.0$ s, $F_{boul}$ starts to increase, which indicates that the boulder starts to interact with the granular medium; a peak value of $1.22 \times 10^7$ N is reached about 0.015 s after the impact starts; at the time $t_b = 0.083$ s, $F_{boul}$ equals to zero, which indicates that the boulder loses interactions with the granular medium. Therefore, the impact duration $T_{imp}$ is 0.083 s ($T_{imp} = t_b - t_0$).

The results of Pichler et al. (2005) obtained under similar conditions are selected to validate simulation results in terms of the peak value of $F_{boul}$ and $T_{imp}$. To support the design of rockfall protection structures covered with energy-absorbing gravel layers, Pichler et al. (2005) first conducted dimensional analysis to build relations between the penetration depth, the impact duration, and the impact force, respectively, and the rock boulder mass, the height of fall, and the indentation resistance of the gravel. Based on this theory, Pichler et al. (2005) designed rockfall experiments to let rock boulders of approximately cubic shapes hit on a granular layer with a face, an edge, or a tip. The mass of rock boulders was designed up to 20 000 kg. The falling height of boulders was designed up to 20 m. The granular medium was designed as 25 m in length, 4 m in width, 2 m in depth and filled with wide-range grained gravel (the maximum diameter of grains is 0.2 m). The gravel was filled and compacted layer by layer. The obtained experimental results permit to theoretically estimate rockfall events which are beyond the experimental scales.
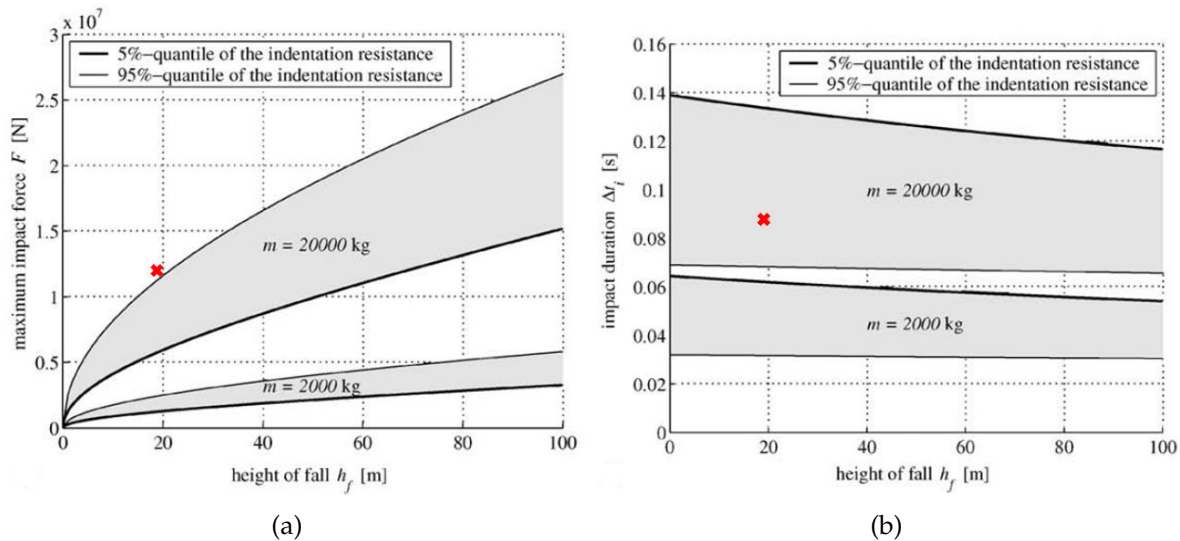


**Figure 3.15:** *(a) Maximum impact force on the boulder, (b) Impact duration obtained in Pichler et al. (2005). The red cross points correspond to the DEM simulation results.*

The comparison between DEM results and the theoretical results of Pichler et al. (2005) is shown in figure 3.15. In case of the peak value of $F_{boul}$, the DEM result is slightly higher. The reason for this may be due to the fact that a spherical boulder is used in the DEM simulation, while their results were obtained based on cubic boulders. Studies in literature indicate that compared to spherical shaped boulders, angular boulders have

a lower peak value of impact force (Degago, 2007; Degago et al., 2008). On the other hand, the comparison of $T_{imp}$ shows a good agreement between the simulation and experiments.

### 3.4.2.2 Dynamic amplification effects

In rockfall dynamic impacts on granular layers, it is well known that dynamic amplification effect exists (Stoffel, 1998; Calvetti et al., 2005). The dynamic amplification effect is defined as: the transmitted stress/force on the bottom is larger than those corresponding to the application of a quasi-static force equal to the peak value of the impact force (Calvetti et al., 2005).

In this study, dynamic amplification effect is checked for model validation purpose. Due to the fact that the resultant force acting on the bottom $F_{bott}$ is dependent on the weight of the medium, and the rockfall protection structure design is more interested in knowing the additional transmitted force on the bottom $\Delta F_{bott}$ rather than $F_{bott}$, the dynamic amplification effect in this study is defined as the ratio of the maximum incremental transmitted force on the bottom boundary $max.\Delta F_{bott}$ to the peak value of impact force $max.F_{boul}$. The incremental transmitted force on the bottom boundary at a time $t$ is defined as $\Delta F_{bott}^{t} = F_{bott}^{t} - F_{bott}^{t_0}$, where $F_{bott}^{t}$ and $F_{bott}^{t_0}$ are the transmitted forces on the bottom at times $t$ and $t_0$ respectively.

Figure 3.16 shows the time evolution of $\Delta F_{bott}$. $\Delta F_{bott}$ keeps constant at the beginning of the impact, and starts to increase approximately at 0.015 s. A peak value of $2.48 \times 10^7$ N is reached at 0.034 s. The peak value is reached 0.019 s later than the peak value of the impact force. The ratio of $max.\Delta F_{bott}$ to $max.F_{boul}$ is 2.1, which indicates that the simulation is able to reproduce the dynamic amplification effect.

The corresponding results of Stoffel (1998) are selected to validate the dynamic amplification effect obtained in the DEM simulation. In order to better understand the damping ability of soil cushion covered on rockfall protection rock sheds, Stoffel (1998) performed series of impact tests at LMR-EPFL of Lausanne to drop falling rock blocks from various heights on a reinforced concrete slab covered by different materials (Stoffel, 1998). The blocks were made of steel shells plugged with concrete. Their shapes were cylinders with spherical bottoms. The mass of the blocks were 100, 500 and 1000 kg, the
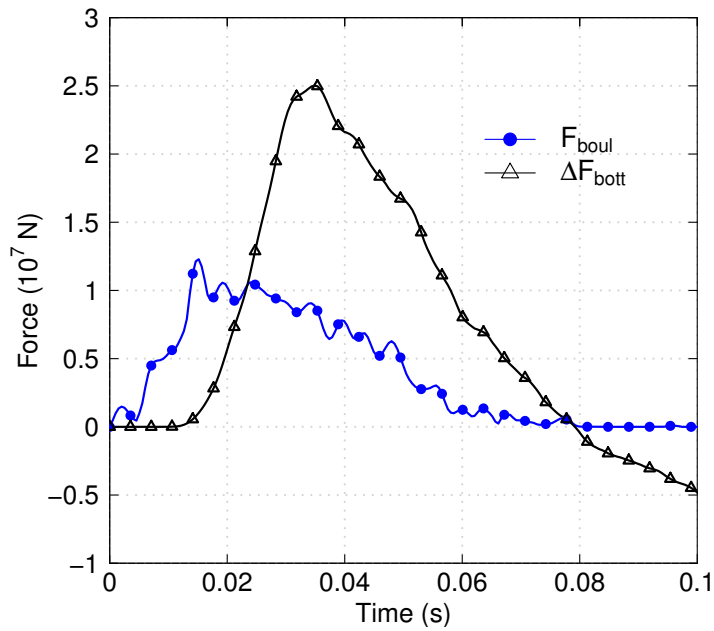
**Figure 3.16:** *Time evolution of impact force $F_{boul}$ and incremental transmitted force on the bottom $\Delta F_{bott}$*
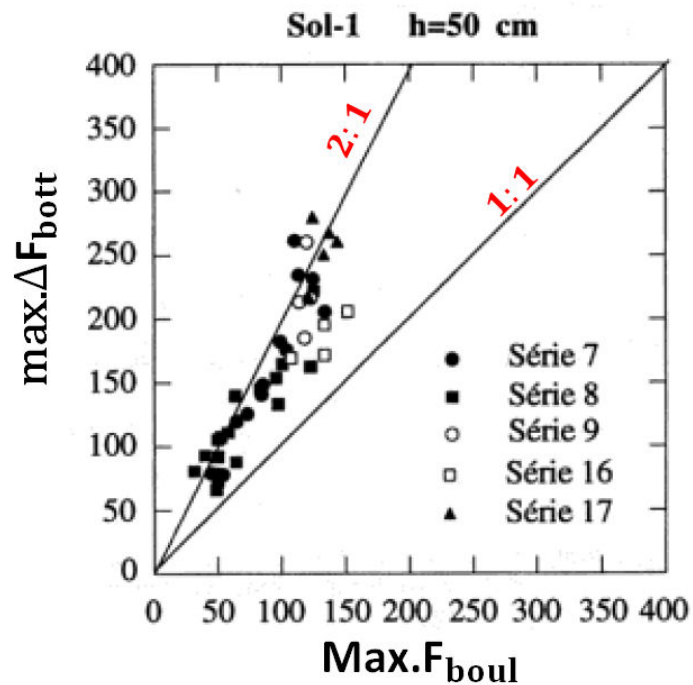


**Figure 3.17:** *Results in terms of the ratio of $Max.\Delta F_{bott}$ to $Max.F_{boul}$ obtained in Stoffel (1998) (page 90)*

falling heights ranged from 0.25 to 10 m. The dimensions of the reinforced concrete plate were 3.4 m $\times$ 3.4 m $\times$ 0.2 m. The thickness of the soil cushion layer ranged from 0.35 m to 1 m.

The ratio of $Max.\Delta F_{bott}$ to $Max.\Delta F_{boul}$ obtained by Stoffel (1998) for the cases of boulders impacting a gravel layer of 0.5 m is shown in figure 3.17. Most data distribute around the value of 2, which is very close to our simulation result (2.1), even though the experiments and the simulation are under different impact conditions.

### 3.4.2.3   Compression wave velocity

The transmitted force on the bottom is related to the propagation of compression waves inside the impacted medium. Moreover, the propagation and reflection of compression waves play an important role in the reaction of the boulder and the response of the granular medium (Calvetti et al., 2005; Bourrier et al., 2008). This part mainly focuses on investigating the velocity of compression waves.

The velocity of compression waves propagating inside the medium is calculated as:

$$V_{wave} = \frac{H}{t_a} \tag{3.21}$$

where, $H$ is the medium thickness; $t_a$ is the time that the compression wave reaches the bottom boundary.

A criterion is adopted to check when the compression waves reach the bottom boundary, that is the incremental value of $\Delta F_{bott}$ exceeds 1% of the $max.\Delta F_{bott}$. Based on this criterion, $t_a = 0.016$ s is obtained. As a result, the velocity of compression waves $V_{wave}$ obtained by equation (3.21) is 200 m/s, which is a common value as cited in the literature (Stoffel, 1998).

Additional lateral boundary effects are checked to insure that the reflected compression waves from lateral boundaries have no influences on the reaction of the boulder. The criterion adopted is that whether the round trip of compression waves finishes later than the impact time:

$$\begin{cases} t_c = \frac{L}{H}t_a > T_{imp}, & \text{no lateral boundary effects;} \\ t_c = \frac{L}{H}t_a \leq T_{imp}, & \text{lateral boundary effects.} \end{cases} \tag{3.22}$$

where, $L$ is the sample length; $t_c$ is the time when the reflected waves come back to the initial impact location of the boulder. The obtained $t_c$ is 0.11 s, which is bigger than $T_{imp}$ (0.083 s). Therefore, no lateral boundary effects are thought to occur in this impact case.

#### 3.4.2.4   Final penetration depth

The vertical component of velocity $V_{boul}$ and penetration depth $Z_{boul}$ of the boulder are recorded to investigate the movement of the boulder (Figure 3.18). $Z_{boul}$ is a relative value with respect to the initial position of boulder. The simulation is run long enough to obtain the final penetration depth of the boulder.

The velocity of boulder $V_{boul}$ starts to become positive at a time of 0.053 s (Figure 3.18). The maximum value of $V_{boul}$ equals 1.28 m/s and is reached at the time of 0.074 s. At the time of $t_b$=0.083 s (when boulder starts to lose contact with the granular medium, figure 3.14), $V_{boul}$ corresponds to a value of 1.23 m/s. During the period from 0.083 s to 0.51 s, $V_{boul}$ varies from positive values to negative values, which indicates that there is no strong interaction between the boulder and the granular medium, or the boulder is just contacting with few flying particles. Starting from the time of 0.51 s, the boulder impacts again on the granular medium with a velocity of -2.5 m/s. Then successive interactions between the boulder and the medium finally lead to $V_{boul}$ equals to zero.

Correspondingly, the penetration depth of the boulder equals to a value of 0.52 m at the time of 0.053 s. Afterwards, the boulder first rebounds and then impacts again the medium at a position of 0.77 m. The corresponding position of the boulder and the medium at the time of 0.053 s and 0.51 s is shown in figure 3.19. It is worth noting that the medium keeps going downward between the two impacts, without the influences of boulder. The settlement of the medium between the two impacts is 8.3% of the medium
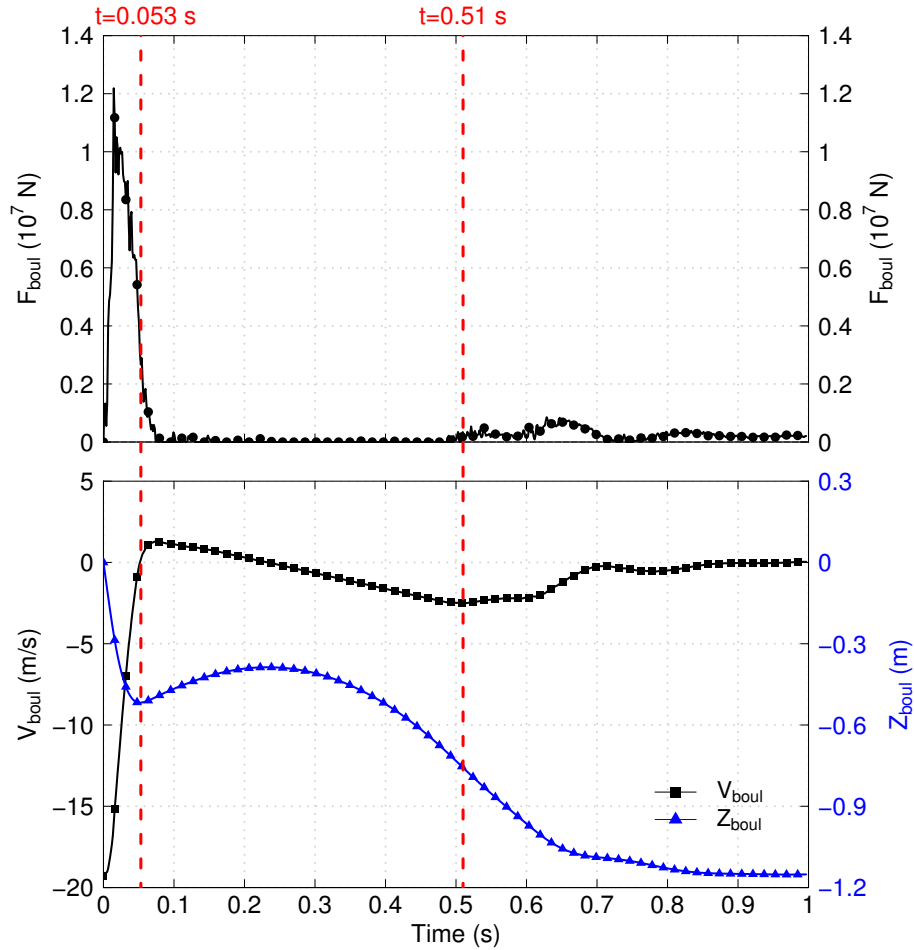
***Figure 3.18:*** *Time evolution of impact force $F_{boul}$, boulder's velocity $V_{boul}$ and Penetration depth $Z_{boul}$*

thickness, and is mainly due to the ejection of grains in the impact neighbourhood (Figure 3.19(b)). The final penetration depth of the boulder inside granular medium is 1.15 m, which is a little bit larger than the results of Pichler et al. (2005) (Figure 3.20). This might be due to the fact that particles eject and the granular medium has strong rearrangements during the impact.

To sum up, the impact force on the boulder, the impact time, the transmitted force on the bottom boundary, the final penetration depth of the boulder are investigated. The agreement between our DEM results and results from literature are satisfying which confirms the validation of the model.

(a)                                              (b)
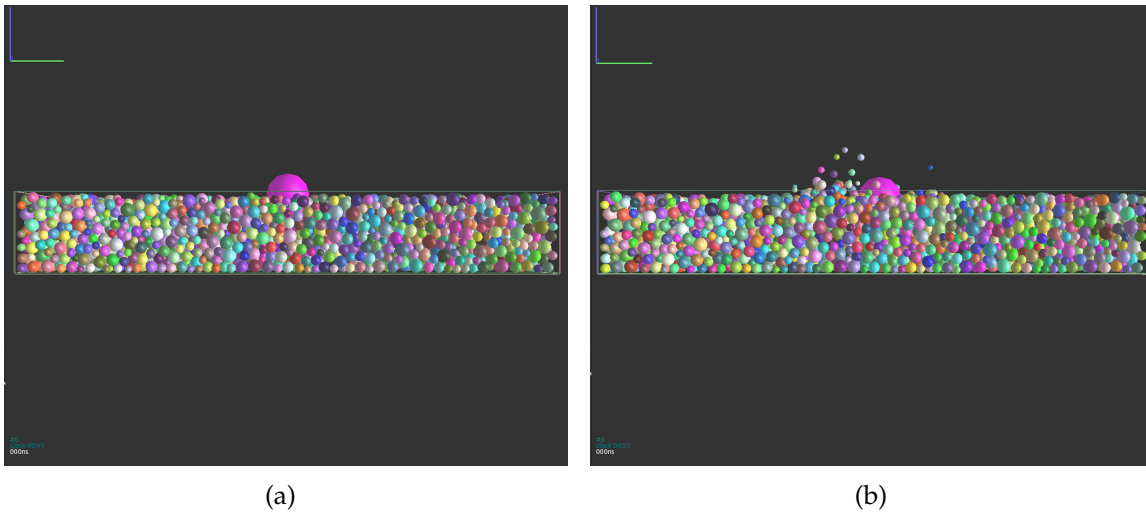
*Figure 3.19:* *Positions of boulder and the granular medium at the time of (a) 0.053 s, (b) 0.51 s*
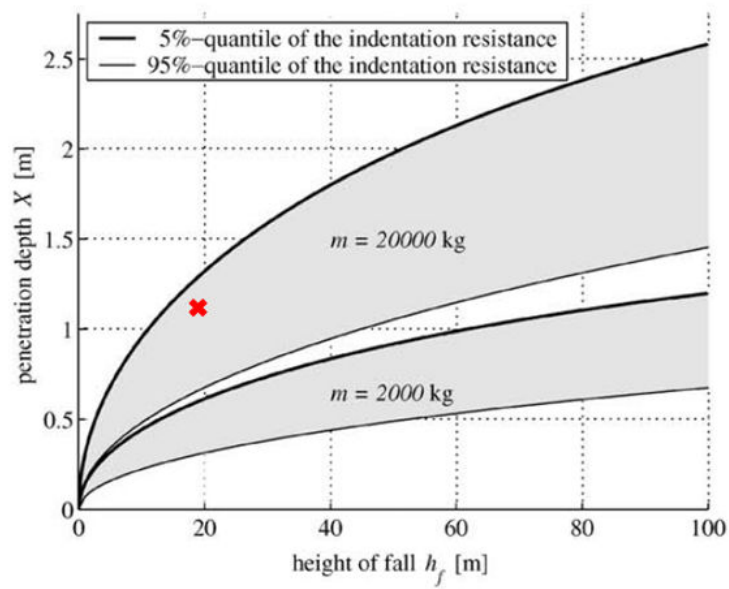


*Figure 3.20:* *Penetration depth obtained in Pichler et al. (2005). The red cross points correspond to the DEM simulation results*

## 3.5   Conclusion

This chapter conducts 3D discrete element modelling of the interaction between a granular medium and a falling boulder. To build this impact model, a contact law is chosen to simulate the behaviour of granular materials. Since no specific dynamic experiment in literature is available for model calibration, an assumption is made that the contact law calibrated under quasi-static triaxial tests can be further used into dynamic impact modelling.

First of all, an elastic-plastic contact law implemented with rolling resistance to consider particle shape effects is chosen as the contact law. Experimental data of quasi-static triaxial loading on angular Ticino sand are adopted to calibrate the contact parameters, since the angular Ticino sand can represent rockfall impacted granular medium, such as natural slopes or protection embankments.

Following a calibration procedure proposed in the literature, the calibration succeeds in finding a series of local contact parameters that allow to reproduce the macroscopic response of Ticino sand under 100 kPa of confining pressure. The match of simulation and experiments under 200 kPa and 300 kPa confining pressures by using the same series of contact parameters validates the calibrated parameters. During the calibration, it is found that particle number has no great influence on the macroscopic behaviour of the granular medium, since there is no inertia effects in quasi-static loading. In addition, rolling resistance is able to account for the particle shape effects. It has important effects in improving the peak stress and the dilatancy properties of the sand.

Secondly, the newly calibrated contact law is applied to simulate the dynamic loading process of a boulder impact a granular medium. The comparison of simulation results and experimental results given in the literature in cases of maximum impact force on the boulder, the impact duration, the finial penetration depth of boulder validates the impact modelling. In addition, the model is shown to be capable of reproducing the dynamic amplification effects.

The validation of the 3D impact model indicates that DEM is capable of modelling the impact of a boulder on a granular medium. Besides, the contact law calibrated by quasi-static triaxial tests is able to be applied in dynamic impact problems. Based on this model validation, further investigation on the response of the granular medium can be conducted.

# Chapter 4

# Global bouncing occurrence of the boulder

## Contents

## 4.1   Introduction

Due to the important role of bouncing in the prediction of rockfall trajectories and the design of protection structures, the objective of this chapter is to investigate the global bouncing occurrence of boulder based on the 3D impact model developed and validated in chapter 3. Parameters concerning boulder sizes and medium thickness are varied.

In addition, local configuration effects and the energy propagation processes inside the impacted medium are primarily investigated, particularly because the bouncing of boulder is closely related to the boulder-medium interaction. More specifically, the investigation of local configuration effects aims at evaluating the variability of the results (impact force and reflected velocity of boulder) with respect to various impact locations, and selecting an appropriate number of simulations whose average value is representative. The energy propagation processes are investigated by analysing the time evolution of kinetic energy, elastic strain energy, coordination number, energy dissipation inside different medium volumes, which helps understanding the response of the medium under impact.

Finally, the bouncing occurrence of boulder with respect to different layer thickness and boulder sizes are obtained by adopting a bouncing criterion. Relations between the bouncing of boulder and the response of the granular medium are discussed.

## 4.2   Variability of the results with respect to impact locations

### 4.2.1   Introduction

Due to the discontinuity of granular materials, the impact processes are closely related to the local configurations (Bourrier et al., 2008). In order to check the local configurations of the impact model, simulations of two identical boulders vertically impacting a granular medium corresponding to two different impact locations are conducted. The granular medium is the same as the one validated in chapter 3, with a maximum grain size ratio of 2. The two impact location points are selected without having lateral boundary effects. Figure 4.1 shows that the impact forces and the velocities of boulder with respect to the

two impact locations are different, not only in the peak values, but also in the arriving times of the peak values. Particularly, the impact force peak is $1.42 \times 10^7$ N and $1.20 \times 10^7$ N corresponding to location $A$ and $B$ respectively, the maximum velocity is 1.50 m/s and 0.61 m/s corresponding to location $A$ and $B$ respectively.



(a)                                                                                    (b)
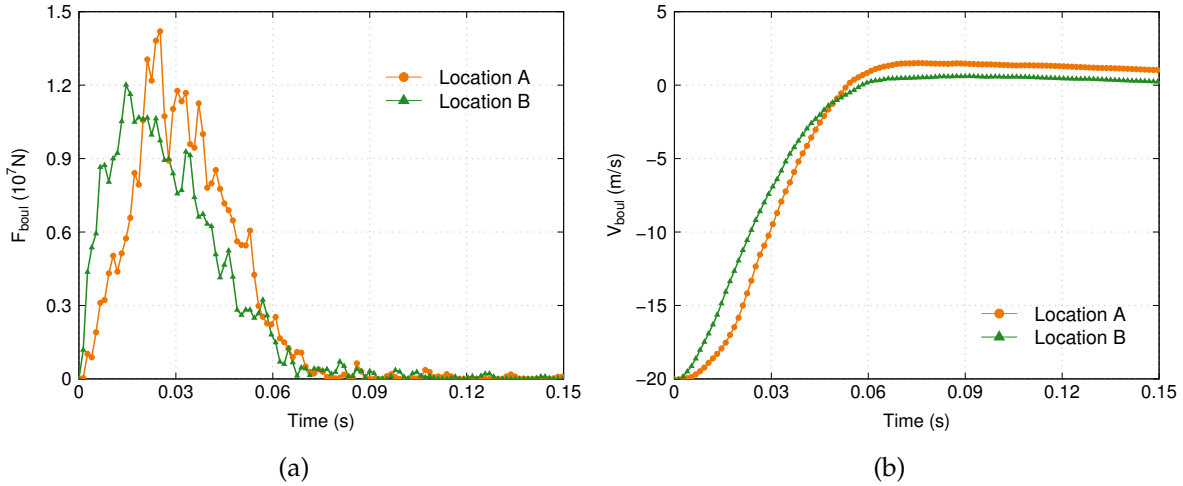
**Figure 4.1:** *Variability of results in terms of (a) Impact force on the boulder $F_{boul}$, (b) Vertical velocity of boulder $V_{boul}$ with respect to two locations. In this case, the radius of the boulder is 1.2 m, the layer thickness of the granular medium is 3 m*

Therefore, when examining the bouncing occurrence of boulder impacting a granular medium, it is necessary to know the variability of the simulation results with respect to impact locations, and to have an idea about how many simulations are necessary to have the representative average reaction of the boulder. Under the condition of normal impacts, the reaction of boulder mentioned here mainly concerns the maximum vertical impact force on the boulder $max.F_{boul}$ and maximum vertical component of the boulder velocity $max.V_{boul}$.

Despite this requirement, no exhaustive investigations conducted upon the variability of results with respect to impact locations have been found in the literature. Only few works in the literature consider the local configuration effects. For instance, in the work of Bourrier et al. (2008), the evolution of the mean value and the standard deviation of the reflected kinetic energy of the boulder versus the number of simulations were investigated. The results indicated that 100 locations with a 0.05 m distance apart can

insure a stable mean value and standard deviation of the reflected kinetic energy of the boulder. However, this is a rough estimation, besides, the evolution of mean value and standard deviation is dependent of the randomization of the impact locations.

## 4.2.2   Methodology

This work interests in knowing the minimum number of simulations to be conducted in different impact conditions, such as various boulder sizes and various layer thickness. It is supposed that the the number of simulations for the case of $R_b = R_m$ ($R_b$ is the radius of boulder, $R_m$ is the average radius of particles inside the medium), will also be relevant for cases of $R_b > R_m$, based on the assumption that the number of simulations required depends on the ratio of $R_b/R_m$: the larger the ratio of $R_b/R_m$, the smaller the variability of the results. The influence of layer thickness on the variability of the results is not considered, the investigations are conducted based on a layer thickness of $15R_m$.

In order to overcome lateral boundary effects, the impact locations of boulder are all located on a center surface of 2 m × 2 m area (the length of the area is 10% of the medium length). Moreover, the area is uniformly divided into $a \times a$ grids, with $a$=2, 3, 4, ..., the impact locations are all located on the grid nodes. Therefore, the number of simulations, $n$, equals to 9, 16, 25, 36, 49, ... (Figure 4.2).

The reference case corresponds to 400 number of impact simulations. This number of simulations is supposed to be sufficient to capture the average reaction of the boulder. In order to achieve the goal of selecting an appropriate number of simulations that compromises between the average reaction of boulder and the computation time, first of all, the variability and the distribution of results with respect to various number of simulations are examined; second, a statistical tool is used to select a smaller number of simulations which supports the hypothesis that there is no significant difference between the corresponding mean value $\overline{x_1}$ and the mean value of the reference case $\overline{x_2}$.
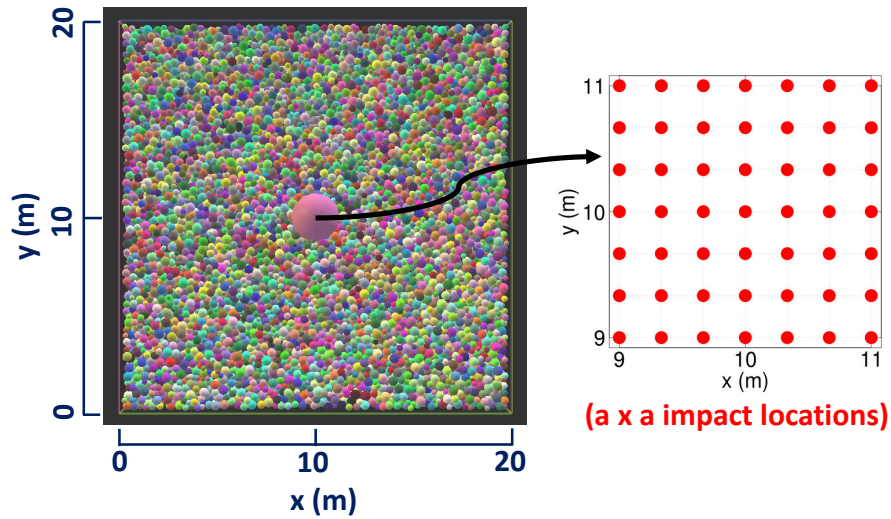
**Figure 4.2:** *n number of impact locations on the center surface area of 2 m × 2 m, n = a², with
a = 2, 3, 4, ..., 20.*

## 4.2.3   Results

The distributions of simulation results are examined in this section by using a Shapiro-Wilk test. Based on this, a student's t-test is adopted to select the number of simulations whose average value shows no significant difference from the reference case. Afterwards, the number of simulations selected is adopted for other impact cases which are demonstrated in section 4.4 and section 5.3.1.

### 4.2.3.1   Normality of the distributions

Figure 4.3 shows the probability density distributions of $max.F_{boul}$ and $max.V_{boul}$ for 400 simulations and 49 simulations as two examples. Detail information of the distribution for $n$ number of simulations are shown in table 4.1.
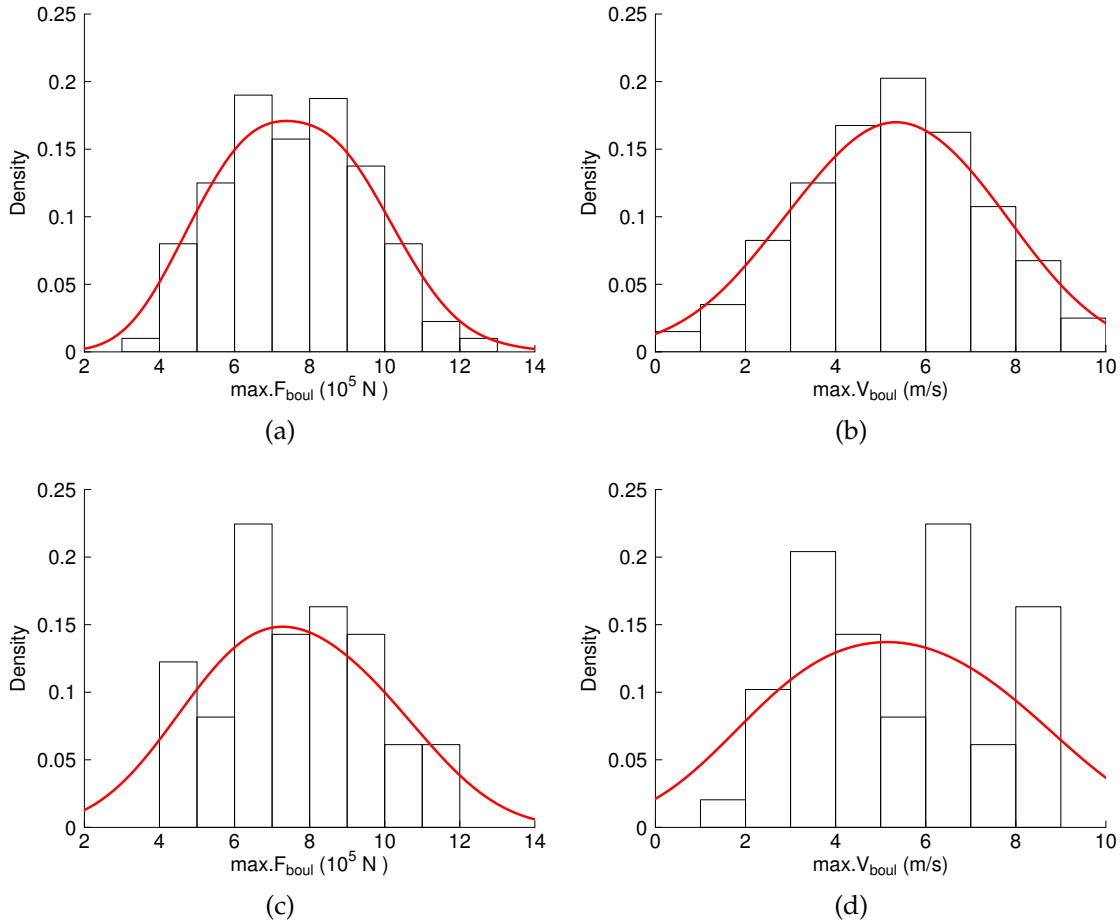
***Figure 4.3:*** *Probability density distributions of (a) Maximum impact force on the boulder* max $F_{boul}$, *(b) Maximum reflection velocity of boulder* max $.V_{boul}$ *of 400 simulations; Probability density distributions of (c)* max $.V_{boul}$, *(d)* max $.V_{boul}$ *of 49 simulations. The red curves are density estimates along the histograms*

Table 4.1 indicates that, for the case of $max.F_{boul}$, the average value out of $n$ number of simulations varies from 7.3-7.7 $\times 10^5$ N, the ratios of standard deviations to the average values are around 20-30%; for the case of $max.V_{boul}$, the average value varies from 5.28-5.73 m/s, the ratios of standard deviations to the average values vary around 32-43%. There is no clear trend showing which number of simulations have the results (average value and standard deviation) most close to the reference case.

*Table 4.1:* Average value $\overline{x_n}$, standard deviation $s_n$ as well as the p-values of Shapiro-Wilk normality tests for $n$ number of simulations

| $n$ (number of simulations) | max .$F_{boul}$ | | | max .$V_{boul}$ | | |
| :---: | :---: | :---: | :---: | :---: | :---: | :---: |
| | $\overline{x_n}$ ($10^5$ N) | $s_n/\overline{x_n}$ | p-value | $\overline{x_n}$ (m/s) | $s_n/\overline{x_n}$ | p-value |
| 9 | 7.7 | 0.247 | 0.542 | 5.723 | 0.318 | 0.457 |
| 25 | 7.5 | 0.221 | 0.265 | 5.618 | 0.403 | 0.839 |
| 36 | 7.3 | 0.297 | 0.231 | 5.504 | 0.430 | 0.557 |
| 49 | 7.6 | 0.261 | 0.266 | 5.309 | 0.392 | 0.041 |
| 64 | 7.6 | 0.251 | 0.560 | 5.332 | 0.353 | 0.434 |
| 400 | 7.6 | 0.247 | 0.001 | 5.279 | 0.383 | 0.564 |

In addition, the Shapiro-Wilk test (Shapiro and Wilk, 1965; Razali and Wah, 2011) is used to check the normality of the data (Table 4.1). The test rejects the hypothesis of normality when the p-value is less than or equal to a cutoff value, 0.05 for instance. Failing the normality test indicates that with 95% confidence the data does not fit the normal distribution. On the other hand, passing the normality test only indicates that no significant difference from normality is found.

Although a p-value of 0.001 is obtained in terms of $max.F_{boul}$ in the reference case (This is due to the fact that the Shapiro-Wilk test is biased by sample size, large samples may be statistically different from a normal distribution (Wilk and Gnanadesikan, 1968)), generally p-values given in table 4.1 indicate that the Shapiro-Wilk test does not significantly reject the hypothesis of normal distributions. Therefore, the following student's t-test which is based on normal distribution hypothesis can be adopted to select the appropriate number of simulations.

### 4.2.3.2   Student's t-test

In order to select a small number of simulations $x_1$ whose average value is not significantly different from the reference case $x_2$, a statistic tool of Student's t-test is used, based on the previous conclusion that the distributions of $n$ number of simulation results are normal.

Student's t-test is one of the most commonly used tools to test the difference between two sample means. The test determines whether two populations are the same within a given level of confidence. A confidence interval for the difference between two means specifies a range of values within which the difference between the means of the two populations may lie (Easton and McColl, 1997).

The confidence interval for the difference between two mean values is given by

$$\mathbf{CI} = (\overline{x_1} - \overline{x_2}) \pm t^* \sqrt{\frac{s_1^2}{n_1} + \frac{s_2^2}{n_2}} \tag{4.1}$$

where $s_1$ and $s_2$ are the standard deviation for the two populations respectively, $t^*$ is the upper $\frac{1-C}{2}$ critical value for the $t$ distribution with $k$ degrees of freedom, with k equals to the smaller value of $n_1 - 1$ and $n_2 - 1$, C equals to 0.95. If the confidence interval includes 0 we can conclude that there is no significant difference between the means of the two populations, at a given level of confidence (Neyman, 1937; Easton and McColl, 1997).

The comparison between the two mean values for $n$ simulations and the reference 400 simulations in table 4.2 indicates that, for a 95% of confidence interval, there is no significant difference between the average values, for all the cases of $n \leq 64$. However, the intervals decrease with the increase of simulation numbers (Table 4.2). A percentage value $p$ is defined as:

$$p = \frac{t^* \sqrt{\frac{s_1^2}{n_1} + \frac{s_2^2}{n_2}}}{\overline{x_2}} \times 100\% \tag{4.2}$$

Table 4.2 shows $p$ decreasing with the increase of simulation number, which indicates that the larger the number of simulations, the smaller the significance from the reference case. Based on this, a number of 49 simulations is selected that compromises best between the representative average reactions and the computational time. Therefore, the number of 49 impact simulations is applied to impact cases with different layer thickness and boulder sizes.

*Table 4.2: Confidence intervals between n number of simulations and the reference case*

| Pair of simulations | max $F_{boul}$ | | max $V_{boul}$ | |
|---|---|---|---|---|
| | CI ($10^7$ N) | p (%) | CI (m/s) | p (%) |
| 9-400 | [-0.011, 0.013] | 19.5 | [-0.701, 1.589] | 26.9 |
| 25-400 | [-0.006, 0.005] | 9.4 | [-0.455, 1.132] | 18.1 |
| 36-400 | [-0.009, 0.003] | 10.0 | [-0.463, 0.913] | 15.7 |
| 49-400 | [-0.005, 0.005] | 7.9 | [-0.497, 0.557] | 12.0 |
| 64-400 | [-0.005, 0.004] | 6.7 | [-0.375, 0.480] | 9.7 |
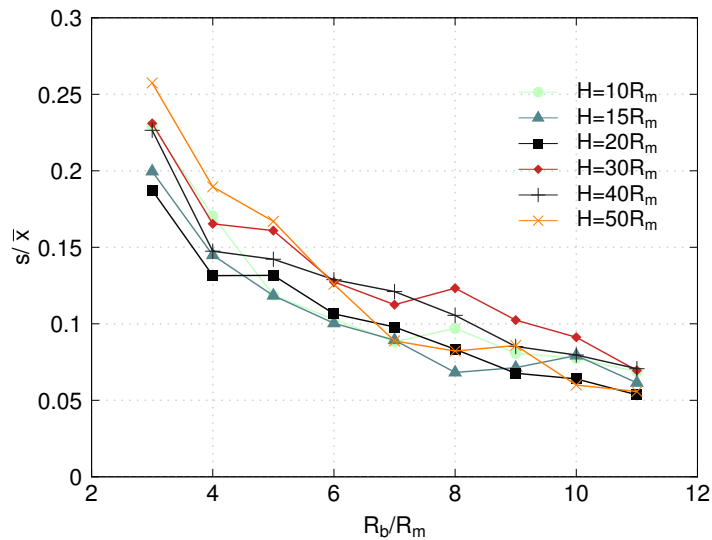


*Figure 4.4: Evolution of $s/\overline{x}$ (the ratio of the standard deviation to the mean value, for the case of maximum impact force on the boulder) versus $R_b/R_m$*

Based on the results of 49 simulations, the ratio of standard deviation to the mean value decreases with the increase of the ratio $R_b/R_m$ (Figure 4.4), which confirms the assumption that the variability of the results decreases with the increase of $R_b/R_m$.

## 4.3   Energy propagation inside the granular medium

Kinematics and energy propagations inside the impacted medium are important issues which help understand the boulder-medium interactions. The aim of this section is to understand the response of the impacted medium through energy propagation (elastic strain energy, kinetic energy, energy dissipation) processes as well as the grain rearrangements (coordination number) inside the medium, based on a detailed medium division approach. Based on this, relations between the energy propagation process and the bouncing of boulder will be further discussed. In this section, the results will be first demonstrated and the interpretation of the results will be conducted afterwards.

### 4.3.1   Layer division

The granular medium is first divided into several crown volumes according to their distance from the impact point (Figure 4.5). Second, each crown volume is divided into a lateral part and a central part due to their different loading and boundary conditions. Particularly, in the studies of Stoffel (1998), a load diffusion angle inside the granular medium is found between 33° to 47° (Figure 4.5(a)), for the case of non-compacted soil. Therefore, a angle of 90° is adopted for central volumes (Figure 4.5(b)). Due to the limited number of particles and too important particle rearrangements, the physical processes involved inside an initial crown which is just below the impact point are not investigated.



(a)          (b)
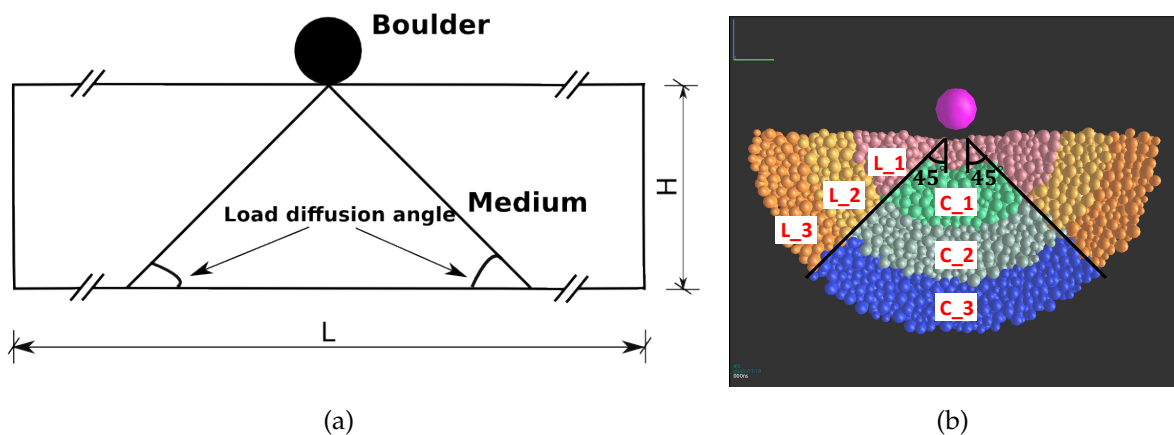
*Figure 4.5: (a) Load diffusion angle, (b) Layer division for an impact case of a 4 $R_m$ boulder radius and 40 $R_m$ layer thickness*

The energy propagation process within the impacted granular medium is investigated from crown to crown based on a specific impact case: the radius of boulder $R_b = 4R_m$, the initial impact velocity is 20 m/s, the initial kinetic energy of the boulder is 1158 kJ. The thickness of the impacted medium is $40R_m$ (each crown volume is of 5-6 particle in thickness). The number of particles in lateral volumes L_1, L_2, L_3 are 1146, 3174, 6325 respectively, the number of particles in the central volumes C_1, C_2, C_3 are 645, 1703, 3319 respectively. Basically, the sample needs at least 2-3 s to be stable after the impact. However, we suppose that energy propagations within the initial period of 0.2 s are the most interesting parts. Therefore, energy propagations within the initial 0.2 s are considered.

## 4.3.2   Evolution of kinetic energy $E_k$ and elastic strain energy $E_s$

Kinetic energy $E_k$ and elastic strain energy $E_s$ are recorded inside each crown volume to investigate the energy exchange and transfer processes. Generally, several phenomena are observed:

- Time delay of the increases in energies from crown_1 to crown_3

  In lateral volumes, the increase in $E_k$ is time delayed, which starts at 0.012 s, 0.024 s, and 0.036 s for volume L_1, L_2, L_3 respectively. In addition, the initial $E_k$ of each volume is zero, since the medium is in quasi-static state before being impacted (Figure 3.8(a)). Similarly, the increase of $E_s$ is time delayed. On the other hand, the initial $E_s$ inside each volume is not nil (the medium is compressed under gravity), they are 0.74 kJ, 5.5 kJ, 19.0 kJ for volumes L_1, L_2, L_3 respectively (Figure 3.8(b)). Same trend of time delay is observed in central volumes (Figure 3.8(c-d)). The difference is that the initial $E_s$ are 1.7 kJ, 11.0 kJ, 37.9 kJ for volumes C_1, C_2, C_3 respectively, which are approximately twice larger than that in lateral volumes.

- Reduction of peak values of energy increments from crown_1 to crown_3

  In lateral volumes, there is a reduce of peak values of incremental $E_k$ and incremental $E_s$ from volumes L_1 to L_2 to L_3, the peak values of incremental $E_k$ are 78.3 kJ, 20.9 kJ, 7.6 kJ respectively; the peak value of incremental $E_s$ are 35.3 kJ, 19.74 kJ and 15.5 kJ respectively. In central volumes, same trends of reduction of
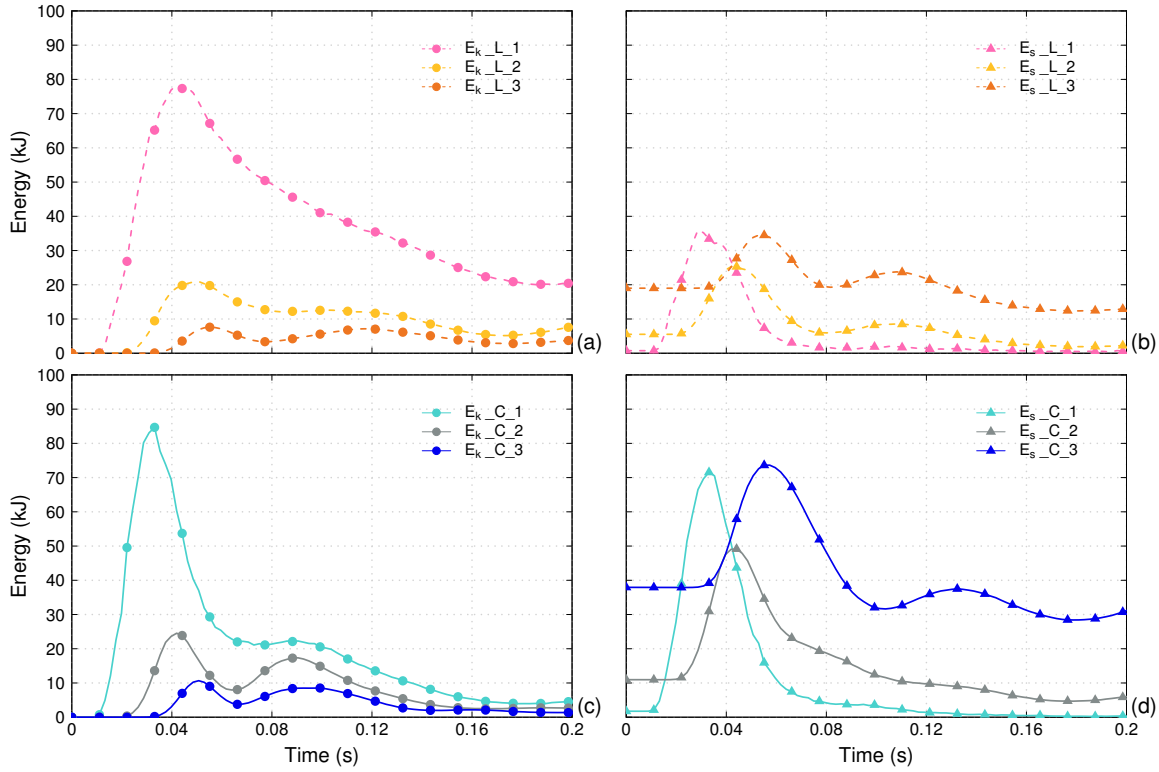
***Figure 4.6:*** *Time evolution of kinetic energy $E_k$ and elastic strain energy $E_s$ inside each volume*

incremental peak values from volumes C_1 to C_2 to C_3 is observed: the peak values of incremental $E_k$ are 84.7 kJ, 24.5 kJ, 10.7 kJ respectively; the peak values of incremental $E_s$ are 69.8 kJ, 38.2 kJ and 35.7 kJ respectively. It is worth noticing that the peak values of the incremental $E_s$ are around twice larger than that in lateral volumes, although the number of particles in central volumes are less than lateral volumes.

● The relation of incremental $E_k$ and incremental $E_s$ to the initial value of $E_s$

Three ratios are defined: $\lambda_a$ is the ratio of maximum incremental $E_s$ to the initial $E_s$ value; $\lambda_b$ is the ratio of the maximum incremental $E_k$ to the initial $E_s$; $\lambda_c$ is the ratio of maximum incremental $E_k$ to the maximum incremental $E_s$. In lateral volumes successively from L_1 to L_2 to L_3, $\lambda_a$ is 47.4, 3.6 and 0.8 respectively, $\lambda_b$ is 105.3, 3.8 and 0.4 respectively, $\lambda_c$ is 2.2, 1.1, 0.5 respectively. In central volumes

successively from C_1 to C_2 to C_3, $\lambda_a$ is 39.9, 3.5 and 0.9 respectively, $\lambda_b$ is 48.5, 2.2 and 0.3. $\lambda_c$ is 1.2, 0.6, 0.3. The ratios have decreasing trends from crown_1 to crown_3. In addition, the ratios obtained in central volumes are smaller than those in lateral volumes.

- Second peak of $E_k$ and $E_s$

In addition, two peaks are observed, especially for $E_k$ curves shown in figure 4.6 (c). The ratios of second peak value to the first peak value are 0.26, 0.7, 0.8 for crown C_1, C_2, C_3 respectively. The second peak is observed more easily in the crown_3 than that in the crown_2 and crown_1.

- Correlation of $E_k$ and $E_s$

The energy in lateral and central volumes are plot together to analyse the correlations of $E_s$ and $E_k$ (Figure 4.7). It is found that: first of all, inside each crown , the increases in $E_k$ and $E_s$ for both lateral volume and central volume start at the same time, the peak values of $E_s$ in lateral volume and central volume arrive nearly at the same time. Second, in central volumes, peaks of $E_s$ and $E_k$ arrive at the same time, while in lateral volumes, peaks of $E_s$ arrives earlier than $E_k$. Correspondingly, the peak value of $E_k$ in central volume is always reached earlier than that in the lateral volume.

### 4.3.3   Evolution of coordination numbers

In order to study the kinematics of the the impacted medium, the evolution of coordination number inside each volume is investigated (Figure 4.8). It shows that initially the sample is moderately dense with coordination numbers among 3.5 - 4.5, while after being influenced by the impact, a rapid and important decrease in coordination numbers is induced. Similar to the evolution of $E_k$ and $E_s$, the drop in coordination number is time delayed. The minimum coordination number is 0.5, 1.9, 3.0 for volume L_1, L_2, L_3 respectively, the minimum coordination number is 0.9, 2.5, 3.5 for volume C_1, C_2, C_3 respectively. The drop in coordination number is less significant for crowns located at increasing distances from the impact point. In the same crown, the drop in coordination number is more significant in lateral volumes than that in central volume.
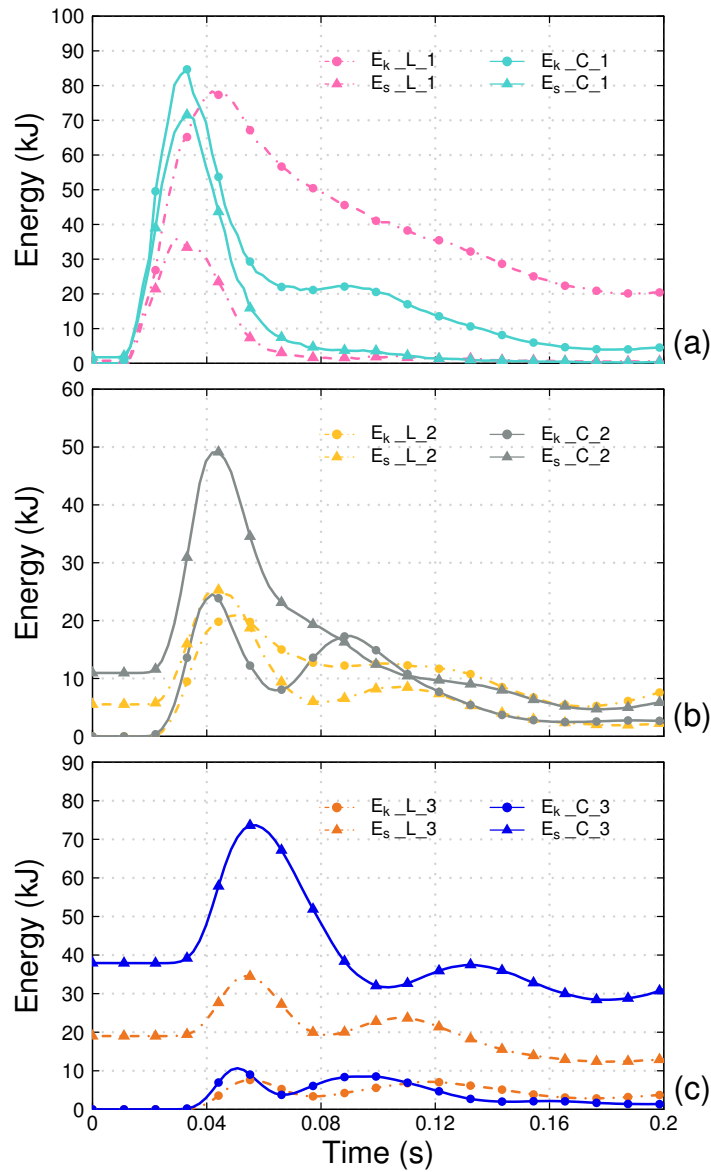
**Figure 4.7:** *Time evolution of kinetic energy $E_k$ and elastic strain energy $E_s$ inside each volume*

## 4.3.4 Evolution of incremental energy dissipation

Figure 4.9 shows the amount of incremental energy dissipation by frictional sliding and frictional rolling inside each volume (frictional rolling includes both frictional bending and frictional twisting).
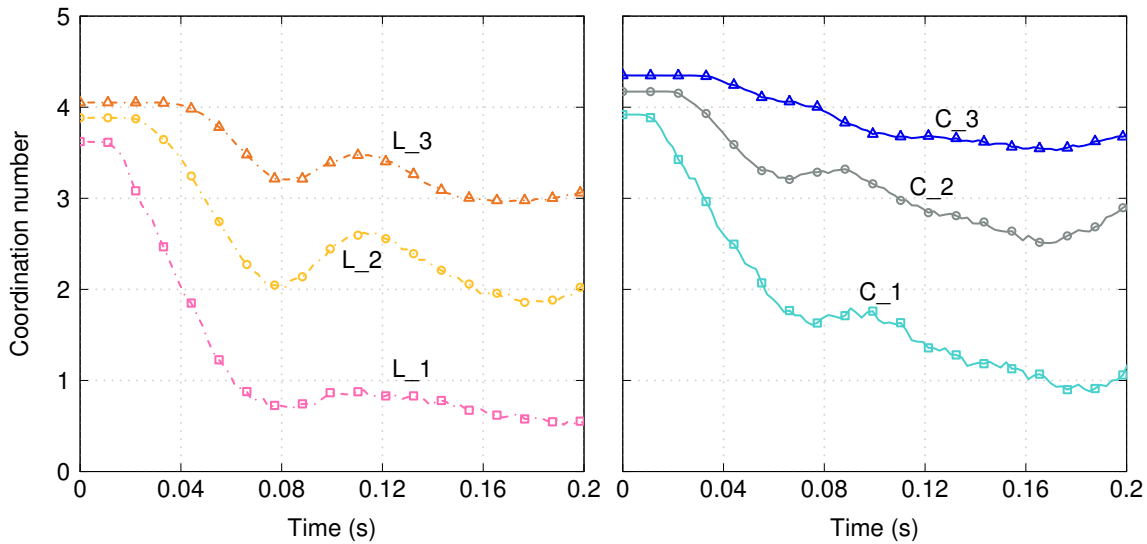
*Figure 4.8:* Time evolution of coordination numbers inside each volume

The magnitude of incremental energy dissipation decreases from crown_1 to crown_3, even though the number of particles in crown_3 is much larger than that in crown_1. Inside each volume, the amount of incremental energy dissipation by frictional sliding is much larger than that by frictional rolling (Figure 4.9). The ratio of the maximum energy dissipation by sliding to that by rolling is 1.5, 2.2, 3.4 in volume L_1, L_2, L_3 respectively, and is 2.6, 4.5, 9.5 in volume C_1, C_2, C_3 respectively. In addition, the peak value of energy dissipation by frictional rolling reaches slightly later than that by frictional sliding.

In addition, till the time of 0.2 s, the sum of energy dissipation within the three crown volumes is 355.1 kJ which is 50.5% of the sum of energy dissipation within the whole sample (702.6 kJ). Therefore, occupying 33.5% of the total sample volume, the crown volumes play an important role in energy dissipation.

Figure 4.10 indicates that the number of frictional sliding contacts are much larger than frictional rolling contact number. The ratio of maximum sliding contacts to the maximum rolling contacts inside each volume is around 10 to 20. Besides, the peak value of rolling contact number is reached slightly later than that of sliding contact number.
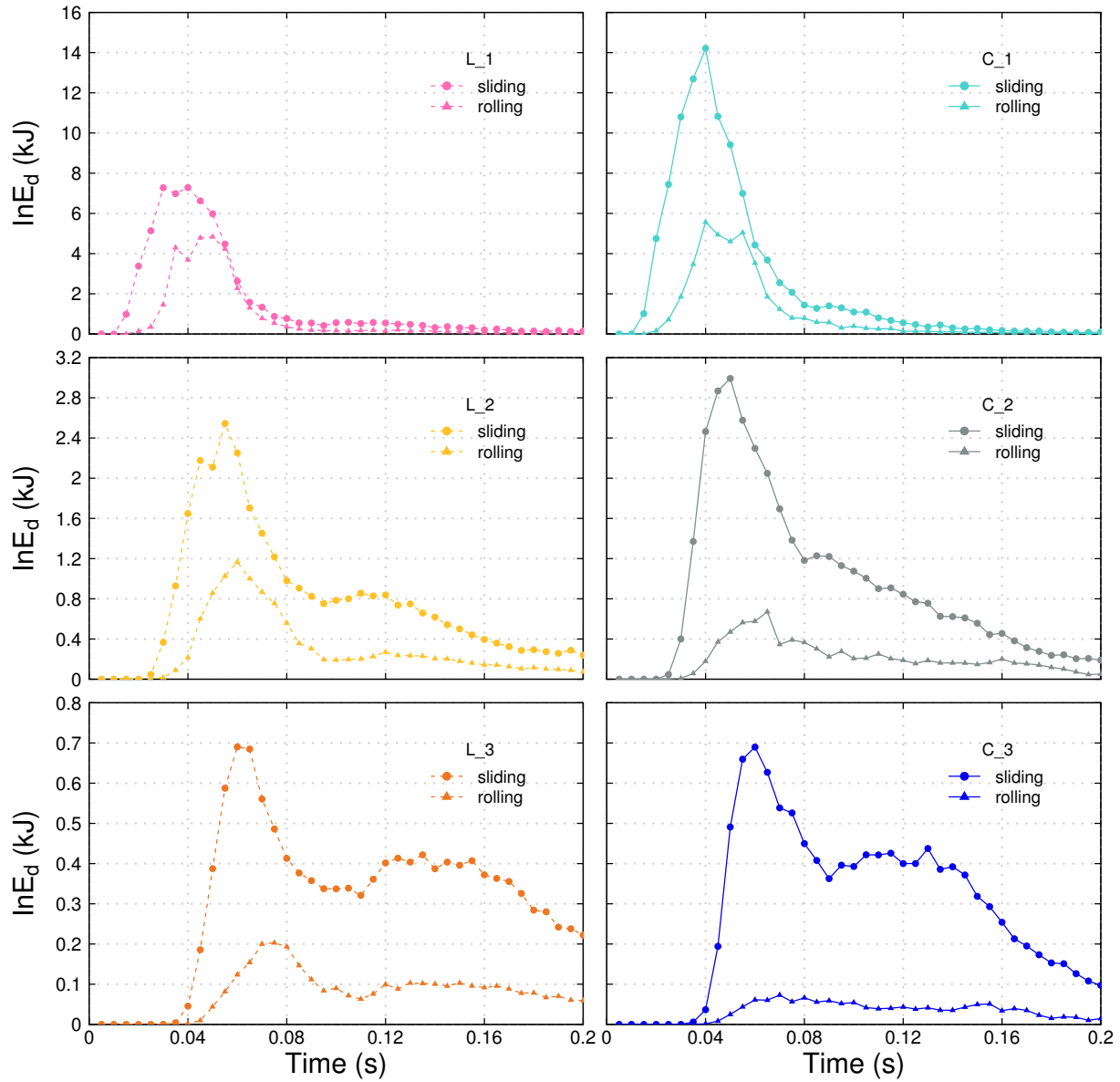
***Figure 4.9:*** *Incremental sliding and rolling energy dissipation inside each crown volume*
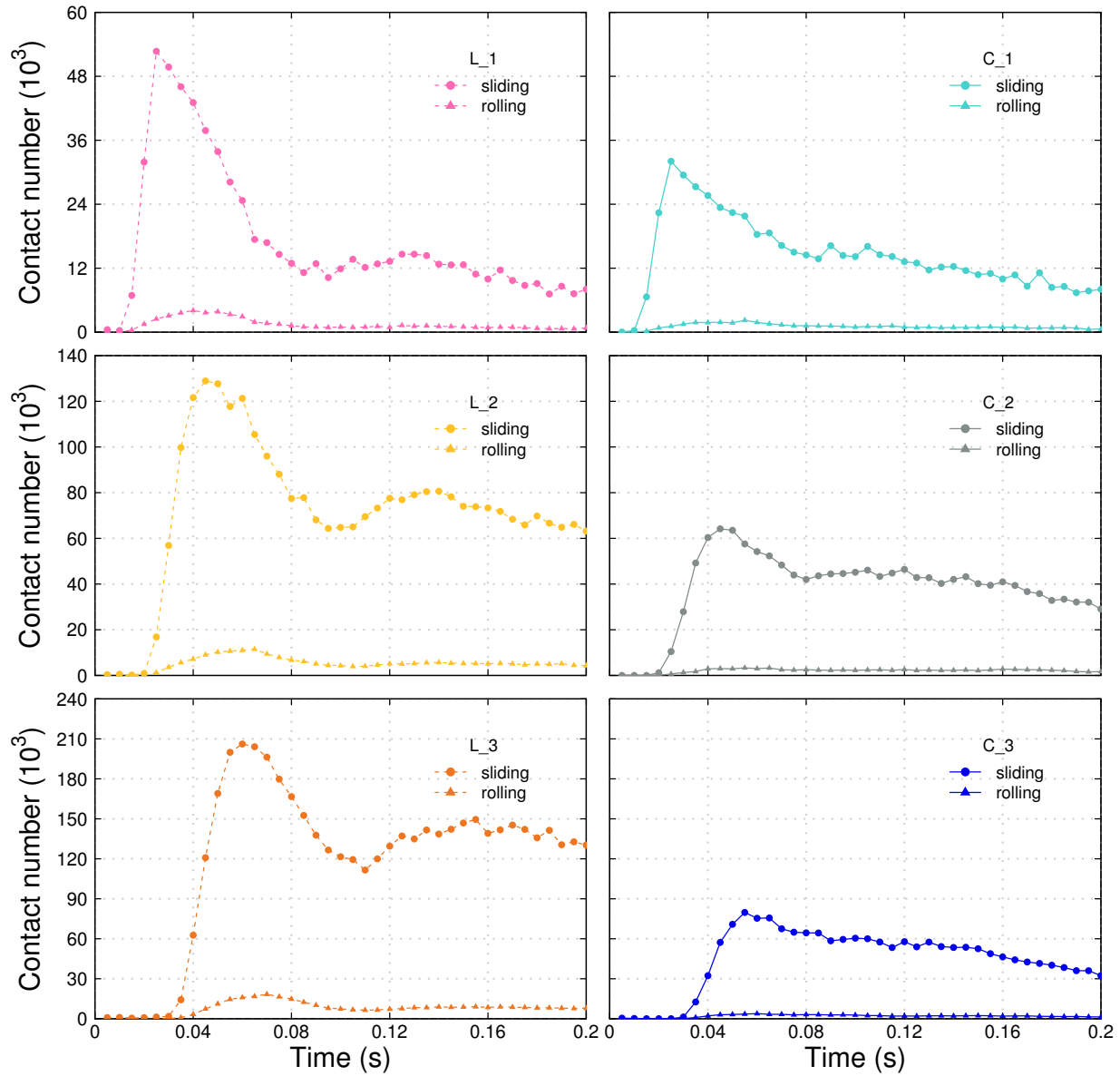
***Figure 4.10:*** *Number of sliding and rolling contacts inside each crown volume*

### 4.3.5 Discussion

The evolution of energies and coordination number offers information upon the physical response of the medium during boulder-medium interaction. The time delay of the increase in energies as well as the reduction of peak values from one crown to the adjacent one indicate that the propagation of energies is relevant with the propagation of compression waves. Moreover, the reflection of waves from the bottom boundary is revealed by the second energy peaks.

Among elastic strain energy $E_s$, kinetic energy $E_k$ and energy dissipation $E_d$, $E_s$ is related to the strength of the granular medium developed to resist the impact loading. Similar to the evaluation of impact force on the boulder, the increase in elastic strain energy inside each volume shows a peak (Figure 4.7). This indicates that the strength developed by the medium to resist against the impact of the boulder is not persistent. In addition, the increase of $E_s$ is accompanied with the increase in $E_k$ and $E_d$, the decrease in coordination number (Figure 4.11), which points out the strong rearrangements of the particles as well as the strength decrease of the granular medium. More specifically:
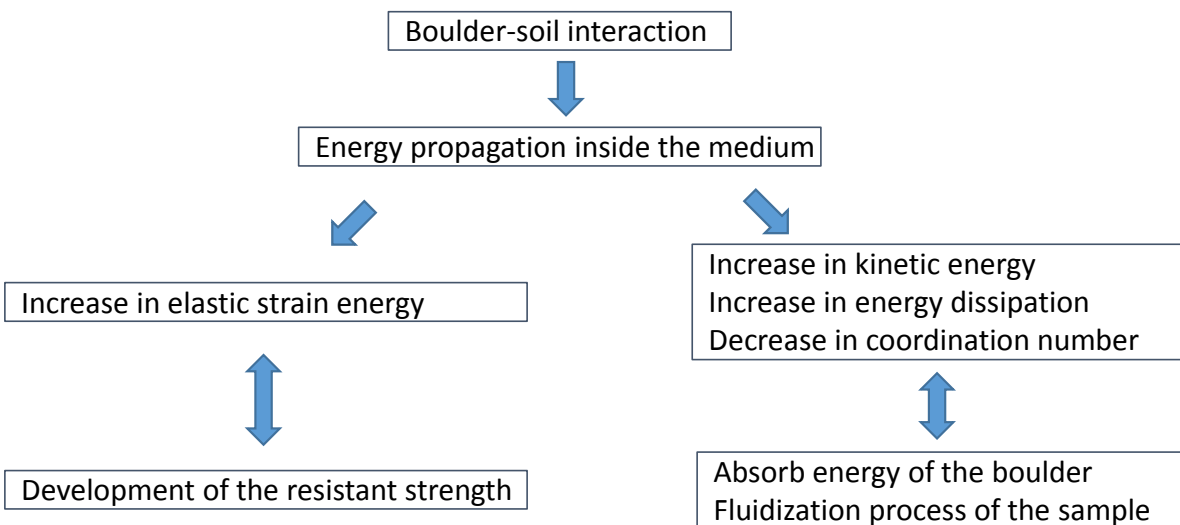


*Figure 4.11:* *Schema of energy propagation process inside the impacted medium*

- The peak value of $E_k$ is reached simultaneously or slightly later than that of $E_s$. The propagation of compression waves composes not only a compression phase (characterized by the increase of $E_s$), but also recovery phase (characterized by the increase of $E_k$). In addition, the correlation of $E_k$ and $E_s$ indicates the larger the initial value of $E_s$, the smaller the maximum $E_k$ increments.

- Comparison between energy dissipation by sliding and by rolling reveals that sliding motion is more dominating than rolling in this impact case, particularly, the number of sliding contacts is much larger than that of rolling contacts. The results are in contradiction with the results of Oda et al. (1982), Bardet (1994) and Shodja and Nezami (2003), in which they found that rolling motions are more dominating than sliding. This is because they used low rolling frictional oval particles, while in this simulation, rolling resistance is adopted to model the particle shape effects. This is consistent with the fact that rolling resistance has effects in resisting the rolling motion between the particles and inducing a much less number of rolling contacts. One thing to keep in mind is that even sliding motion is more dominating, energy dissipation by rolling is not negligible in this impact case. Moreover, energy dissipation per contact by rolling is much larger than that by sliding.

- The decrease in coordination number is relevant with the fluidization of the granular medium during the impact (de Bruyn and Walsh, 2004; Bourrier et al., 2008). After being subjected to the impact, the volume becomes very loose, especially for the volume of crown_1 and crown_2.

- Central volumes are the most influenced ones by having relatively higher magnitudes of $E_s$, indicating that they contribute to the main strength to the impact of the boulder. Lateral volumes characterized by relatively higher magnitudes of $E_k$ and $E_d$ indicate that they mainly play the role of absorbing boulder's kinetic energy. This is also consistent with the bimodal character of granular medium: a load bearing strong network and a energy dissipation weak network Radjaï et al. (1998). The energy dissipation in lateral volumes is due to the dissipation of weak networks, and the dissipation in central volumes is mainly due to the buckling of strong force networks.

The reaction of boulder is strongly related to the response of the impacted granular medium. Boulder rebounds if the medium is able to develop strong strength (characterized by large value of $E_s$) during the impact. Otherwise, the medium mainly plays the role of transforming boulder's kinetic energy into $E_k$ and $E_d$.

## 4.4   Boulder's global bouncing occurrence

This section aims at investigating the bouncing occurrence of boulder based on the developed 3D numerical impact model, with the consideration of particle shape effects. Impact conditions of various boulder sizes and medium thickness are considered. In addition, bouncing occurrence of boulder in 2D impact cases are also conducted to be qualitatively compared with 3D cases.

For this aim, a local bouncing criterion is defined that the impact force acting on the boulder is less than a proportion of boulder weight. Two criteria parameters are used to define a local bouncing occurrence and a global bouncing occurrence respectively. Parametric studies are conducted to see the effects of criterion parameters on the bouncing occurrences of boulders. Four specific impact cases are analysed to understand mechanisms that govern the bouncing of the boulder. Combined with the physical energy propagation process inside the medium, the bouncing of boulder on the granular medium is discussed.

### 4.4.1   Impact simulations

Series of simulations are conducted to investigate the bouncing occurrences of boulder under various impact conditions. The varying parameters are the radius of the boulder $R_b$ and the thickness of the impacted granular medium $H$. Samples of various layer thickness $H$ are generated for this purpose. $R_m$ of each impacted sample is 0.2 m, the length and width of the impacted sample in all cases are 20 m. The boulders impact the granular mediums vertically without rotational velocities, the initial impacting velocities are 20 m/s, thus the initial kinetic energy of boulder is cubic of the boulder radius.

Both 2D and 3D simulations are conducted. The 2D simulations using spherical particles and using the same contact parameters calibrated based on quai-static triaxial tests, with the consideration of rolling resistance. In 2D impact simulations, the center of boulder and particles are aligned in the "$y = 0$" plane. In order to avoid particles going out of "$xz$" plane, the freedom "$yXZ$" of particles are fixed, where "$y$" represents the translational movement in the "$y$" direction, "$X$" and "$Z$" represent the rotational movements around "$X$" and "$Z$" axis respectively. The boulders impacted on 2D samples are the same as the ones impacted on 3D samples.

In this study, in order to avoid local configuration effects induced by the discrete nature of granular materials, and to obtain representative bouncing actions (a boulder might bounce corresponding to one impact location and not on the other location), simulation corresponding to various impact locations are conducted.

For each pair of $(R_b, H)$ impact conditions, simulations corresponding to different impact points are conducted to get the average reaction of boulder. In 3D cases, 49 points are uniformly distributed in the center surface 2 m $\times$ 2 m of the "$xy$" plane. In 2D cases, 7 points are considered and are uniformly located in the center part of the sample (2 m) to avoid boundary effects. The number of simulations in 2D and 3D cases is assumed to be sufficient to get representative average results. Moreover, each impact simulation is run as long as 3 s to obtain the final settle of the boulder and the granular medium. A large domain of $(R_b, H)$ is considered: the boulder radius $R_b = nR_m$, with $n = 1, 2, ...,$ 11; the layer thickness $H = mR_m$, with $m = 10, 15, 20, ..., 50$ (to be more convenient, both $R_b$ and $H$ are represent by the average radius of particles $R_m$).

## 4.4.2  Definition of bouncing

### 4.4.2.1  Definition of a local bouncing

A local bouncing is a bouncing occurrence corresponding to a specific impact location. Various local bouncing occurrence criteria can be adopted, such as the impact force on the boulder equals to zero value or the change in the impacting particle's normal velocity sign after the interaction with the medium. The shortcoming of the former criterion is that impact force on the boulder is not vanishing in some cases by contacting with flying particles. Based on the later criterion, boulder always rebounds, due to the fact that without damping, the normal velocity of the boulder always fluctuates around the zero value before the boulder finally stops (if the simulation is run until the final settle of the boulder and the medium).

The local bouncing criterion adopted in this work is that the minimum impact force acting on the boulder inside series of time windows $\widehat{F}$ is less than a fraction value $\alpha_{cri}$ ($\alpha_{cri} \ll 1$) of the boulder weight $W_{boul}$. Bouncing is defined as:

$$\widehat{F} \leq \alpha_{cri} \, W_{boul} \tag{4.3}$$

Therefore, it is possible for the case of boulder contacting with few flying particles to be considered as bouncing, and the case of a tinny positive boulder velocity due to the fluctuations to be not considered as a bouncing.

The initial time window starts from the time $t'$, where $t'$ corresponds to the time when the velocity of the boulder first become positive. Starting from $t'$, successive time windows are taken to calculate the average impact force on the boulder $\overline{F_i}$:

$$\begin{cases} t_w = n \, t_c \\[2mm] \overline{F_i} = \dfrac{1}{t_w} \int_{t'+(i-1)t_w}^{t'+it_w} F_{boul}(t)dt, \qquad i = 1, 2, ... \\[2mm] \widehat{F} = \min\left(\overline{F_1}, \overline{F_2}, ..., \overline{F_i}, ...\right) \end{cases} \tag{4.4}$$

where $t_w$ is the length of the time window; $t_c$ is the contact duration of a grain impacting a fixed boulder; $n$ is a parameter.
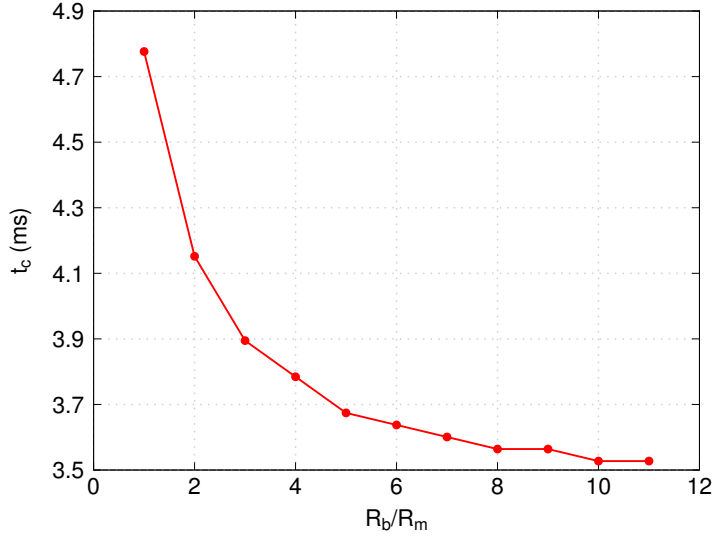
**Figure 4.12:** *Evolution of collision time versus the ratio of $R_b/R_m$*

Simulations are conducted to allow a particle (radius $R_m = 0.2$ m) to impact a fixed boulder (radius $R_b = [R_m, 11R_m]$) under gravity with an initial velocity (the collision time is independent of grain impacting velocity). Figure 4.12 shows that generally the contact duration is among [3.5 ms, 4.7 ms]. In this work, $t_w = 0.05$ s, which is approximately 10 times of the grain-boulder collision time.

Figure 4.13 shows the time evolution of impact force $F_{boul}$, boulder velocity $V_{boul}$ and boulder penetration depth $Z_{boul}$ for a specific impact case of $R_b = 5R_m$, $H = 15R_m$. Two impacts corresponding to the time period of [0 s, 0.1 s] and [0.45 s, 0.71 s] are observed. The first impact induces significant reverse of $V_{boul}$, correspondingly, $Z_{boul}$ goes up to 0.1 m during the time period of 0.1 s to 0.2 s (Figure 4.13(c)). The second impact only induces $V_{boul}$ slightly reverses. The zoom of $F_{boul}$ in figure 4.13(b) shows that $F_{boul}$ is generally less than $\alpha_{cri}W_{boul}$ between the two impacts, except during the period of [0.28 s, 0.36 s] in which the boulder is contacting with flying particles. In addition, it is worth noting that $V_{boul}$ has a tiny positive value (0.018 m/s) around the time of 0.7 s, while $F_{boul}$ is much larger than the critical value $\alpha_{cri}W_{boul}$, the boulder is considered staying in contact with the granular medium. The bouncing of boulder in this impact case is verified based on $F_{boul}$ between the first and the second impacts.
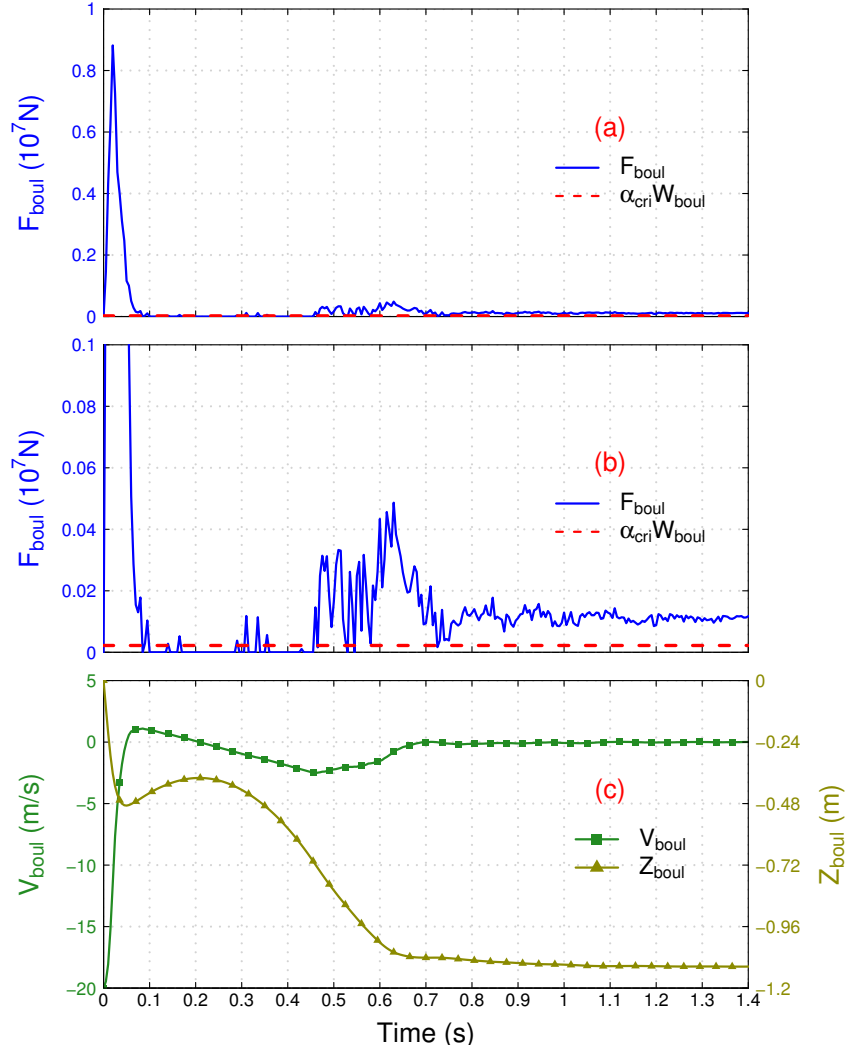
**Figure 4.13:** *Time evolution of (a) impact force $F_{boul}$, (b) zoom of $F_{boul}$, (c) velocity $V_{boul}$ and penetration depth $Z_{boul}$ for the case of $R_b = 5R_m$, $H = 15R_m$*

### 4.4.2.2 Definition of a global bouncing

Since 7 simulations and 49 simulations are considered in 2D and 3D cases respectively for each $(R_b, H)$ impact case, a global bouncing occurrence for varying impact points and fixed incident conditions is defined as:

$$\frac{n}{N} \geq P_{cri} \tag{4.5}$$

where N is the total number of simulations; n is the number of local bouncing occurrences events, $n \leq N$.

Therefore, two parameters $\alpha_{cri}$ and $P_{cri}$ are adopted for the definition of a bouncing. $\alpha_{cri}$ is the proportion of impact force acting on the boulder to the boulder weight, which defines a local bouncing; $P_{cri}$ is the proportion of local bouncing compared to the total number of impact locations, which defines a global bouncing.

### 4.4.3  Bouncing occurrence diagrams
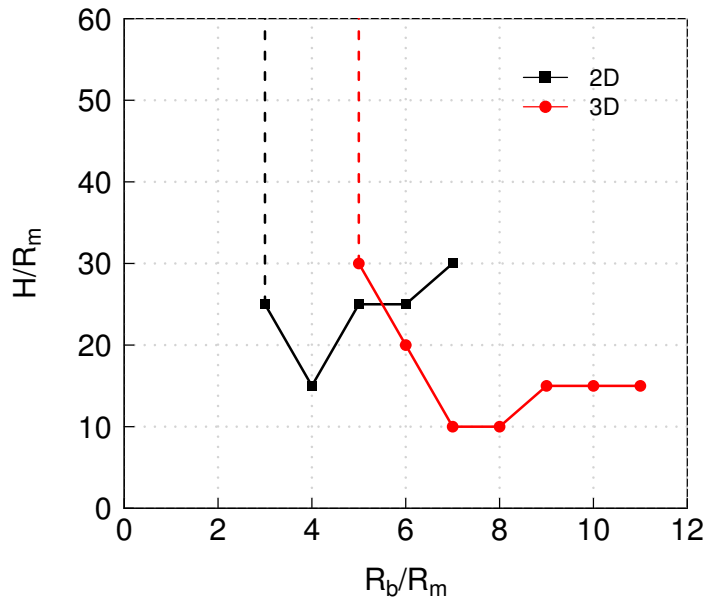


***Figure 4.14:*** *Bouncing occurrence diagrams for both 2D and 3D cases by adopting two criterion parameters $\alpha_{cri} = 0.2$ and $P_{cri} = 0.6$*

Figure 4.14 demonstrates the bouncing of boulder corresponding to the case of $\alpha_{cri} = 0.2$ and $P_{cri} = 0.6$. Results obtained in 2D and 3D cases are plot together for qualitative comparison purpose. The curves distinguish the $(R_b, H)$ plane into a rebound domain and a non-rebound domain: the space below the curve corresponds to the re-

bound domain, and the space above the curve corresponds to non-rebound domain. The solid lines themselves belong to rebound domain, and the dotted lines themselves belong to non-rebound domain.

Generally, similarities and differences exist between bouncing of boulder in 2D and 3D cases:

- For both 2D and 3D cases: if the impacting boulder is sufficiently small, boulder rebounds whatever the thickness of the sample; if the layer thickness is sufficiently shallow, bouncing occurs whatever the size of the boulder. In addition, three impact regime exists. The first regime corresponds to a small impacting boulder, in which the boulder rebounds for any sample height. The second impact regime corresponds to a medium size boulder, in which the boulder does not bounce for all cases, the bouncing domain shows a decrease trend as $R_b$ increases. The third impact regime corresponds to a big size boulder, in which the bouncing shows an increase trend as $R_b$ increases. The results are generally consistent with the results of Bourrier et al. (2008).

- The domains of bouncing regimes are different between 2D and 3D cases. For 2D case, the domain for the three regimes is $R_b < 3R_m$, $3R_m \leq R_b \leq 4R_m$, $R_b > 4R_m$ respectively; For the 3D case, the domain for the three regimes is $R_b < 5R_m$, $5R_m \leq R_b \leq 7R_m$, $R_b > 7R_m$ respectively. Compared to the 3D case, the domain of the first regime is smaller and the domain of the second regime is more limited in 2D case. The bouncing domain of the third regime shows a much steeper increase trend in 2D case.

In addition, figure 4.15 shows the bouncing occurrence of boulder for various of $\alpha_{cri}$ and $P_{cri}$, the range of $\alpha_{cri}$ is $[0, 0.2]$, the range of $P_{cri}$ is $[0.5, 0.8]$. The results indicate that for both 2D and 3D cases, the larger the value of $\alpha_{cri}$, the larger the bouncing domain; the larger the value of $P_{cri}$, the smaller the bouncing domain (Figure 4.15 ). The influence of using different parameters in 2D cases is less important than 3D cases. In 2D cases, the third regime is mostly influenced by varying parameters, while the domains of the first and second regimes are independent of the varying parameters. In 3D cases, all of the three regimes are influenced by the parameters. Generally 2D cases have larger bouncing domains.
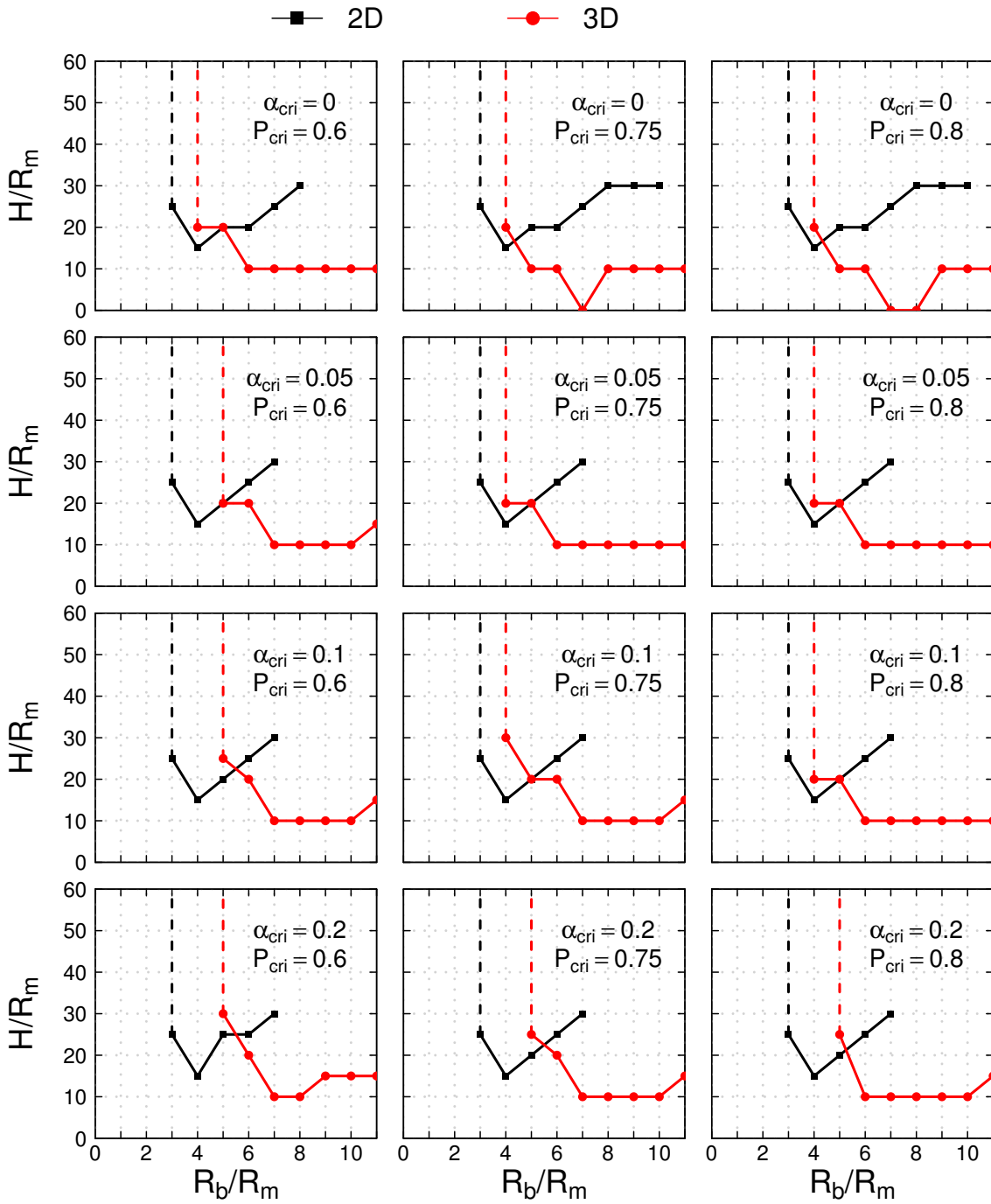
***Figure 4.15:*** *Bouncing occurrence diagrams for both 2D and 3D cases by adopting various pair of criterion parameters ($\alpha_{cri}$, $P_{cri}$)*

Investigations are conducted to understand the impact mechanisms based on the reaction of boulder (impact force, velocity) corresponding to three impact regimes. Particularly, due to momentum conservation law, $F_{boul}\Delta t = M_b \Delta V_{boul}$, the variation of boulder's velocity $\Delta V_{boul}$ depends on the impact force on the boulder $F_{boul}$ and the contact duration, as well as the mass of the boulder $M_b$. Four specific impact cases are considered ( figure 4.16). The reaction of boulder corresponding to the four cases are shown in figure 4.17.
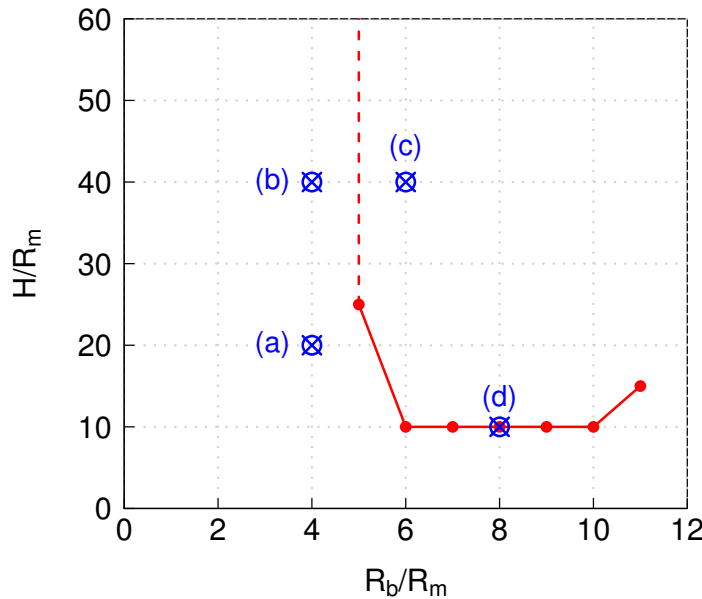


**Figure 4.16:** *Bouncing occurrence diagrams for both 2D and 3D cases by adopting two criterion parameters $\alpha_{cri} = 0.2$ and $P_{cri} = 0.8$*

The bouncing of boulder shown in figure 4.17(a) and 4.17(b) corresponds to the first impact regime, in which the bouncing of boulders is due to the first impact between the boulder and the granular medium. In addition, layer of thinner thickness results in a higher impact force on the boulder and makes the boulder to have a larger bouncing velocity. Particularly, the maximum impact force on the boulder in cases of (a) and (b) is $0.73 \times 10^7$ N, $0.51 \times 10^7$ N respectively, the maximum velocity of boulder after the first impact is 2.54 m/s, 0.67 m/s respectively.
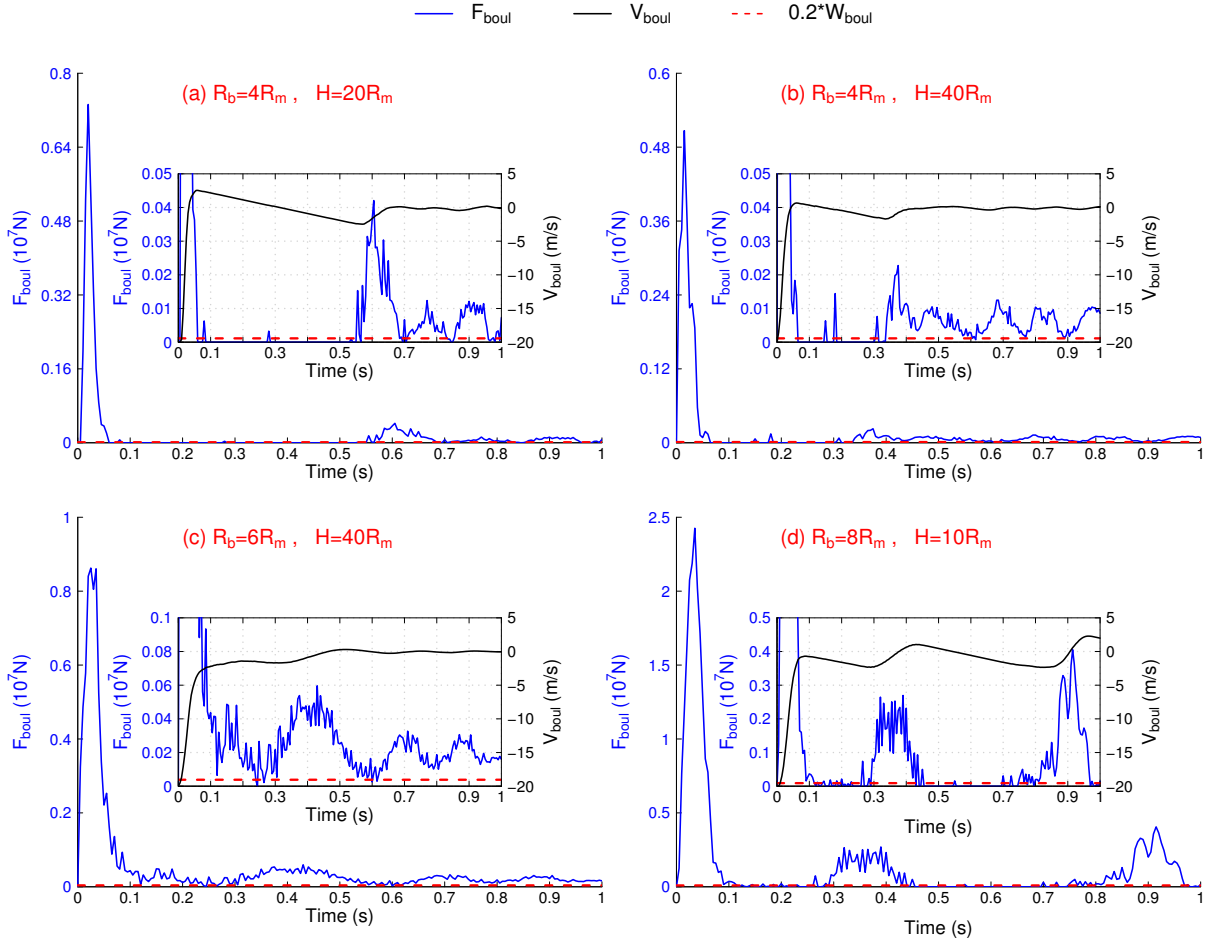
**Figure 4.17:** *Reaction of impact force on the boulder $F_{boul}$, velocity of boulder $V_{boul}$ for the case of (a) $R_b = 4R_m$, $H = 20R_m$; (b) $R_b = 4R_m$, $H = 40R_m$; (c) $R_b = 6R_m$, $H = 40R_m$; (d) $R_b = 8R_m$, $H = 10R_m$*

Figure 4.17(c) is a non-bouncing event corresponding to the second regime. The first impact makes the velocity of boulder decrease without inversion. During the successive interactions, the impact force on the boulder is always larger than the critical value $\alpha_{cri}W_{boul}$, which indicates that the boulder keeps contacting with the whole granular medium. The velocity fluctuates around the zero value until the boulder finally stops.

Figure 4.17(d) corresponds to a bouncing event of the third regime. Similar as shown in figure 4.17 (c), the velocity of boulder decreases after the first impact, while the difference is that there occurs a second impact which makes the boulder bouncing (The impact force on the boulder is much smaller than its gravity weight after the second impact

which indicates that the boulder loses the contacts with the medium. On the whole, three impacts are observed in figure 4.17(d).). In fact, the case of second impact makes boulder rebound occurrence corresponding to a big boulder impacting with large incident energy. Boulder transfers large amount of energy to the medium while the medium only has limited energy dissipation capacities, the residual energies transferred from the medium back to the boulder make boulder to rebound.

In addition, it is worth mentioning that during the second impacts of cases shown in figure 4.17(a-d), at the time of 0.55 s, 0.33 s, 0.3 s, 0.3 s respectively, the layer thickness below the boulder are $18R_m$, $37.3R_m$, $34R_m$, $4.5R_m$ respectively (data not shown). It seems that the bouncing of boulder during the second impact shown in figure 4.17(d) is related to a thin layer thickness between the boulder and the bottom boundary. The large strength of the medium with a thin layer thickness might be related to the strong force chains developed inside the medium. Moreover, the energy of boulder shown in figure 4.17(d) is not totally absorbed by the granular medium at the time of 1 s. On the contrary, at that time the kinetic energies of boulders shown in figure 4.17(a-c) almost have been totally transferred to the medium, the velocities are all around 0 values. It confirms that the stabilization of the boulder-medium interaction process is dependent of input energy and energy dissipations.

### 4.4.4   Discussion

The results of 4 impact cases (Figure 4.17) reveal that the bouncing of the boulder is induced either by the first impact or by the successive impacts (Figure 4.18). Based on the results obtained in the former section which indicate that strength (revealed by the elastic strain energy, impact force, or the velocity of boulder after impact) and dissipation capacities (revealed by the increase of kinetic energy and energy dissipation) are two issues that influence the reaction of the boulder, it seems that if the medium has strong strength to the impact of boulder during the first impact, the boulder directly rebounds. If the boulder does not rebound after the first impact, the boulder stays in contact with the medium. The bouncing of boulder depends on the subsequent interactions between the boulder and the medium as well as the energy dissipation inside the medium.
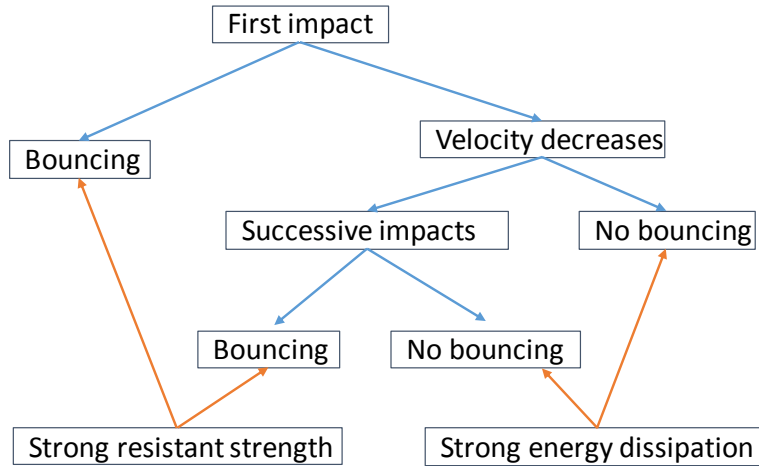
***Figure 4.18:*** *Schema of the bouncing occurrence of boulders*

Moreover, the reaction of boulder is dependent of boundary conditions (layer thickness). On one hand, thinner layer can develop stronger strength during the first impact. For instance, the peak value of impact force obtained by impacting a medium of $20R_m$ thickness is 43% larger than impacting a medium of $40R_m$ thickness (Figure 4.17(a-b)). On the other hand, it is reasonable to suppose that thicker layers have higher energy dissipation capacities due to more number of grains and more number of contacts. The strength and the energy dissipation capacity of the medium are related to each other. Therefore, thinner mediums are characterized with the stronger strength resistance and the smaller energy dissipation capacity makes boulder easier to rebound after the impact. This is consistent with the fact that boulder always rebounds on a shallow medium thickness as illustrated by the bouncing occurrence diagrams.

The shape of bouncing diagram curves may be interpreted from the medium strength and energy dissipation points of view. The first regime corresponds to small boulders with small initial input energy, even thick medium is able to build strong enough strength to resist the impacts of these boulders, bouncing occurs for every layer thickness. The bouncing domain of the second regime shows a decrease trend because thinner layers are required to maintain stronger resistance to the penetration of boulder under moderate input energy impact. The bouncing domain of the third regime shows an increase trend because under big input energy impact, the strength developed by the medium during the first impact is not sufficient to make the boulder rebound and the bouncing of boulder relies on successive impacts, which allows bouncing to occur on a thicker layer thickness

(or layers characterized by larger amount of energy dissipation capacities). Therefore, the bouncing/non-bouncing of boulder on a granular medium is a competition between the boulder incident energy (represented by the boulder size) and strength together with energy dissipation capacities of the medium (represented by the medium thickness). In fact, the bouncing of boulder is related to the relatively high strength as well as low energy dissipation capacities of the medium

In addition, the difference between the bouncing diagram curves in 2D and 3D cases may be interpreted similarly. Under the impact conditions of same boulder and same local contact parameters, strength and energy dissipation capacity of the medium in 2D case are much smaller than 3D case, due to its limited number of particles and to the strong kinematical constraint in the cross direction. Therefore, the bouncing domain of first regime induced by the first impact is smaller in 2D case compared to 3D case, the bouncing domain of the third regime mainly due to the second impact is bigger in 2D case than 3D case. One thing to keep in mind is that the comparison between 2D and 3D cases are just qualitatively comparisons. The 2D impact simulations are not calibrated with experiments and adopt the same contact parameters as well as grain size distributions as the 3D cases. The 2D simulations calibrated with experiments might give quantitatively different bouncing occurrence diagrams.

## 4.5   Conclusion

This chapter investigates the bouncing occurrence of boulder on a granular medium with the consideration of local configuration effects and the physical energy propagation process inside the medium. The results indicated that the strength of the sample developed to resist the impact of boulder and energy dissipation properties are important points that significantly influence the reaction of the boulder. More specifically:

First of all, local configurations are shown to have influences on the impact force and reflect velocity of the boulder. For the impact case of $R_b = R_m$, statistical test suggests that 49 simulations of fixed incident conditions and varying impact locations compromise best between the representative average results and the computational cost. Afterwards, 49 simulations are adopted for impact cases of $R_b > R_m$. In addition, the variability of results decreases with the increase of $R_b/R_m$.

Second, the energy propagation process inside the impacted zone investigated from crown to crown indicates that the energy propagation is associated with the propagation of compression waves. The strength of the sample under impact is represented by the increase of elastic strain energy due to the overlapping between contacting particles. The increase of elastic strain energy is followed by a fluidization process in which the particles have strong rearrangements characterized by the increase in kinetic energy and energy dissipation, as well as the decrease in coordination number. In addition, energy dissipation by sliding is much more important than that by rolling, due to the implementation of rolling resistance.

Third, the bouncing of boulder follows three bouncing regimes with respect to boulder sizes. Investigation of four specific impact cases corresponding to three regimes indicates that the bouncing of boulder is induced either by first impact or subsequent impacts. If the granular medium gives enough strength against the first impact, boulder rebounds directly. Otherwise, the bouncing of boulder during the successive impacts depends on the strength of medium as well as the energy dissipation capacities. This interpretation explains the shifts of regime curves between 2D and 3D impact cases.

The global bouncing reactions of boulder and the response of the impacted granular medium are mainly interpreted in this chapter from an energy propagation and kinematic points of view. However, interpretations of load transfer mechanisms from a micromechanical point of view is still required, since, undoubtedly, all macro responses of the granular medium have deep fundamental micro-mechanical reasons. The next chapter will focus on investigating the force chain related load transfer micromechanics inside the impacted medium. Unlike in this chapter where 49 simulations are considered to quantify the bouncing, most of the investigations in the next chapter (except section 5.3.1 and 5.3.2) do not consider the effects of local configurations. We suppose that investigation corresponding to one specific impact location is sufficient to point out the main micromechanisms that govern the boulder-medium interaction.

# Chapter 5

# Micromechanical behaviour of the impacted medium

## Contents

## 5.1 Introduction

This chapter investigates the boulder-medium interaction from a micromechanical point of view. The aim is to investigate how the microstructure evolves and adapts itself when impacted. In particular, it will be shown that force chain plays a major role.

First of all, force chain networks inside an impacted medium are characterized based on particle stress informations. The properties of chains (the number of chain particles, the average chain length) are examined. Second, the effects of grain sizes are investigated. Simulations of identical boulders impacting medium of different grain sizes are conducted, relations between the impact force on the boulder and force chain properties (average chain length, chain age) are investigated. Third, the load transfer mechanisms inside the impacted medium are quantified through the spatial and temporal evolution of force chains. The spatial force chain structures are characterized based on the regimes proposed by Clark et al. (2014). Finally, force chain buckling mechanisms are studied to find the correlation of the number of buckled force chains with impact force, kinetic energy as well as energy dissipation inside the impacted medium. Finally, the potential of force chain micromechanisms for rockfall trajectory analysis and protection structural design is discussed.

## 5.2 Characterization of force chains inside an impacted medium

The commonly used numerical force chain identification methods are based on particle contact informations. Initially, force chains are characterized simply by following the path of maximum contact force at each particle (Radjaï et al., 1998; Makse et al., 2000; Bourrier et al., 2008; Kondic et al., 2012), in which the contact force between particles is plotted with a line thickness proportional to the magnitude of the contact force. However, this can result in highly nonlinear force chains, and it is difficulty to characterize the chain orientations. Comparatively, force chain identification method based on particle stress tensor seems to be a better approach (Peters et al., 2005; Tordesillas et al., 2009, 2014). This method takes particle contact informations as inputs and gives force chain networks as outputs, using particle principal stress to characterize both the orientation and magnitude of force chains. In addition, very recently, Tordesillas et al. (2015) pre-

dicted the majority of force chain particles (76-82%) observed in experiments without need for any information on contact forces. The force chain network was predicted through a subnetwork of contacts that transmits the "maximum flow" (i.e., the highest units of force) at "least cost" (i.e., the dissipated energy from such transmission).

## 5.2.1   Major principal stress $\sigma_1$ of a particle

This work adopts the force chain identification method based on particle stress tensor. The stress tensor of a particle $\sigma$ is calculated as:

$$\sigma = \frac{1}{V} \sum_{c=1}^{N^c} f_i^c l_j^c = \begin{vmatrix} \sigma_x & \tau_{xy} & \tau_{xz} \\ \tau_{xy} & \sigma_y & \tau_{yz} \\ \tau_{xz} & \tau_{yz} & \sigma_z \end{vmatrix} \tag{5.1}$$

where $V$ is the volume of the particle, $N^c$ is the number of neighbouring particles in contact with this particle, $f_i^c$ is the $i^{th}$ component of the force $f^c$ acting on the particle, $l_j^c$ is the $j^{th}$ component of the vector $l^c$ denoting from the center of the contacting neighbour to the center of the particle.

The principal stresses $\sigma_1$, $\sigma_2$, $\sigma_3$ are obtained based on the eigenvalues and eigenvectors of the matrix illustrated in equation (5.1). Only the principal stress characterized by the maximum stress magnitude is chosen to decide whether a particle is a chain particle or not, the major principal stress $\sigma_1$ has the maximum stress magnitude and thus is the one considered .

The major principal stress of each particle is characterized by a magnitude value $\sigma_1$ and two orientation parameters $\theta$ and $\varphi$, where $\sigma_1$ is the magnitude of the major principal stress; $\theta$ is the angle between $\sigma_1$ and the $z$ axis, $\varphi$ is the angle between $\sigma_1$ and the $x$ axis (Figure 5.1). By definition, the range of $\theta$ and $\varphi$ are both within $[0°, 180°]$.
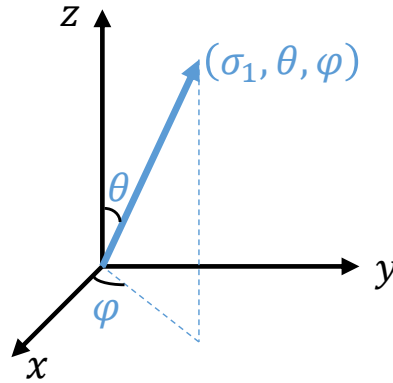
**Figure 5.1:** *The major principal stress of a particle*

## 5.2.2 Algorithms for selecting force chain particles

The algorithm for a particle to be in a force chain consists checking whether it undergoes larger stress compared to the average stress value of all the particles. The algorithm is:

$$\sigma_1^j > \overline{\sigma_1} = \frac{1}{n} \sum_{i=1}^{n} \sigma_1^i \tag{5.2}$$

where $\sigma_1^j$ is the magnitude of the major principal stress of the $j^{th}$ particle, $n$ is the total number of particles, $\overline{\sigma_1}$ is the average magnitude of the major principal stress of all particles.
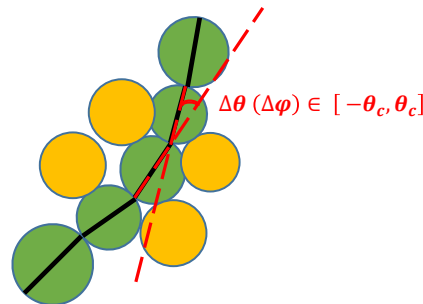


**Figure 5.2:** *Intersection angle of chain particles*

The force chains are quasilinear with minimum three chain particles, therefore, the orientations of major principal stresses of two adjacent chain particles belonging to the same chain should fulfill:

$$\Delta\theta \in [-\theta_c, \theta_c] \qquad \text{and} \qquad \Delta\varphi \in [-\theta_c, \theta_c] \qquad (5.3)$$

where $\Delta\theta$ and $\Delta\varphi$ are the interaction angles of the orientation of the major principal stresses between two adjacent chain particle (Figure 5.2). $\theta_c = 0°$ implies perfectly linear force chains. Considering the discrete properties of granular materials, $\theta_c$ is selected to allow force chains to have a reasonable degree of "curvature". $\theta_c$ in this study adopts the value of $45°$, a common value used in the literature (Peters et al., 2005; Tordesillas et al., 2009, 2014).

### 5.2.3   Procedures for identifying force chain network

The procedure for identifying the force chain network is described as:

1. Calculate $\sigma_1$ of each particle.

2. Filter out particles whose $\sigma_1$ are smaller than the average value $\overline{\sigma_1}$. The particles whose $\sigma_1$ are larger than the average value $\overline{\sigma_1}$ are called strongly-stressed particles.

3. Filter out particles having less than two contacts. Since a force chain is defined as having minimum three particles, therefore, for a particle to be in a chain, it must be a strongly-stressed particle contacting at least two strongly-stressed neighbours. Correspondingly, chain particle candidates are strongly-stressed particles having at least two strongly-stressed neighbours.

4. Randomly choose a chain particle candidate as the starting point, detect the successive chain particles within $[-\theta_c, +\theta_c]$ in the forward and backward direction following the procedure proposed by Peters et al. (2005). This is called a detection loop. In addition, the candidates for the next chain particle are examined starting from the one characterizing with the maximum value of $\sigma_1$, to make the force chains to extend preferably toward the most strongly-stressed direction.

5. Repeat the detection loop until all the force chains have been detected. Moreover, in order to avoid producing crossing chains, one particle belongs to only one chain (at the largest).

### 5.2.4 Average major principal stress $\overline{\sigma_1}$

In order to have an idea of force chain properties inside the impacted granular medium, the time evolution of the average major principal stress of all particles $\overline{\sigma_1}$, the number of chain particles (based on $\theta_c = 45°$) are investigated in this subsection. The investigations are conducted based on the 3D impact case of $R_b$=1.17 m, $H$= 3 m.
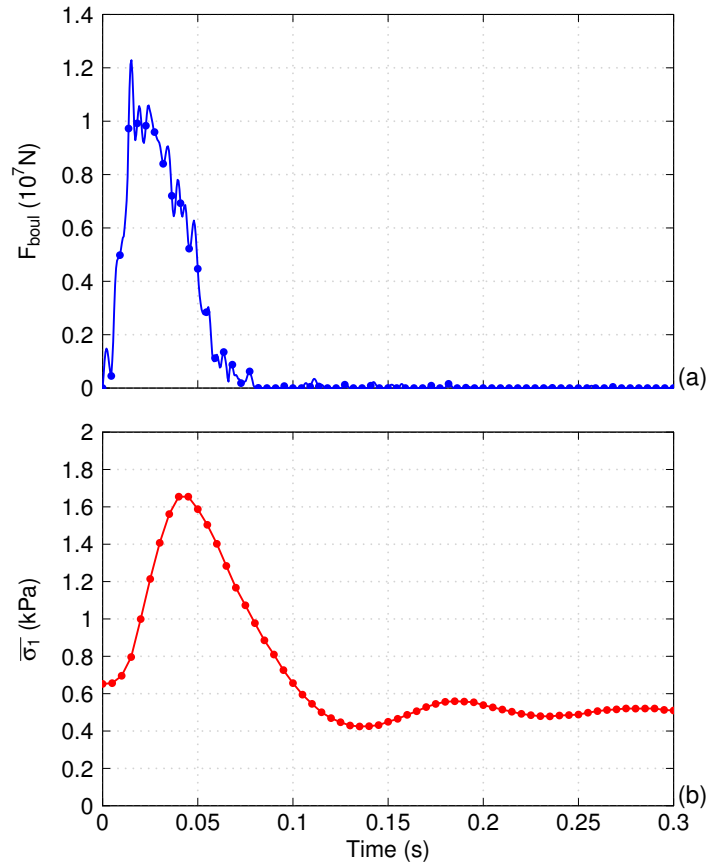


**Figure 5.3:** *Time evolution of (a) Impact force on the boulder and (b) Average major principal stress $\overline{\sigma_1}$ of all particles*

The time evolution of $\overline{\sigma_1}$ and impact force $F_{boul}$ are plotted together for comparison purpose (Figure 5.3). The figure indicates that initially, the value of $\overline{\sigma_1}$ is 0.65 kPa (due to gravity), impact induces the increase in $\overline{\sigma_1}$, high values of $\overline{\sigma_1}$ corresponds to high values of $F_{boul}$. In addition, the maximum magnitude of 1.65 kPa is reached at the time of 0.04 s, which is later the arriving time of the impact force peak $max.F_{boul}$. From the time of 0.1 s,

$\overline{\sigma_1}$ fluctuates around a value which is smaller than the initial value. One thing to keep in mind is that the critical value for chain particle identification $\overline{\sigma_1}$ varies with time. It is possible for a particle who has the same magnitude of $\sigma_1$ to be a chain particle candidate at one time and not at another time.

## 5.2.5   Number of chain particles and average chain length

The time evolution of chain particle populations (inside specific crown or the whole sample volume) and average chain length are investigated inside this subsection (Figure 5.5). The medium is divided into several crown volumes according to their distance from the impact point. Each crown has the same thickness, that is a quarter of the medium thickness (Figure 5.4). The volume between the boulder and Crown_1 is not considered due to its limited number of particles. The length of a chain is defined by the number of particles belonging to the chain. The average chain length $l_{chain}$ is defined as the population of chain particles divided by the number of chains.
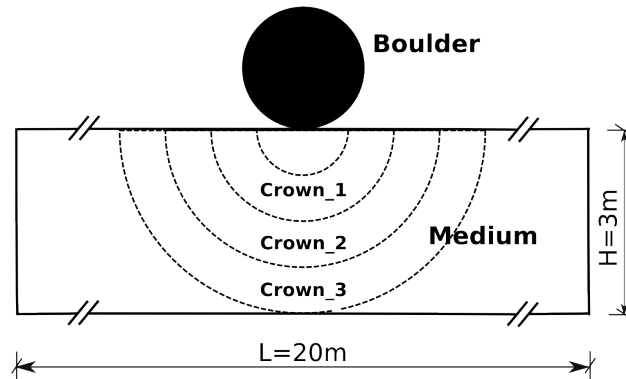


**Figure 5.4:**  *Crown volumes of the medium*

Figure 5.5(b) shows that initially, the total number of chain particles inside the three crowns are 170, which occupies of 7.7% of the total chain particles. Moreover, chain particles mainly locate inside the crown_3 layer (67% of the total chain particle population inside the three crown volumes). Impact introduces a significant decrease in chain particle populations inside the crown_3 volume, the minimum numbers of chain particles become 61% of the initial value. The decrease of chain particle number inside crown_2 is less significant compared to crown_3. The decrease in chain particle populations inside

crown_2 and crown_3 is due to the increase of $\overline{\sigma_1}$. On the contrary, impact induces the increase in chain particle number in crown_1 volume, the maximum value is 10.2 times of the initial value. The amount of chain particles inside each volume decrease after the corresponding peak values. The population of chain particles is negligible inside crown_1 and crown_2 after the time of 0.076 s, while the population of chain particles are non-vanishing inside crown_3 and shows a slight increase trend after the time of 0.076 s.

Figure 5.5(c) shows the time evolution of the number of chain particles for the whole sample. Initially, the population of chain particles is 13.6% of the total number of particles inside the sample (the total particle population is 17961). Impact induces a decrease of chain particle number, the minimum value is 43% of the initial value. The number of chain particles increases back to the value of 2442 at the time of 0.075 s, and varies slightly after the time of 0.15 s.

Figure 5.5(d) shows the time evolution of $l_{chain}$ inside the impacted medium: initially the average chain length is 4.58, impact induces the decrease of average chain length, a minimum value of 4.07 is reached at the time of 0.03 s. The minimum number of chain particles and the minimum average chain length are reached around 0.01 s earlier than the peak value of $\overline{\sigma_1}$, which indicates that the most compressed state of the medium is reached later than the time corresponding to the minimum number of chain particles. In addition, impact does not induce significant variation of average chain length (the variation is between the value of 4.0 and 4.7).

The variation of the number of chain particles and $l_{chain}$ indicates the micromechanical reorganization inside the impacted medium. The investigation in this section corresponds to a specific case, while in the next section, the effects of grain sizes on the impact force on the boulder, the chain length and the chain age will be investigated.
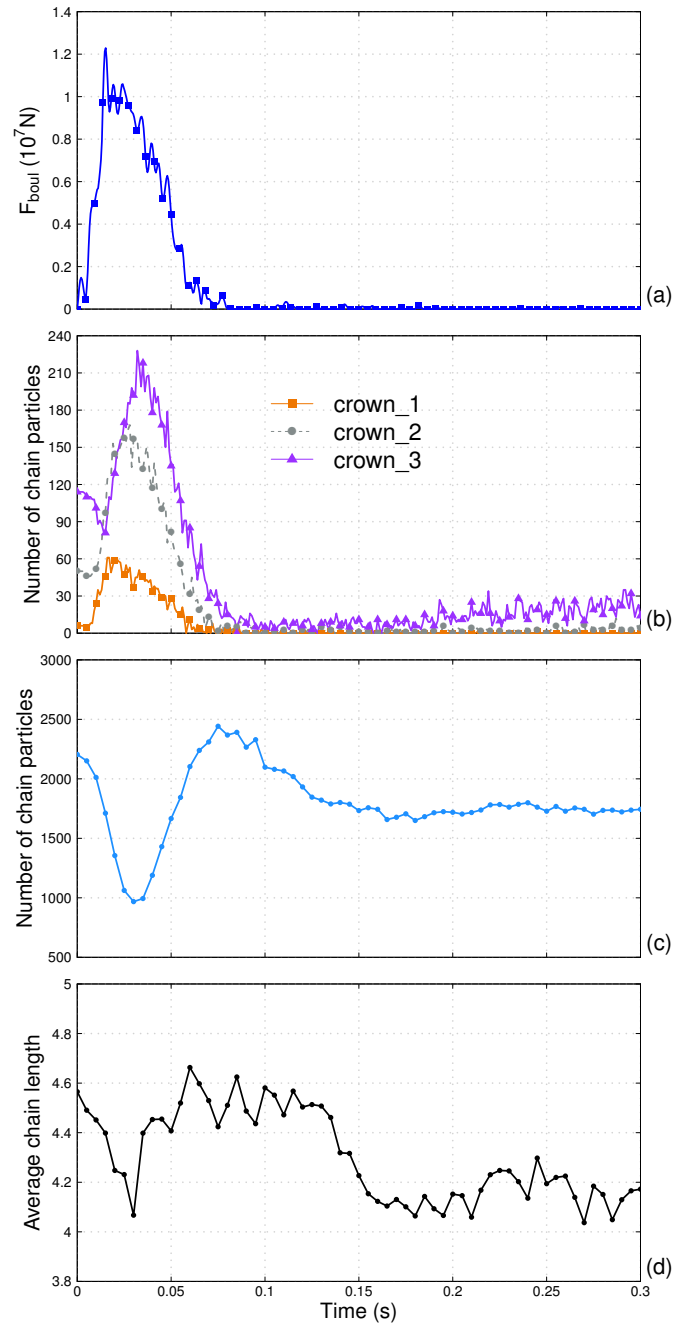
***Figure* 5.5:** *Time evolution of (a) Impact force on the boulder $F_{boul}$, (b) number of chain particles inside crown layers, (c) Number of chain particles for the whole sample, (d) Average chain length*

## 5.3   Parametric analysis of the effects of grain sizes

It has been shown in chapter 4 that the bouncing of boulder depends on the ratio of boulder size to grain size $R_b/R_m$, under conditions of a fixed grain size $R_m = 0.2$ m. This section investigates the influences of grain sizes $R_m$ on the boulder-medium interaction by fixing $R_b$ and varying $R_m$. The aim is to investigate the relations between the impact force on the boulder and the force chain properties (average chain length, chain age) of the medium depending on its grain size distribution. The effect of grain sizes on impact force is investigated based on 3D simulations. The effects of grain sizes on chain length and chain age are investigated based on 2D simulations for computational considerations, besides, the 2D simulations are supposed to give quantitative consistent results with 3D simulations.

### 5.3.1   Effect of grain sizes on impact force

Simulations of boulders impacting samples composed of various particle sizes are conducted (Figure 5.6). The boulders are all identical with a 1.0 m radius and 20 m/s initial impact velocity. The dimensions of the samples in all cases are 20 m in length and width, 5 m in thickness. The granular assembly inside each sample follows a uniform distribution, with a variation of 33% around the average particle size in the 0.1 m - 0.5 m range. For each impact case corresponding to a specific sample, 49 simulations corresponding to various impact locations are conducted (the impact points are located on the center surface of 2 m $\times$ 2 m, following the same methodology as proposed in chapter 4). The data shown in figure 5.7 correspond to the average impact force peak obtained based on 49 simulation results.

Figure 5.7 indicates that the smaller the size of the particles, the smaller the impact force peak on the boulder. For instance, corresponding to the case of $R_b/R_m$=2 ($R_m$ =0.5 m), the impact force peak is 1.26 $\times 10^7$ N; corresponding to the case of $R_b/R_m$=10 ($R_m$ =0.1 m), the impact force peak is 0.68 $\times 10^7$ N. In addition, as the size of particles become smaller, the decrease gradient of impact force peak tends to become smaller, the impact force peak tends to converge when the size of particles is sufficiently small.

(a)                                          (b)                                          (c)
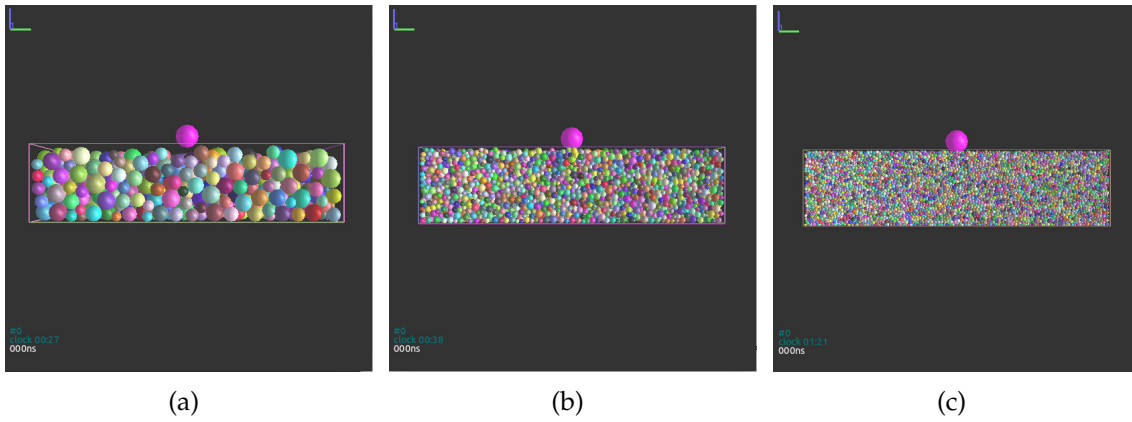
**Figure 5.6:** *Experiments set up for (a) $R_b/R_m = 2$, (b) $R_b/R_m = 5$, (c) $R_b/R_m = 10$*
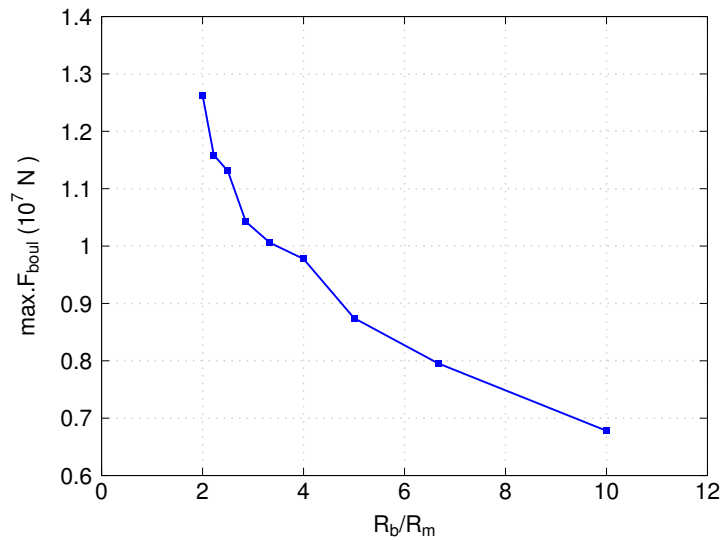


**Figure 5.7:** *The average maximum impact force on the boulder versus the $R_b/R_m$*

### 5.3.2   Effect of grain sizes on chain length

This subsection focuses on investigating the average chain length and chain age inside impacted mediums composed of various grain sizes. The aim is to find how they influence the impact force. Force chain investigations are conducted in 2D cases. The dimensions of all 2D samples are 20 m in lengths and 5 m in thickness. In addition, for each impact case corresponding to a specific sample, 7 simulations corresponding to 7 impact locations uniformly distributed in the center surface of 2 m are conducted. The

data plotted in figure 5.8 are obtained based on the average value of 7 simulations. Even though the results will be quantitatively differ from 2D to 3D, the results obtained based on 2D simulations are supposed to be qualitatively representative of the 3D results.

Figure 5.8 shows the evolution of $l_{chain}$ and $l_{chain}/N_p$ versus the ratio of $R_b/R_m$, where $l_{chain}$ is the average chain length, $N_p$ is the number of particles in the vertical direction of the sample, $N_p = H/d_m$ ($d_m$ is the average particle diameter). $l_{chain}$ is recorded based on the chains existing at the time corresponding to the impact force peak.

Figure 5.8(a) indicates that $l_{chain}$ increases with the increase of $R_b/R_m$. For small particle sizes of 0.05 m ($R_b/R_m$=20), $l_{chain}$ is 5.9, while for big particle sizes of 0.5 m ($R_b/R_m$=2), $l_{chain}$ is 3.4. Figure 5.8(b) indicates that $l_{chain}/N_p$ decreases with the increase of $R_b/R_m$. For small particle sizes of 0.05 m ($R_b/R_m$=20), the ratio of $l_{chain}/N_p$ is as small as 0.2, while for large grain sizes of 0.5 m ($R_b/R_m = 2$), the ratio of $l_{chain}/N_p$ is around 0.7. This result indicates that it is easier for samples composed of big particles to form longer force chains which connect through the medium thickness to develop strong strength against boulder's impact.

### 5.3.3   Effect of grain sizes on chain age

This part investigates the chain age inside the impacted medium. Two notions are proposed: the life-span of a force chain, and the age of a force chain. The life-span is counted back from the time when the chain disappears to the time when it appears. The age of a force chain is counted from a reference time back to the initial time when it appears. If a chain disappears before the reference time state, its chain age equals to its chain life-span.

Two 2D samples composed of particles of $R_m$=0.05 m and $R_m$=0.2 m are taken as examples. Since the investigation is mainly interested in investigating the link between the force chain age and the impact force peak, only force chains appeared before the impact force peak are considered. Since larger number of force chains exists in the case of $R_m = 0.05$ m than in the case of $R_m = 0.2$ m, the investigation is focused on the probability density distribution of chain age. Figure 5.9 indicates that the maximum chain age for the sample of $R_m$=0.2 m is 19 ms, while the maximum chain age for sample of $R_m$=0.05 s is 16 ms. The density of chains whose age is younger than 2 ms is larger
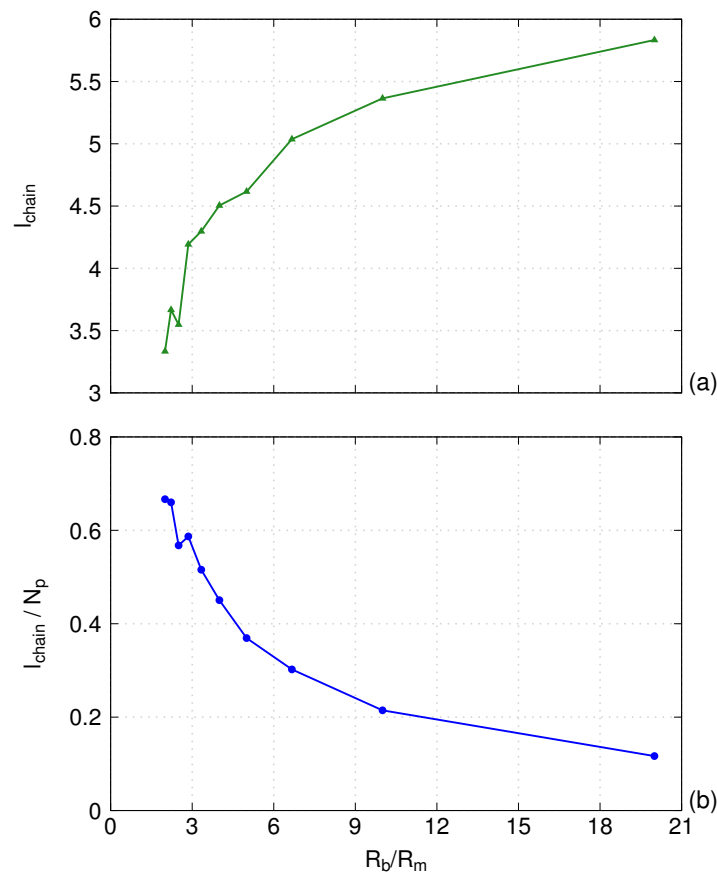
*Figure 5.8:* *Evolution of (a) $l_{chain}$ and (b) $l_{chain}/N_p$ versus $R_b/R_m$*

inside sample of $R_m$=0.05 m (0.48) compared to sample of $R_m$=0.2 m (0.38). The results indicate that more percentage of force chains in the case of $R_m = 0.2$ m have longer ages, in another word, they are more stable.

The results indicate that a higher impact force peak on the boulder in sample composed of big particles is related to a relatively larger chain length with respect to the medium thickness, as well as a higher density of larger chain ages. The relation confirms the role of force chains on the mechanical impact force on the boulder. The load transfer mechanisms inside the impacted medium will be characterized in the next section.
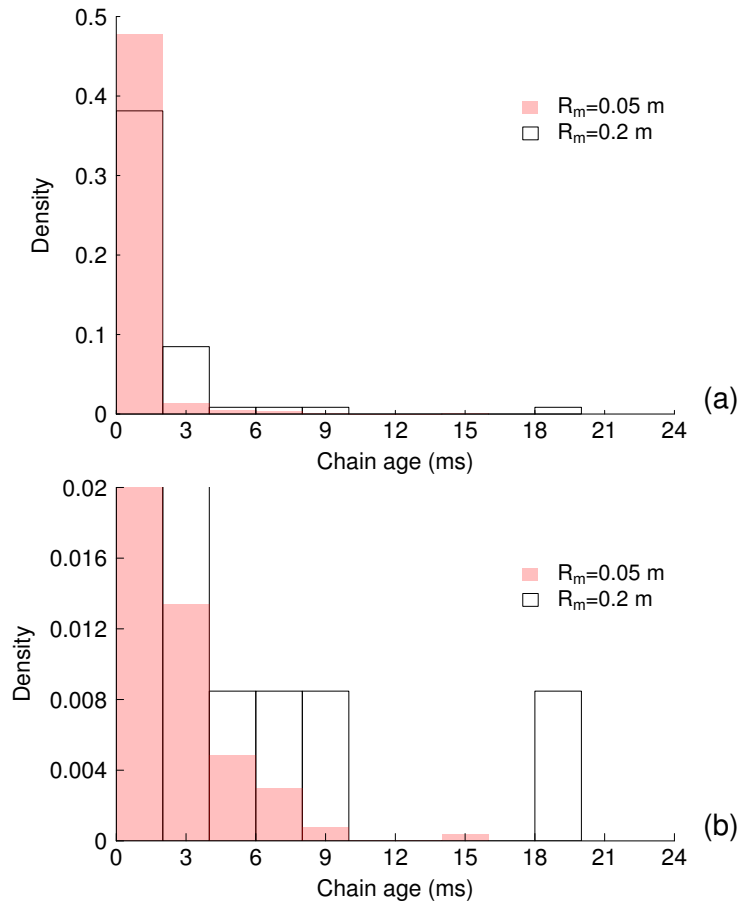
**Figure 5.9:** *(a) Probability density distribution of chain age, (b) Zoom of (a)*

# 5.4 Spatial and temporal evolution of force chains

The load transferred between the boulder and the medium during the interaction is conducted through force chains. The aim of this section is to investigate the role of force chain in load transfer mechanisms inside the impacted medium through the spatial and temporal evolution of force chains. The spatial structure of force chain propagation is investigated based on the study of Clark et al. (2014). The load transfer in the vertical direction of the sample is investigated by characterizing the chain particle populations inside a conical volume, while the load transfer in the lateral direction of the sample is investigated by characterizing the critical length of a homogeneously distributed chain domain ($HDCD$). The investigations are mainly conducted corresponding to 3D the impact case of $R_b$=1.17 m, $H$= 3 m.

### 5.4.1   Spatial structure of force chains

Recently, Clark et al. (2014) experimentally studied force propagation into 2D granular material during impact from an intruder. They determined the speed and spatial structure of the force response using high speed video and photoelastic particles. The results show that these quantities depend on a dimensionless parameter $M'$

$$M' = t_c v_0 / d \tag{5.4}$$

where $v_0$ is the intruder speed at impact, $d$ is the particle diameter, $t_c$ is the collision time for a pair of grains impacting at relative speed $v_0$. They observed that for low $M'$ ($M' \ll 1$), strong force networks are spatially sparse and inhomogeneous, force propagation is chainlike with a speed $v_f$ satisfying

$$\frac{v_f}{v_b} \propto \left(\frac{v_0}{v_b}\right)^{\frac{\alpha - 1}{\alpha + 1}} \tag{5.5}$$

where $v_b$ is a characteristic sound speed inside a grain. The networks become more spatially dense and homogeneous and the force propagation speed $v_f$ departs from equation (5.5) as $M'$ increases (Figure 5.10).

In the study of Clark et al. (2014), the expression

$$v_f = 1.2 v_b \left(\frac{v_0}{v_b}\right)^{\frac{\alpha - 1}{\alpha + 1}} \tag{5.6}$$

fits satisfactorily all the data (with $\alpha = 1.4$), except for the softest particles ($M' \approx 0.6$).

Investigations are conducted to see which impact regime proposed by Clark et al. (2014) the impact simulation of $R_b$=1.17 m, $H$=3 m corresponds. One thing to keep in mind is that different materials are used in this numerical modelling and the experiments. In the work of Clark et al. (2014), the derivation of the collision time between two particles is governed by a force which varies as a power law in particle compression, while $t_c$ in this study is obtained by allowing two identical particles of 0.2 m radius to impact with an relative velocity of $v_0$ based on a linear normal contact law, $t_c$=0.0047 s (see chapter 4).
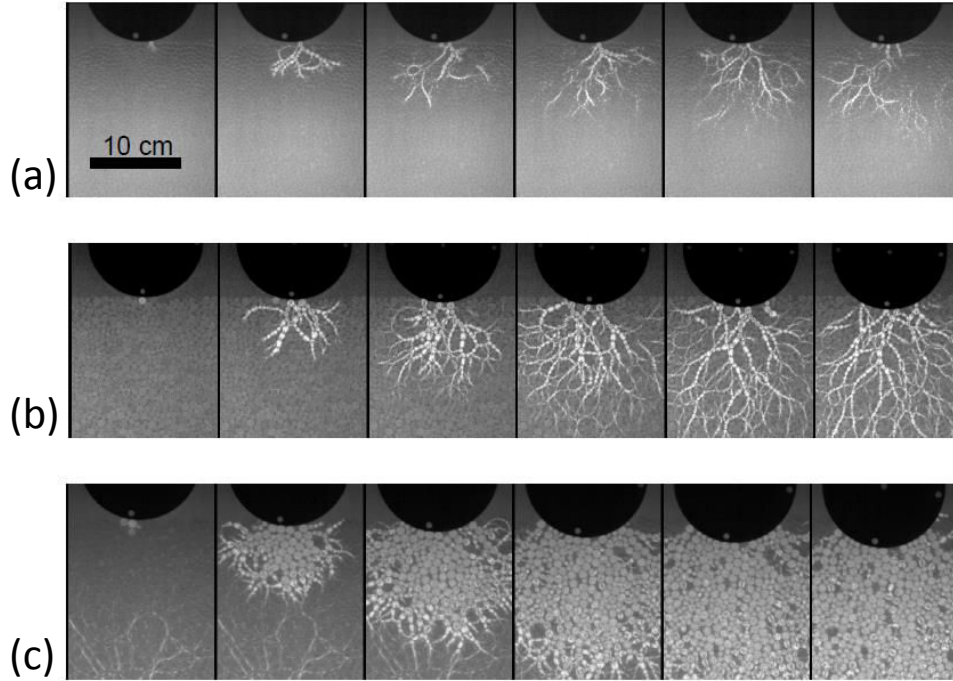
**Figure 5.10:**  *Propagating stresses at impact force for all three sets of particle used. (a) harder particles (M′ ≈ 0.1) correspond to fast, chain-like force propagation, (b) forces for intermediate stiffness particles (M′ ≈ 0.3) are spatially more dense, but still relatively chain-like. (c) the softest particles (M′ ≈ 0.6) show a dense force structure which propagates with a well defined front (Clark et al., 2014).*

The dimensionless parameter $M'$ obtained in this study is $M' = t_c v_0 / d = 0.0047 \times 20/0.4 = 0.24$, with $t_c$=0.0047 s, $d$=0.4 m, $v_0$=20 m/s. Thus theoretically, the impact case in this study approximately corresponds to the second regime (Figure 5.10(b)). Therefore equation (5.6) is adopted to calculate approximately the force propagation velocity in this impact case, with

$$v_b = \sqrt{\frac{E}{\rho}} \tag{5.7}$$

where $E$ is the Young modulus (a value of 75 MPa is obtained based on the stress-strain behaviour of quasi-static triaxial test, see figure 3.11), $\rho$ is the bulk mass density of the particles (in this study, $\rho = 1600$ kg/m$^3$), therefore, $v_b$ is 217 m/s. Based on this, a value of 175 m/s is obtained for $v_f$ (equation (5.6)), which is very close to the compression wave velocity of 200 m/s obtained in chapter 3.
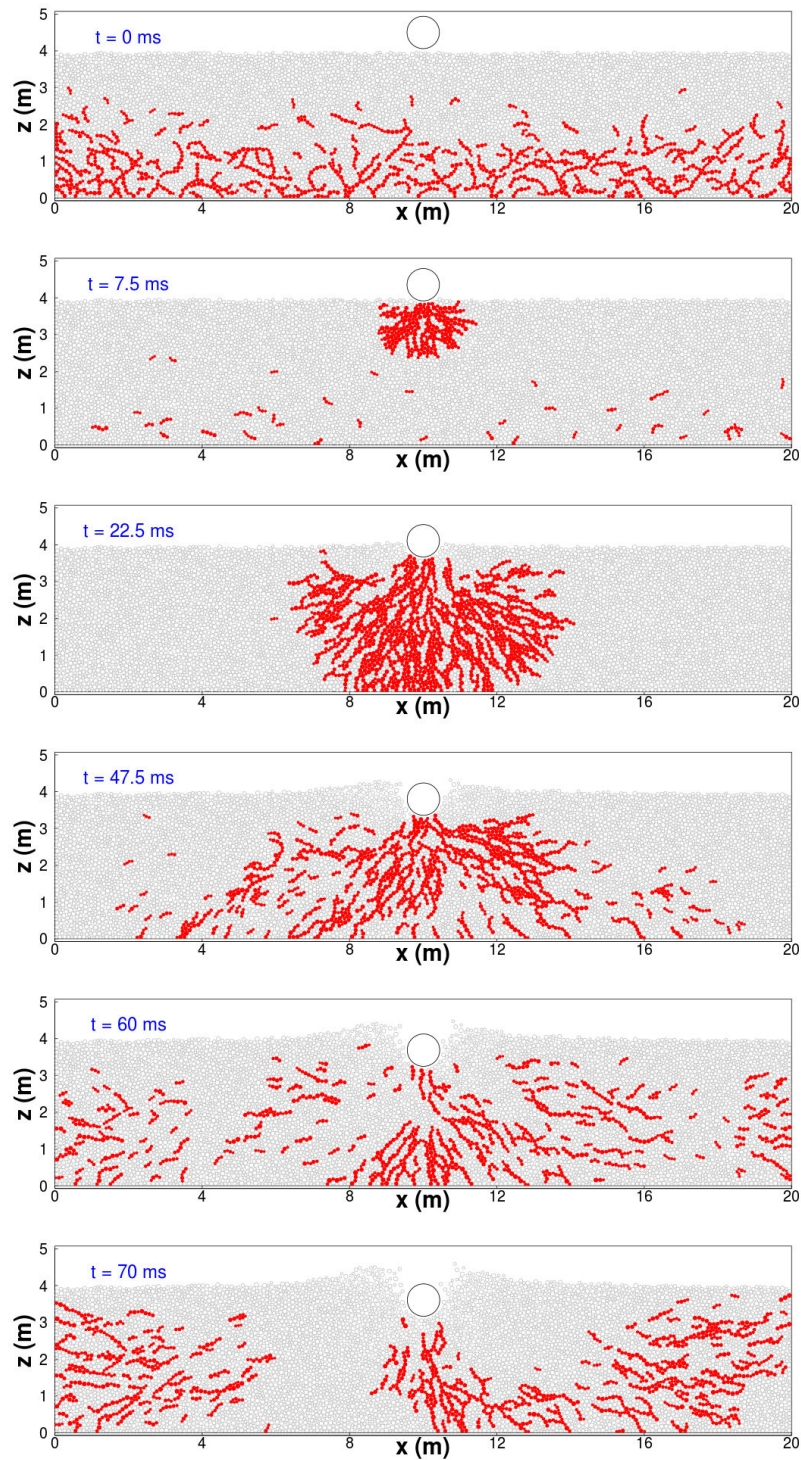
***Figure 5.11:*** *Evolution of force chain network inside a 2D impacted medium*

Figure 5.11 illustrates the propagation of force chains inside an impacted medium corresponding to a 2D impact case, where the average diameter of particles is 0.1 m, the collision time of two corresponding identical particles is 0.0012 s, the impact velocity of the boulder is 20 m/s. Thus the dimensionless parameter $M'$ obtained for this case is 0.24, which corresponds to a second regime (same as the 3D impact case). This is confirmed by figure 5.11. The force network developed in this impacted medium is spatially dense but still relatively chain-like structure.

## 5.4.2 Chain particle distances

The chain particle distance is defined as the distance between two chain particles. The variation of chain particle distances offers informations of population and spacial distribution of chain particles. The distances between chain particles are quantified by using the radial distribution function (Mueth et al., 1998), which is illustrated as:

$$g(l) = \sum_{i=1}^{N-1} \sum_{j=i+1}^{N} \delta(l_{ij} - l) \tag{5.8}$$

where $g(l)$ is the radial distribution function; $l_{ij}$ is the distance between two particles $i$ and $j$ which belong to two different force chains, the cases of two particles belonging to the same force chain are avoided to eliminate inter-correlations; $N$ is the total number of chain particles; $\delta$ is the Kronecker function. In order to take the distance of each pair of chain particles into account, it is supposed that if $0 < l_{ij} - l < a d_m$, then $l_{ij} - l = 0$, $d_m$ is the mean diameter of grains, $a = 0.2$.

Distribution of chain particle distances is shown in figure 5.12, the chain particle distance is normalized by the average particle radius. The analysis mainly focuses on the shapes of the distributions as well as the peak values. Before impact ($t = 0.00$ s), a peak value of chain particle distances is observed for $l = 47.6\ R_m$. As impact starts, at $t = 0.04$ s, the peak value decreases and is observed for $l = 26\ R_m$. In addition, the area of the surface below the curve decrease compared to the time of $t = 0.00$ s. These results indicate that both the number of chain particles as well as the distance between chain particles decrease, the chain particles generally become closer to each other. As impact continues, at $t = 0.08$ s for instance, the distribution curve goes above the curve corresponding to the case of $t = 0.00$ s, moreover, two peaks are slightly
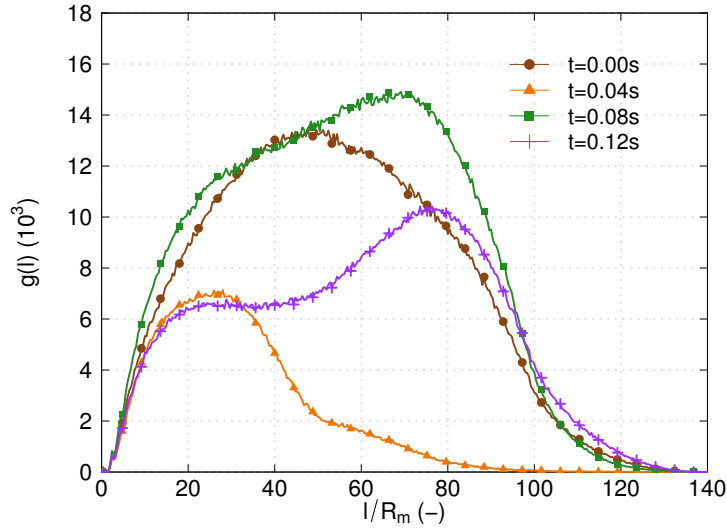
***Figure 5.12:** The radial distribution function of chain particle distances*

observed. The results indicate that more force chains are developed, besides, the appearance of the two peaks indicates that force chains are self-aggregated in different parts of the sample. The observation of two peaks for the case of $t = 0.12$ s is more pronounced.

The aggregation of chain particles in different parts of the sample indicates the bi-aggregation character of the chain particle distributions. Force chains mainly locate in several parts of the medium, one central part between the boulder and the bottom boundary, other approximately symmetrical lateral parts between the medium center and the lateral boundaries (Figure 5.11).

The bi-aggregation character inside the impacted medium results from the load transfers mechanisms and the boundary conditions. In this impact case, the medium thickness is 3 m, the medium length and width are 20 m, thus the bottom boundary effects are more important than lateral boundary effects. According to the energy propagation process demonstrated in chapter 4, the central volumes between the boulder and the bottom boundary are characterized by larger amount of elastic strain energies, therefore, force chains between the boulder and the bottom boundary contributes to the main strength of the medium. On the other hand, force chains also transfer inside the lateral volumes as indicated by their spatial chain particle distributions. These results indicate that there are self-organization and propagation of force chains during the impact process.

### 5.4.3 Population of chain particles and average chain distance inside the conical volume

As shown in chapter 4, the main strength of the medium to the impact of boulder is contributed by the particles in the central volumes between the boulder and the bottom boundary. A 3D conical volume inside the medium is defined as having the same value of height and bottom radius. Figure 5.13 shows a vertical section of the conical volume. The aim is to investigate the relation between force chains within the conical volume and the impact force on the boulder as well as the velocity of the boulder.
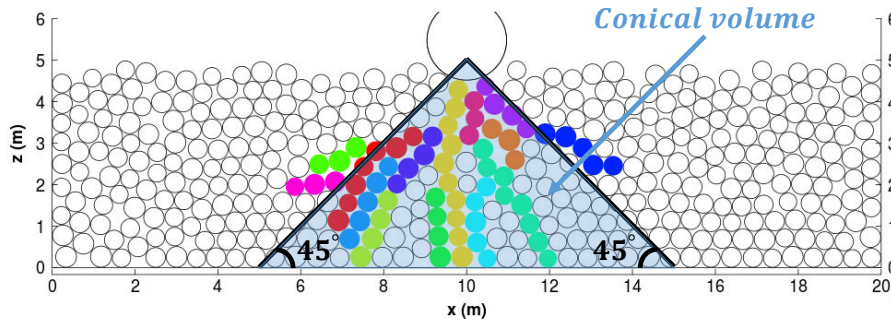


**Figure 5.13:** *A vertical section of the conical volume*

For this purpose, $p^{cv}$ is defined as the ratio of the number of chain particles to the total number of particles inside the conical volume. In addition, the average chain distance inside the conical volume is an important property which relates not only to the spatial distribution of chains but also to the strength of the medium. The average chain distance $d_c^{cv}$ is calculated as:

$$d_c^{cv} = \sqrt[3]{\frac{V^{cv}}{n_c^{cv}}} \tag{5.9}$$

where $n_c^{cv}$ is the number of chains inside the conical volume, $V^{cv}$ is the volume, $V^{cv} = \frac{1}{3}\pi H^3$.

Figure 5.14 shows that $p^{cv}$ follows approximately the same trend as $F_{boul}$. Before the impact, chain particles in the conical volume only occupy 10% of the total number of particles due to gravity. $p^{cv}$ increases as impact starts, which indicates that more particles participate in load transfer, meanwhile, the impact force on the boulder increases and
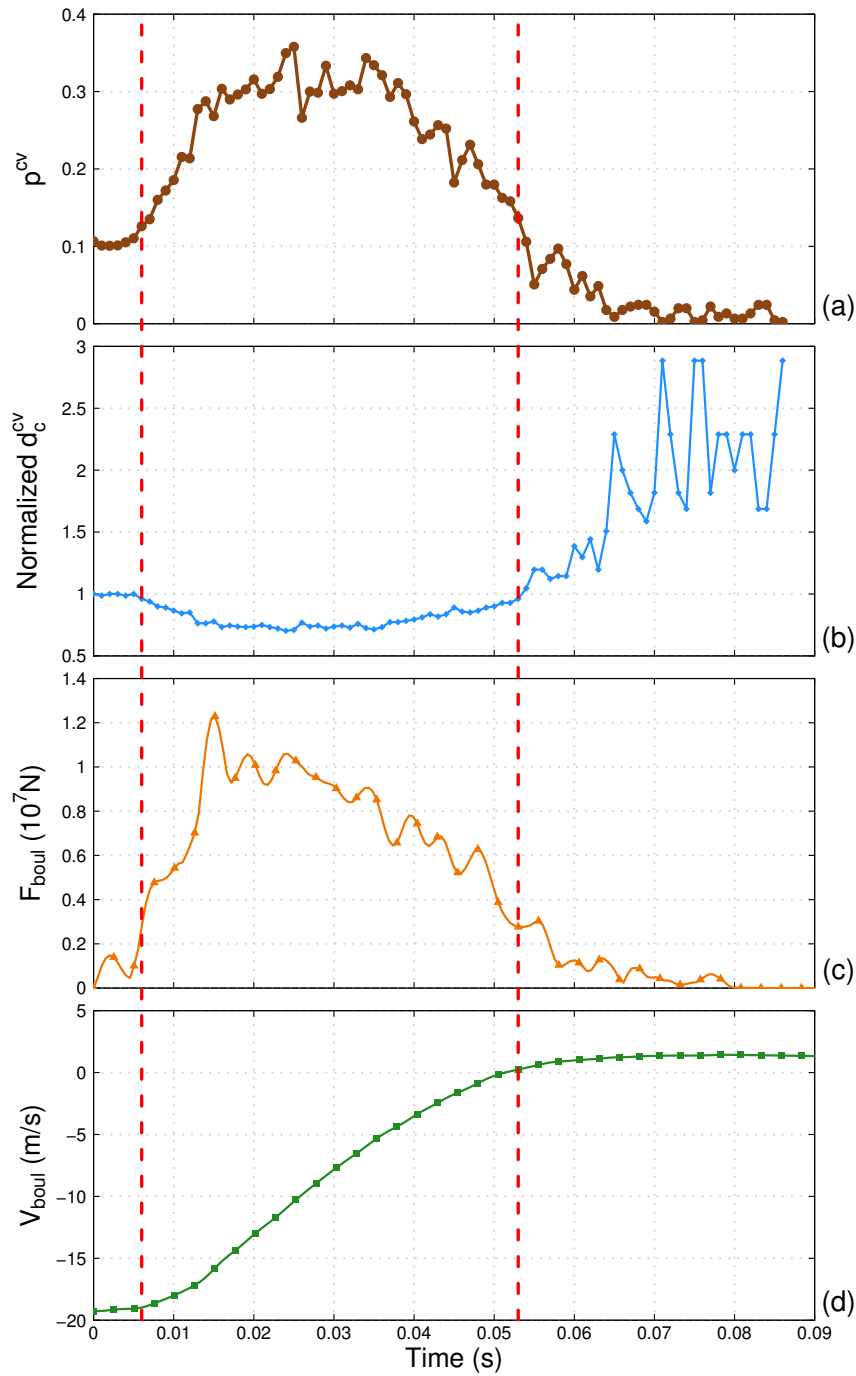
**Figure 5.14:** *Time evolution of (a) Percentage of chain particles in the conical volume $p^{cv}$, (b) Normalized chain distance $d_c^{cv}$, (c) Impact force on the boulder $F_{boul}$ and (d) Velocity of the boulder $V_{boul}$*

the velocity of boulder decreases. The peak value of $p^{cv}$ is around 36%. After the time of 0.035 s, the decrease of $p^{cp}$ corresponds to the decrease of $F_{boul}$. $p^{cv}$ equals to small values (0.02-0.04) when impact force on the boulder equals zero.

Figure 5.14(b) shows the time evolution of the $d_c^{cv}$ (normalized by the initial value), $d_c^{cv}$ is smaller than the initial value from 0.006 s to 0.053 s which indicates that the chains become closer. The minimum value is 70% of the initial value. In addition, highest values of $F_{boul}$ fall in the range of 0.006-0.053 corresponds to the situation where force chain are very close. After the time of 0.06 s, the number of chain particles decreases, besides, the distance between chains becomes larger (Figure 5.14(a) and (b)). The increase of $d_{chain}$ is related to the decrease of chain density as well as the decrease of strength of the medium.

### 5.4.4 Critical length $l_{HDCD}$

This subsection investigates the temporal propagation of force chains in the lateral direction. The notion of homogeneously distributed chain domain $HDCD$ is proposed. $HDCD$ is a cuboid domain centred inside the medium where the force chain particles are homogeneously distributed (Figure 5.15). The quantification of the load transfer mechanisms can be roughly conducted by quantifying the time evolution of the dimension of $HDCD$.

Several assumptions are made to characterize the dimension of the $HDCD$ domain. First of all, the heterogeneous distribution of chain particles in sample thickness $z$ direction is not considered here, the thickness of the domain $HDCD$ equals the medium thickness $H$. Second, due to the fact that the boulder impact point is located on the center surface of the medium, it is supposed that chain distributions in sample length $x$ and width $y$ directions are not only similar but also both symmetrical with the impact point. Therefore, only one critical length $l_{HDCD}$ is used to characterize the dimension of $HDCD$. The item $l_{HDCD}$ thus represents the half length of the homogeneously distributed chain domains in the $x$ direction. The evolution of $l_{HDCD}$ is used to quantify the load transfer inside the impacted medium.

The method for selecting $l_{HDCD}$ is described as follows:
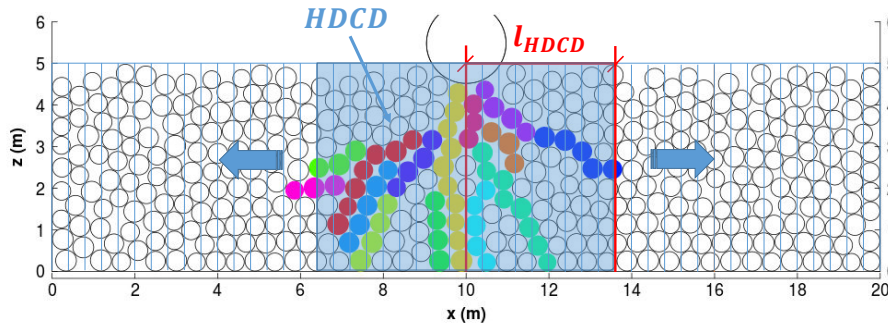
**Figure 5.15:** *Description of chain section sub-divisions*

1. Vertically divide the sample into sections (starting from the impact location). The length of each section equals average particle diameter $d_m$ ($d_m$=0.4 m). Therefore, there are $m$ sections in total, $m = \dfrac{L}{2d_m} = 25$, where $L$ is the medium length, $L$=20 m.

2. Suppose $p_x$, $p_y$, $p_z$ are the $x$, $y$, $z$ coordinates of a particle respectively. The criterion for a chain particle locates within a section is that $p_x$ locates inside that section. Count the number of the chain particles inside each section (the axial symmetrical sections with the impact location are considered together). $n_i$ is the number of chain particles inside $i^{th}$ section, $i \leq m$. An illustration of the algorithm is shown in figure 5.15.
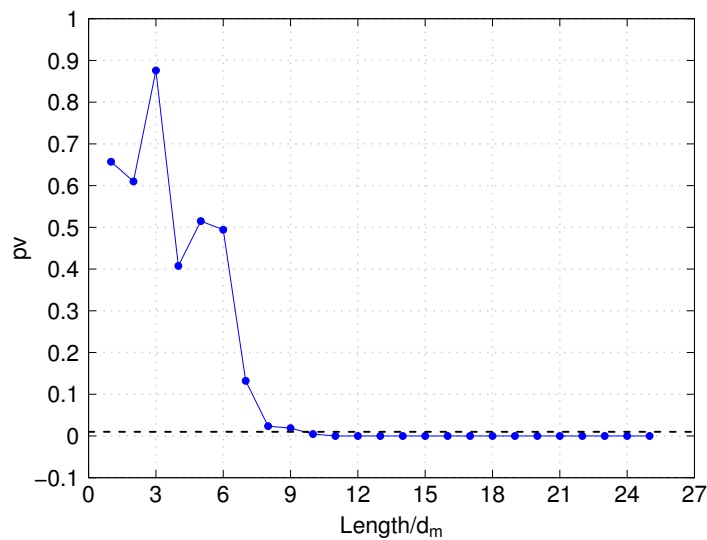


**Figure 5.16:** *Distribution of chi-square p-values for $t = 0.04$ s, the dotted line represents pv=0.01*

3. $l_{HDCD}$ is selected based on the criterion that the chain number in each section of the $HDCD$ has an equal population distribution. Correspondingly, the chi-square test is adopted for this purpose. More specifically, at $t$ time, if the p-value $pv_{i,t}$ of the chi-square test for a vector $N_i = (n_1, n_2, ..., n_i)$ is larger than a cut off value (0.01 for instance), the hypothesis is made that the population probabilities of chain number in each section is equal. Thus, $pv_{i,t}$ can be plotted as a function of the length variable (Figure 5.16). The criterion for selecting $l_{HDCD}$ is:

$$\text{If} \qquad \max(pv_{i+1,t}, \frac{\sum_{j=i+1}^{m} pv_{j,t}}{m-i}) < pv_{i,t} < \overline{pv}, \qquad \text{then} \qquad l_{HDCD,t} = id_m \quad (5.10)$$

Where $\overline{pv}$ is the critical p-value, $\overline{pv} = 0.01$. At the time of 0.04 s (Figure 5.16), $l_{HDCD}$ obtained according to the algorithms is $10d_m$.

Figure 5.17(a) shows the time evolution of $l_{HDCD}$. At the very beginning of the impact, $l_{HDCD} = 25d_m$ (equals to the half length of the sample), force chains are uniformly distributed in the $x$ direction of the whole sample due to gravity. Shortly after impact starts, the critical length rapidly decreases. A minimum value of $7d_m$ is reached at the time of 0.02 s, which indicates that the force chains particles are aggregated near the impact point to participate in the strength of the medium. Afterwards, $l_{HDCD}$ increases up to a peak value of $25d_m$ at 0.07 s, which indicates that force chains propagate and $l_{HDCD}$ reaches the lateral boundaries of the medium. After the time of 0.075 s, $l_{HDCD}$ decreases due to the reflection of load transfers from lateral boundaries.

Even though the time evolution of $l_{HDCD}$ quantifies lateral load transfers and reflections inside the impacted medium, the load transfer in the conical volume is much more important and directly influences the impact force and the velocity of the boulder. The load transfer in the lateral direction can be considered as a second-order mechanism.
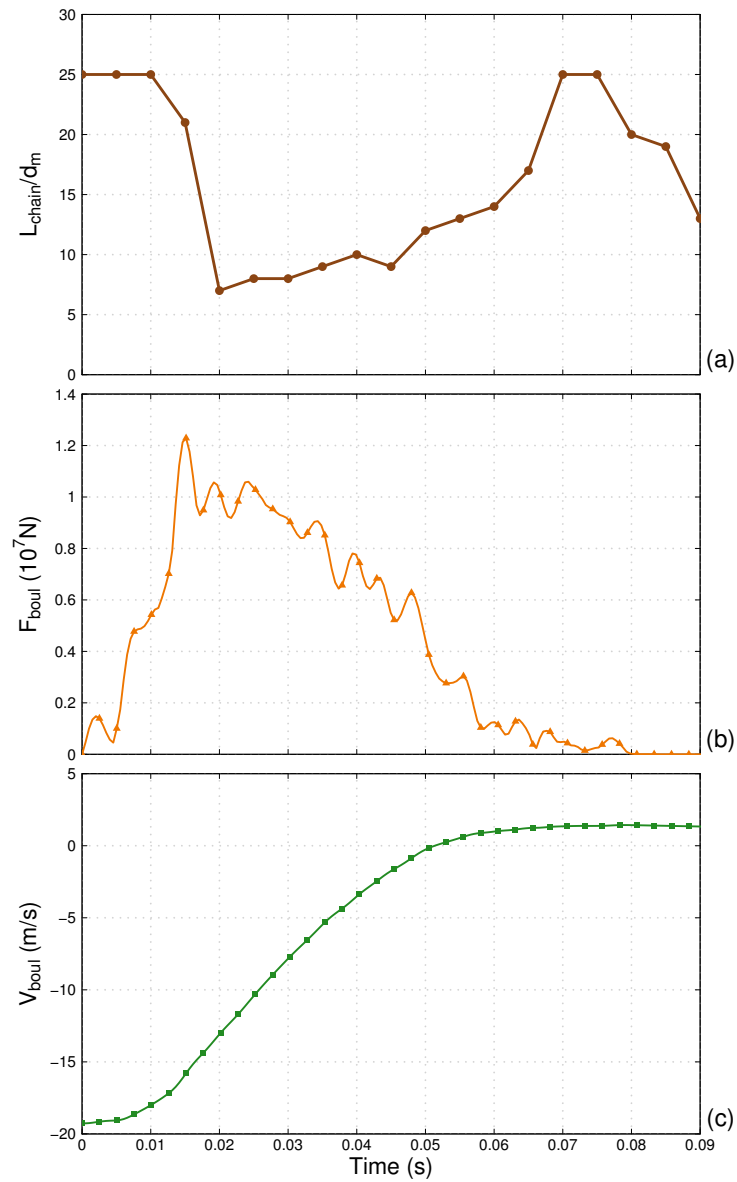
**Figure 5.17:** *Time evolution of (a) $l_{HDCD}$, (b) impact force $F_{boul}$ and (c) boulder velocity $V_{boul}$*

## 5.5   Force chain buckling mechanisms

The micromechanical load transfer inside the impacted medium not only involves the spatial and temporal evolution of force chains, but also the failure of force chains. In this section, the force chain buckling related mechanisms are investigated. The aim is to investigate the role of force chain buckling in the development of the impact force on the boulder, as well as in the microstructure evolution and energy transfer process inside the medium.  First, the algorithm for force chain buckling is introduced.  The investigation includes the properties of force chain buckling (the buckling angle, the buckling number).  Second, the triggering mechanisms and the energy dissipation of buckling are investigated. Third, the relations between force chain buckling, impact force and energy items are investigated. All the investigations are conducted based on the 3D impact case of $R_b$=1.17 m, $H$= 3 m.

### 5.5.1   Buckling angle and buckling number

The buckling of forth chain is related to the failure of three chain particle segments. The definition of force chain buckling (Tordesillas et al., 2014) is based on geometry variation of chain particles: suppose at a time $t$, a three-chain-particle segment exists, at time $t + \delta t$, a buckling event has occurred if (Figure 5.18):

$$\alpha = \frac{|\theta_t - \theta_{t+\delta t}|}{2} > \theta_b \tag{5.11}$$

where $\theta_b$ is a threshold parameter. The case of the three-chain-particle segment dying at time $t + \delta t$ is not considered as a buckling. In this study, the time difference $\delta t$ for buckling identification equals to 0.001 s.

The average buckling angle $\bar{\alpha}$ for all force chain segments is calculated. In this case, all the force chain segments are considered as soon as their geometry intersection angle varies. The time evolution of $\bar{\alpha}$ in figure 5.19(a) indicates that after impact starts, a rapid increase of $\bar{\alpha}$ is observed, a peak value of 0.06° is reached around 0.027 s.  The small buckling angle obtained is due to the tiny displacement (0.2% of the particle average diameter) between the two close time states ( 0.001 s of time interval).
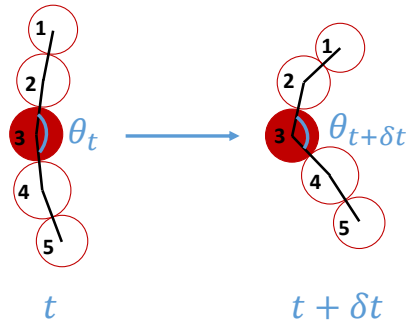
*Figure 5.18:* *Geometry change of three particle segments during a force chain buckling event*

Figure 5.19(b) shows the time evolution of buckling number for four different $\theta_b$. Similarly, a rapid increase of buckling number is observed shortly after impact starts. The larger the criterion angle $\theta_b$, the smaller the peak value, and slightly earlier the peak value is reached. The buckling number peaks are 152, 81, 32, 11 for $\theta_b$ equals $0.05°$, $0.1°$, $0.2°$, $0.4°$ respectively. The corresponding occurrence time of the buckling number peak are 0.028 s, 0.027 s, 0.023 s and 0.017 s respectively. The small value of the buckling angle is due to the tiny relative displacements between particles during the time variation of $\delta t$.
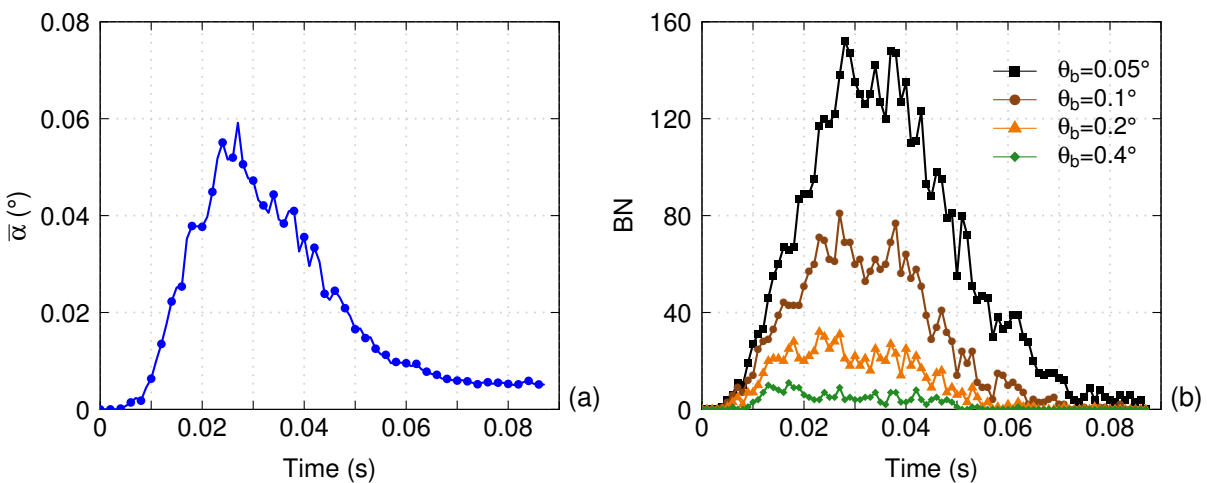


*Figure 5.19:* *Time evolution of (a) average buckling angle $\bar{\alpha}$ and (b) buckling number BN*

### 5.5.2 Triggering and energy dissipation of force chain buckling

In order to investigate the triggering and the energy dissipation of buckling chains, the evolution of buckling number ($BN$), relative translational velocity ($Rel\_v$), relative rotational velocity ($Rel\_w$) as well as ratio of energy dissipation ($Ratio\_E_d$) in buckling segments versus $\theta_b$ are investigated (Figure 5.20). $Ratio\_E_d$ is defined as the ratio of buckling segments with energy dissipation to the total number of buckling segments. All of the items are normalized by the corresponding maximum value.
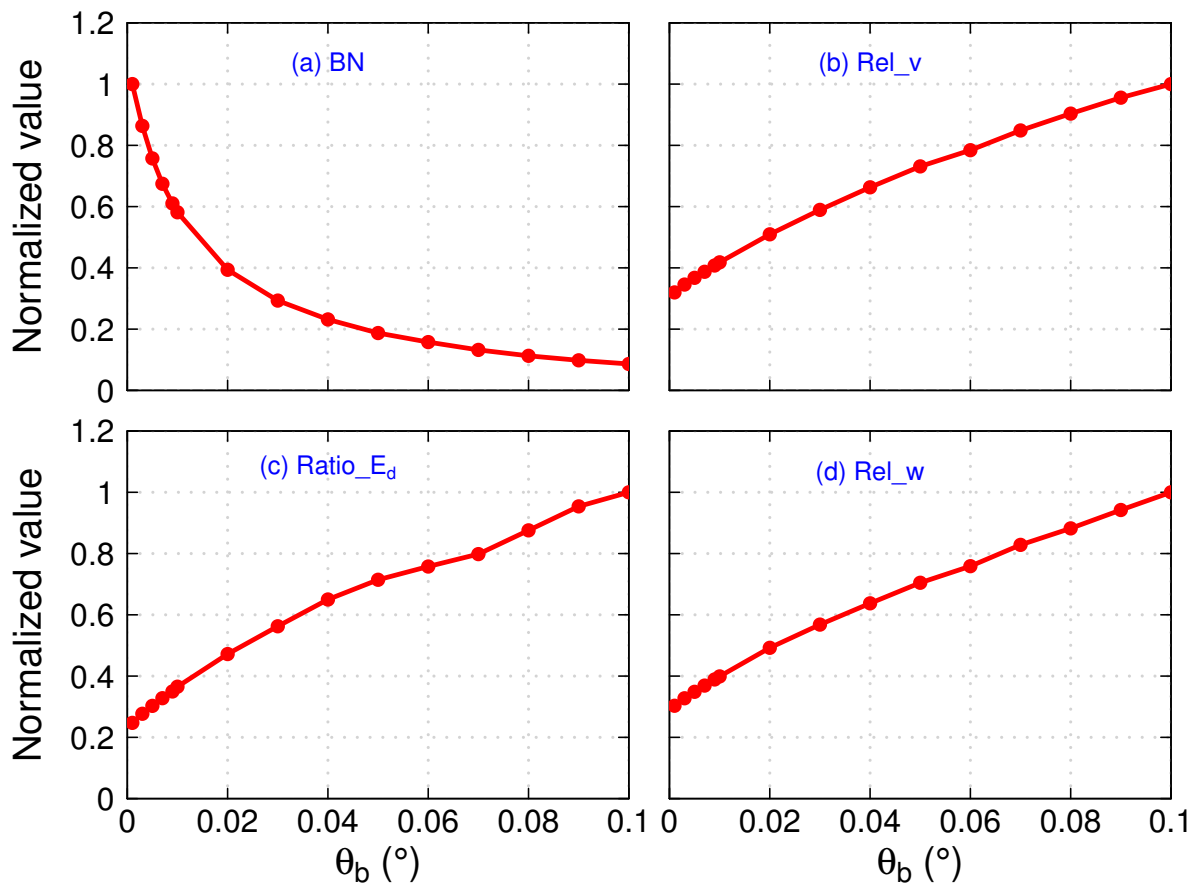


***Figure 5.20:*** *Evolution of buckling number (BN), ratio of energy dissipation segments to the total buckled force chain segments (Ratio_E_d), relative translational velocity (Rel_v) and relative rotational velocity (Rel_w) versus the buckling criterion angle $\theta_b$*

Figure 5.20 indicates that with the increase of $\theta_b$, $BN$ decreases, $Rel\_v$ and $Rel\_w$ increase, $Ratio\_Ep$ increases. The results indicate that the buckling of force chains is triggered by the relative movements between the contacting grains. In addition, the buckling is relevant with energy dissipations, especially for strong buckling characterized by a big $\theta_b$.

Further investigations are conducted to quantify the energy dissipations during the buckling events ($\theta_b$ adopted in following studies is $0.05°$). Inside each buckling segment, four situations might exist: no energy dissipation, energy dissipation due to frictional sliding, energy dissipation due to frictional rolling, energy dissipation due to both frictional sliding and rolling. Buckling without friction dissipation is due to contact opening.

An algorithm is proposed to quantify the contribution of energy dissipation by frictional sliding and rolling in buckling contacts, for each buckling segment,

$$
\begin{cases}
\alpha_{s,i} = \dfrac{InE_{ds,i}}{InE_{ds,i} + InE_{dr,i}} & \text{and} \quad 0 \leq \alpha_{s,i} \leq 1 \\[4mm]
\alpha_{r,i} = \dfrac{InE_{dr,i}}{InE_{ds,i} + InE_{dr,i}} & \text{and} \quad 0 \leq \alpha_{r,i} \leq 1
\end{cases}
\tag{5.12}
$$

where $\alpha_{s,i}$ and $\alpha_{r,i}$ are the proportion of energy dissipation by frictional sliding and by frictional rolling inside the $i^{th}$ buckling segment. $InE_{ds,i}$ and $InE_{dr,i}$ are the energy dissipation due to frictional sliding and frictional rolling for the $i^{th}$ buckled force chain segment respectively.

For the total $N$ number of frictional buckling segments (eliminate those buckling due to contact opens), the percentage of frictional sliding $A_s$ and frictional rolling $A_r$ are defined as:

$$
\begin{cases}
A_s = \sum\limits_{i=1}^{N} \alpha_s \\[4mm]
A_r = \sum\limits_{i=1}^{N} \alpha_r
\end{cases}
\tag{5.13}
$$

Figure 5.21(a) shows the time evolution of frictional buckling number and $As$, $Ar$. The number of buckling contacts with sliding energy dissipation is much larger than that with rolling energy dissipation. This is consistent with the case of the energy dissipation within the whole sample where the sliding energy dissipation plays a more important
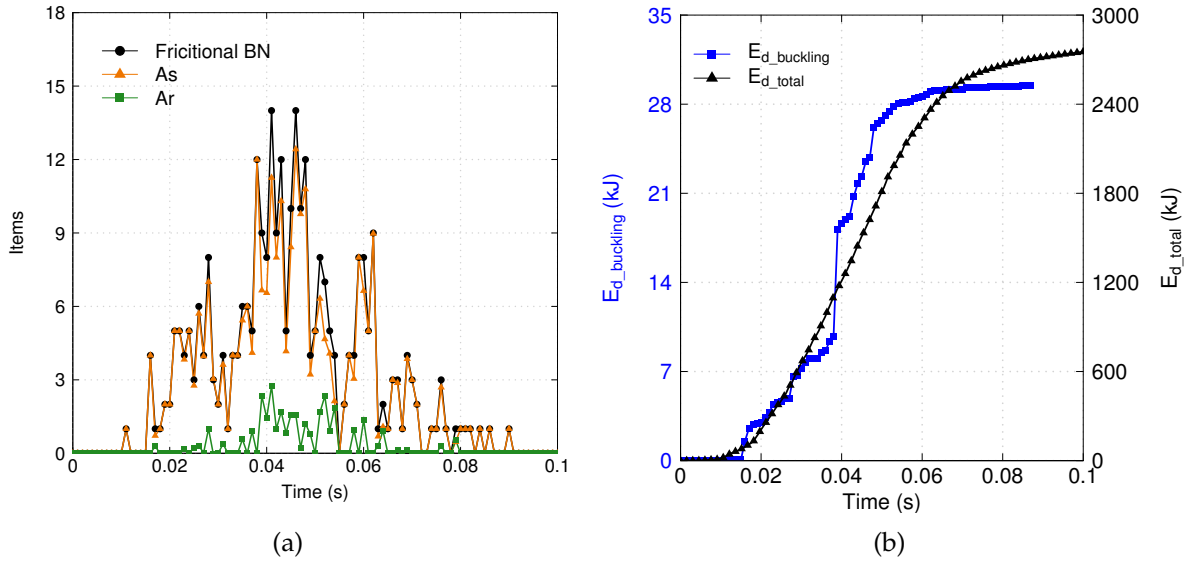
***Figure 5.21:*** *Effects of number of particles on (a) Evolution of AS and AR versus time, (b) Comparison of energy dissipation by force chains buckling*

role. The contribution of energy dissipation by frictional sliding is much larger than frictional rolling, which highlights the importance of frictional sliding in buckling contacts, while energy dissipation by frictional rolling is secondary. This is due to the adoption of rolling resistance in the simulation.

This investigation offers supplementary information of the bimodal character of the granular material, that is, the buckling of force chains also dissipates energy. It is worth reminding that the energy dissipation by buckling force chains is very limited compared to the total energy dissipation. More specifically, till the time of 0.09 s, the energy dissipation by force bucking is about 30 kJ, which is only 1% of total energy dissipation (Figure 5.21(b)). Therefore, the energy dissipation inside the granular medium is mainly associated to the weakly loaded contact network.

### 5.5.3 Relations between buckling, impact force and energy items

In order to investigate the role of force chain buckling in the evolution of medium's strength and microstructure evolution of granular materials, the time evolution of impact force on the boulder $F_{boul}$, kinetic energy of the medium $E_k$, incremental energy dissipation $InE_d$ and the buckling number $BN$ are plotted together to investigate their relations

(Figure 5.22). $InE_d$ is the incremental energy dissipation for the whole granular medium. A buckling criterion angle $\theta_b$ of 0.05° is adopted here. All the items are normalized by the corresponding maximum value.

Figure 5.22(a) indicates that the buckling number peak is reached later than the peak of the impact force. More specifically, at the time corresponding to impact force peak, the buckling number only reaches 20% of the maximum value, while at the time corresponding to the buckling number peak, the impact force on the boulder decreases to 54% of the maximum value. Indicated by figure 5.3 and figure 5.14, the increase of impact force on the boulder is correlated with the increase in particle compression stress as well as the number of force chain particles (which reflect the strength developed by the medium to resist the impact of the boulder), thus the increase of buckling number is secondary at this stage. After the impact force peak, the collapse of the strong force network is more dominating, which is reflected by the large number of force chain buckling.

Therefore, the development and the buckling of force chains are responsible for the evolution of impact force on the boulder. The increase of impact force is related to the increase of force chains, and the decrease of impact force is related to the increase of buckling number.

Figure 5.22(b) indicates that the kinetic energy peak and incremental energy dissipation peak are reached at same time, which is later than the arriving time of the impact force peak. The increases in kinetic energy and energy dissipation are related to the the strong rearrangement of the impacted medium, which corresponds to the reduction of strength and the impact force on the boulder.

Figure 5.22(c) indicates that kinetic energy peak, incremental energy dissipation peak, buckling number peak are reached at the same time. This is consistent with the fact that the buckling of force chains is triggered by the strong rearrangement of particles. In addition, force chain is related to the microstructure of the medium characterized by the decrease in coordination number inside the impacted medium, which relates to the increase of elastic strain energy and kinetic energy.
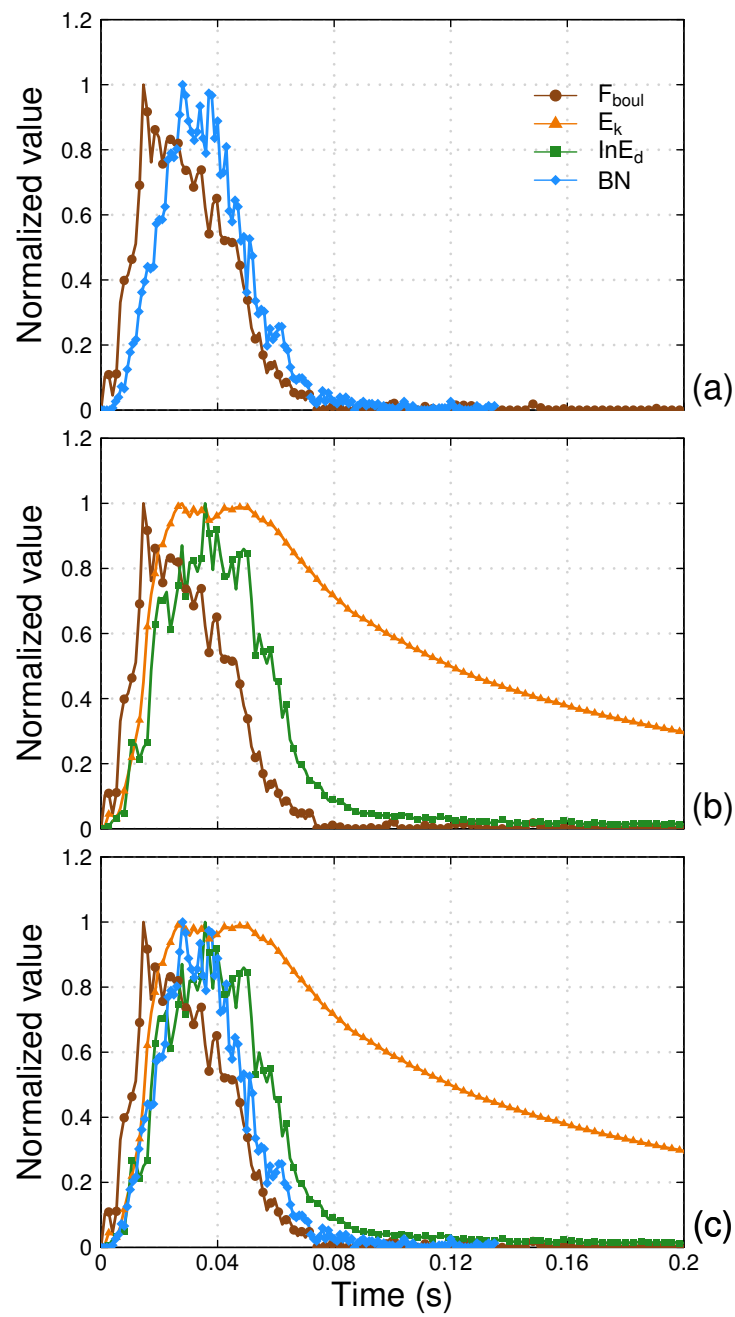
***Figure 5.22:*** *Correlation of buckling number BN with impact force on the boulder $F_{boul}$, kinetic energy of the medium $E_k$ and incremental energy dissipation $InE_d$*

## 5.6   Potential of force chain micromechanisms for rockfall engineering

The investigation highlights the role of force chains in the strength and the microstructure of granular material. First of all, force chains developed in the medium are closely related to the impact force on the boulder. Larger chain particle population, bigger chain density, longer chain length with respect to the medium thickness, longer chain age are related to larger impact force on the boulder. In addition, studies in the literature indicate that force chains are supported by the surrounding grain clusters and force chain stability needs appropriate microstructural neighbours made up of dense grain clusters. The denser the clusters are, the more stable the connected force chains are (Arévalo et al., 2010; Tordesillas et al., 2014; Zhu et al., b,a). Second, the force chains are related to the microstructure and deformation of the medium. The buckling of force chains is related to the grain rearrangements, kinetic energy and energy dissipations inside the impacted medium.

Both the bouncing and the design of protection structures have great interests towards the development of force chains inside the impacted medium. The bouncing of boulder is related to the medium strength which depends on the force chains developed within the medium. The design of protection structures needs to know the buckling of force chains and the microstructure evolution within the granular medium. For example, the design of rocksheds (cushion layer thickness, concrete structure) depends on the force transmission inside the impacted medium. The design of embankment requires to address the deformation of the embankment during the impact.

To sum up, the micromechanical investigation have great potentials, it helps better predict the trajectory of the boulder by well charactering the bouncing, as well as well better design the protection structures (help chose the good material, reduce the impact force on the boulder, control the deformation of the structure).

## 5.7 Conclusion

This chapter mainly interests in investigating the role of force chains in the mechanical impact force on the boulder as well as the load transfer and the microstructure of the granular medium based on investigating the properties of chains (number of chain particles, chain length, chain particle distance, chain age, force chain buckling number).

First of all, force chains are shown to be responsible for the strength of the medium (reflected by the impact force on the boulder). Simulation results of identical boulder impacting mediums composed of various grain sizes indicates that the impact force peak on the boulder decreases with the decrease of grain size. In addition, investigation shows that the sample composed of big particles is characterized by longer fore chain length with respect to the medium thickness as well as larger percentage of long age chains.

Second, the spatial and temporal evolution of force chains are found to be convenient tools to quantify the mechanisms involved in load transfer inside the impacted granular medium. The spatial structure of the force propagation is spatially dense but still relatively chain-like based on the regimes proposed by Clark et al. (2014). The populations of chain particles in the conical domain is related to the impact force on the boulder. The evolution of the critical length $l_{HDCD}$ inside the homogeneously distributed chain domain $HDCD$ characterize the lateral load transfer inside the impacted medium. The high impact force on the boulder corresponds to large population of force chains in the central conical volume and to close chain particle distances, the force chain inside plays a fundamental role on the impact force, while the load transfer in the lateral direction of the medium plays a secondary role.

Finally, the force chain buckling mechanisms are investigated. The buckling of force chains is triggered by relative displacements between particles. Strong buckling is related to energy dissipation. Moreover, energy dissipation by frictional sliding is more dominating than by frictional rolling. Important relations exist among force chain buckling and the impact force on the boulder, kinetic energy, energy dissipation inside the impact granular medium. The increase of buckling number is related to the decrease of impact force on the boulder, as well as the increase of kinetic energy and energy dissipation inside the medium.

# Chapter 6

# Conclusions and perspectives

## 6.1 Conclusions

Boulder trajectory prediction and protection structure design are two issues particularly concerned in rockfall engineering. Both of this two issues are governed by the boulder-medium interaction. In this context, this thesis investigates the interaction of a falling boulder and a granular medium, including the bouncing of a boulder on a granular medium.

Models based on discrete element method are particularly relevant to integrate the discrete nature of the granular material and address dynamic impact problems. A 3D model is developed to model the interaction between a falling boulder and a granular medium. The boulder is modelled as a single sphere with an initial vertical velocity, the granular medium is modelled as an assembly composed of poly-disperse grains. The boundaries of the sample are set large enough to avoid boundary effects. An elastic-plastic contact law implemented with rolling resistance is used to model the impact process. Only frictional energy dissipation is allowed during the impact process. The contact parameters are calibrated based on quasi-static triaxial tests of Ticino sand, an angular sand which can approximately represent soils composed of natural or man-made slopes or rockfall protection structures. It is noticed that rolling resistance has effects in intensely increasing the peak value of the deviatoric stress in triaxial loading. The modelling of the impact process is validated by reproducing the impact force, impact

time, dynamic amplification, penetration depth of the experimental data. The model is supposed to be precise enough to capture the most important physics taking place during the impact process.

Based on the validated 3D impact model, this thesis investigates the global and micromechanical response of the granular medium. The main attention is put on the bouncing of the boulder and the impact force on the boulder.

Local configurations of the medium surface are shown to have influences on the impact force and reflect velocity of the boulder. Statistical investigations suggest that 49 simulations of fixed incident conditions and various impact locations are sufficient to capture the average impact force and reflect velocity of the boulder in 3D impact cases. The impacted granular medium is divided into several crown volumes according to their distances from the impact point. Energy propagation processes (elastic strain energy, kinetic energy, energy dissipation) inside the impacted medium are investigated from crown to crown. The results show that impact induces the increase of elastic strain energy which is followed by a fluidization process characterized by the increase in kinetic energy, energy dissipation as well as the decrease in coordination number. In addition, the role of frictional sliding is more dominating than frictional rolling in these impact conditions, due to the introduction of rolling resistance.

Boulder's bouncing occurrence is investigated under various boulder size $R_b$ and sample thickness $H$ conditions. 2D and 3D impact cases are conducted for qualitative comparison purpose. The results show that the bouncing occurrence is consistent with the theories proposed by Bourrier et al. (2008). By divided the ($R_b$, $H$) plane into bouncing and non-bouncing domains, three regimes are observed. For a small size boulder, boulder rebounds whatever the layer thickness. For a medium size boulder, the amplitude of the bouncing domain decreases with the increase of boulder size. For a large boulder, the amplitude of the bouncing domain increases with the increase in boulder size. In addition, boulder always rebounds in case of a shallow layer thickness.

Analyses together with impact force and velocity of boulder indicate that bouncing occurs either due to first impact or successive impacts with the granular medium. If the medium gives enough strength to the impact of boulder, boulder directly rebounds during the first impact. Otherwise the bouncing of boulder during the successive impacts depends on the strength of the medium as well as the residual incident energy of the boulder.

The response of the impacted medium is investigated from a micromechanical point of view. Force chain is particularly a signature of load transfers inside the impacted medium. The characterization of force chain network inside the impacted medium is based on particle principal stress information. The spatial structure of force propagation inside the impacted medium is spatially dense but relatively chain-like based on the regimes proposed by Clark et al. (2014).

The investigation shows that force chains are responsible for the impact force on the boulder. Simulations of boulder impacting different granular medium composed of different grain sizes show that the peak value of impact force decrease with the decrease in grain size. Meanwhile, for samples composed of large grains, the higher peak value of impact force on the boulder corresponds to longer force chains compared with medium thickness as well as long age of force chains. In addition, the high impact force on the boulder corresponds to large population of force chains in the central conical volume and to close chain particle distances. The force chains inside play a fundamental role on the impact force. Comparatively, the load transfer in the lateral direction of the medium characterized by critical length $l_{HDCD}$ plays a secondary role. The investigation of force chain buckling mechanism shows that, triggered by relative displacements between the chain particles, the increase of buckling number is related to the decrease of impact force on the boulder as well as the increase of kinetic energy, energy dissipation inside the granular medium.

Generally, the investigation of boulder-medium interaction in this thesis concerns the macroscopic reaction of the boulder (bouncing of boulder, impact force on the boulder), energy propagation and force chain microstructure evolution inside the impacted medium. The three items are closely related to each other (Figure 6.1). More specifically:

- The energy propagation process is related to the bouncing and impact force on the boulder. The increase of elastic strain energy is related to the strength developed within the medium to resist the impact loading. The bouncing/non-bouncing of boulder is a competition result of the incident energy of boulder to the strength as well as energy dissipation properties of the medium.

- The energy propagation process is related to the deformation and microstructure of the medium. The energy propagation process is related to the load transfer mechanisms which are characterized by the spatial and temporal evolution of force chains. The increase of kinetic energy and energy dissipation indicates the strong rearrangements of the granular medium, which triggers the buckling of force chain network.

- The micromechanical force transmission within the medium is closely related to the impact force on the boulder, which further influences the bouncing of the boulder.
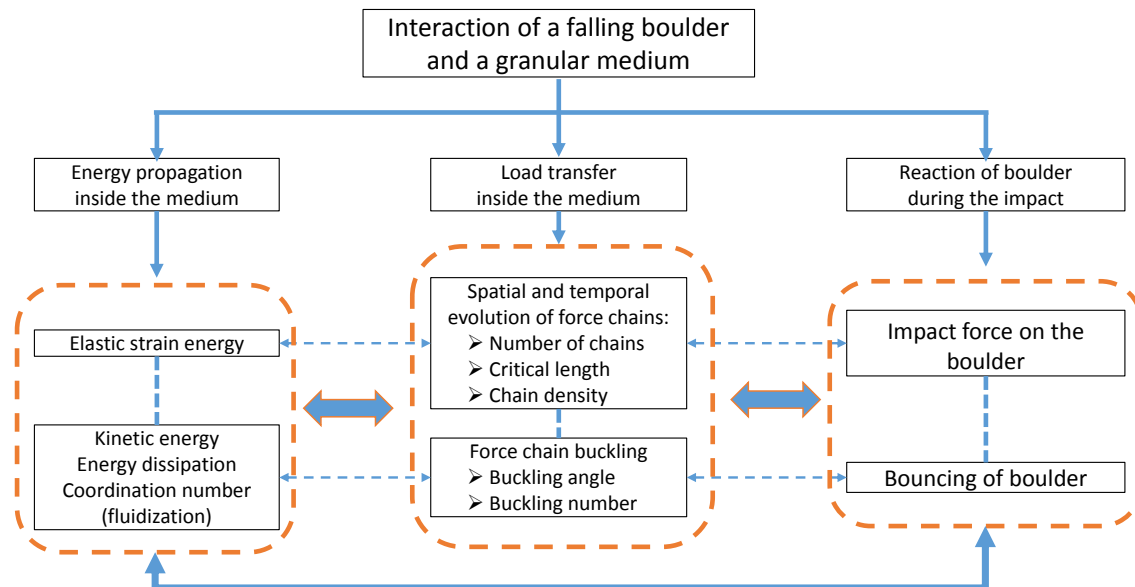


***Figure 6.1:*** *Relation among macroscopic reaction of boulder, energy propagation and force chain microstructure evolution inside the impacted medium*

Although focused on specific points, the investigations point out the important role of force chains upon the bouncing of the boulder, as a component in the force transmission inside the granular material that determines the impact force on the boulder. The investigations offer helps to the prediction of boulder trajectories as well as the design of protection structures.

## 6.2   Perspectives

The improvement of boulder-medium interaction model still needs research based investigations to understand the mechanisms and find the most important parameters that govern the bouncing of boulder as well as the response of the medium. The perspectives and future investigations can include particularly two aspects, the consideration of the particle crushing effects, and further investigation of the boulder-medium interaction with the consideration of grain clusters around force chains.

Particles near the impact zone particularly at the moment of impact are under high stresses which might induce the crushing of particles. The energy dissipation by particle crushing effects might not be negligible, and the way of frictional energy dissipation might be influenced as well. Besides, the strength and stress-strain behaviour of granular medium during the dynamic interaction process might be also influenced by this particle crushing effect.

Although force chain is shown to play an important role in both the strength and the microstructure of the impacted granular medium, the investigation needs to consider the grain clusters surrounding force chains. The stability of force chains relies on the surrounding grain clusters. The evolution of grain clusters and force chains govern the stress and strain evolution as well as the microstructure evolution of the granular material. Particularly, it has been proven in 2D quasi-static conditions that the buckling of force chains is related to the death of $c_3$ (cluster composed of three particles) and generation of $c_{6+}$ (cluster composed of six or beyond number of particles) (Arévalo et al., 2010; Tordesillas et al., 2014; Zhu et al., b,a).

In 3D dynamic impact cases, the microstructure of grain clusters that surround force chains will be much more complex than in 2D cases. The investigation of force chains and the surrounding grain loops will help well understand the micromechanisms that govern the response of granular medium. Based on this, we should be able to better quantify the most relevant soils, according to this microstructure that should be used in protective embankments. This further micromechanical investigation might benefit rock-fall engineering in terms of boulder trajectory predictions and protection structure design.

Based on the enriched model taking into account particle crushing effects as well grain clusters, simulations under various impact velocities and impact angles can be conducted to further investigate the bouncing of boulder.

# Bibliography

Agliardi, F., Crosta, G., and Frattini, P. (2009). Integrating rockfall risk assessment and countermeasure design by 3d modelling techniques. *Nat Hazards Earth Syst Sci*, 9(4):1059–1073.

Albaba, A., Lambert, S., Nicot, F., and Chareyre, B. (2015a). Modeling the impact of granular flow against an obstacle. In *Recent Advances in Modeling Landslides and Debris Flows*, pages 95–105. Springer.

Albaba, A., Lambert, S., Nicot, F., and Chareyre, B. (2015b). Relation between microstructure and loading applied by a granular flow to a rigid wall using dem modeling. *Granular Matter*, 17(5):603–616.

Antony, S. and Kuhn, M. (2004). Influence of particle shape on granular contact signatures and shear strength: new insights from simulations. *International Journal of Solids and Structures*, 41(21):5863–5870.

Arévalo, R., Zuriguel, I., and Maza, D. (2010). Topology of the force network in the jamming transition of an isotropically compressed granular packing. *Physical Review E*, 81(4):041302.

Asteriou, P., Saroglou, H., and Tsiambaos, G. (2012). Geotechnical and kinematic parameters affecting the coefficients of restitution for rock fall analysis. *International Journal of Rock Mechanics and Mining Sciences*, 54:103–113.

Asteriou, P., Saroglou, H., and Tsiambaos, G. (2013a). Rockfall: scaling factors for the coefficient of restitution. In *Proceedings of EUROCK2013 - The 2013 ISRM international symposium*, pages 195–200.

Asteriou, P., Saroglou, H., and Tsiambaos, G. (2013b). Rockfalls: influence of rock hardness on the trajectory of falling rock blocks. *Bulletin of the Geological Society of Greece, Greece, XLVII*.

ASTRA (2008). Actions de chutes de pierres sur les galeries de protection. *Département fédéral de l'environnement, des transports, de l'énergie et de la communication DETEC, Office fédéral des routes OFROU.*

Azzoni, A., La Barbera, G., and Zaninetti, A. (1995). Analysis and prediction of rockfalls using a mathematical model. In *International journal of rock mechanics and mining sciences & geomechanics abstracts*, volume 32, pages 709–724. Elsevier.

Bardet, J. (1994). Observations on the effects of particle rotations on the failure of idealized granular materials. *Mechanics of materials*, 18:159–182.

Belheine, N., Plassiard, J., Donzé, F., Darve, F., and Seridi, A. (2009). Numerical simulation of drained triaxial test using 3d discrete element modeling. *Computers and Geotechnics*, 36(1):320–331.

Bourrier, F., Dorren, L., Nicot, F., Berger, F., and Darve, F. (2009). Toward objective rockfall trajectory simulation using a stochastic impact model. *Geomorphology*, 110:68–79.

Bourrier, F. and Hungr, O. (2011). Rockfall dynamics: a critical review of collision and rebound models. *Rockfall engineering*, pages 175–209.

Bourrier, F., Kneib, F., Chareyre, B., and Fourcaud, T. (2013). Discrete modeling of granular soils reinforcement by plant roots. *Ecological Engineering*, 61P:646–657.

Bourrier, F., Nicot, F., and Darve, F. (2008). Physical processes within a 2d granular layer during an impact. *Granular Matter*, 10:415–437.

Bourrier, F., Nicot, F., and Darve, F. (2010). Evolution of the micromechanical properties of impacted granular materials. *Comptes Rendus Mécanique*, 338:639–647.

Bozzolo, D. and Pamini, R. (1986). Simulation of rock falls down a valley side. *Acta Mechanica*, 63(1-4):113–130.

Budetta, P. and Santo, A. (1994). Morphostructural evolution and related kinematics of rockfalls in campania (southern italy): A case study. *Engineering Geology*, 36(3):197–210.

Calvetti, F. (2008). Discrete modelling of granular materials and geotechnical problems. *European Journal of Environmental and Civil Engineering*, 12:7-8:951–965.

Calvetti, F., Di Prisco, C., and Vecchiotti, M. (2005). Experimental and numerical study of rock-fall impacts on granular soils. *Rivista Italiana di Geotecnica*, 4:95–109.

Cambou, B., Jean, M., and Radjai, F. (2013). *Micromechanics of granular materials*. John Wiley and Sons, USA.

Chareyre, B. and Villard, P. (2005). Dynamic spar elements and discrete element methods in two dimensions for the modeling of soil-inclusion problems. *Journal of Engineering Mechanics*, 131(7):689–698.

Chau, K., Wong, R., Liu, J., Wu, J., Lee, C., et al. (1999). Shape effects on the coefficient of restitution during rockfall impacts. In *9th ISRM Congress*. International Society for Rock Mechanics.

Chau, K., Wong, R., and Wu, J. (2002). Coefficient of restitution and rotational motions of rockfall impacts. *International Journal of Rock Mechanics and Mining Sciences*, 39(1):69–77.

China railway eryuan engineering group (1995). Techanical manuals for railway engineering design (tunnel).

Ciamarra, M., Lara, A., Lee, A., Goldman, D., Vishik, I., and Swinney, H. L. (2005). Dynamics of drag and force distributions for boulder impact in a granular medium. *Phys. Rev. Lett.*, 92:194301.

Clark, A., Petersen, A., Kondic, L., and Behringer, R. (2014). Nonlinear sound during granular impact. *arXiv preprint arXiv:1408.1971*.

Crassous, J., Beladjine, D., and Valance, A. (2007). Impact of a projectile on a granular medium described by a collision model. *Physical Review Letters*, 99(24):248001.

Cundall, P. and Strack, O. (1979). A discrete numerical model for granular assemblier. *Geotechnique*, 29(1):47–65.

de Bruyn, J. R. and Walsh, A. M. (2004). Penetration of spheres into loose granular media. *Canadian Journal of Physics*, 82(6):439–446.

Degago, S. (2007). Impact tests on sand with numerical modeling, emphasizing on the shape of the falling object. Master's thesis, Norvegian university of science and technology.

Degago, S., Ebeltoft, R., and Nordal, S. (2008). Effect of rock fall geometries impacting soil cushion: a numerical procedure. *The 12th International Conference of International Association for Computer Methods and Advances in Geomechanics (IACMAG)*, pages 4517–4524.

Descoeudres, F., Stoffel, S. M., Boll, A., Gerber, W., and Labiouse, V. (1999). *Chapter 4, Rockfalls*. in: Coping study on disaster resilient infrastructure, commissioned by the secretariat for the international decade for natural disaster reduction for the INDR programme forum 'Parterships for a safer world in the 21st century'.

Dolezalova, M., Czene, P., and Havel, F. (2002). Micromechanical modeling of stress path effects using pfc2d code. *Numerical Modeling in Micromechanics via Particle Methods*, 182.

Dorren, L. (2003). A review of rockfall mechanics and modelling approaches. *Progress in Physical Geography*, 27(1):69–87.

Dorren, L., Berger, F., and Putters, U. S. (2006). Real-size experiments and 3-d simulation of rockfall on forested and non-forested slopes. *Natural Hazards and Earth System Sciences*, 6:145–163.

Dorren, L., Domaas, U., Kronholm, K., and Labiouse, V. (2011). Methods for predicting rockfall trajectories and run-out zones. *Rockfall engineering*, pages 143–173.

Easton, V. J. and McColl, J. H. (1997). Statistics glossary.

Einhorn, B., Eckert, N., Chaix, C., Ravanel, L., Deline, P., Gardent, M., Boudières, V., Richard, D., Vengeon, J., Giraud, G., et al. (2015). Changements climatiques et risques naturels dans les alpes. impacts observés et potentiels sur les systèmes physiques et socio-économiques. *Journal of Alpine Research| Revue de géographie alpine*, (103-2).

Estrada, N., Azéma, E., Radjai, F., and Taboada, A. (2011). Identification of rolling resistance as a shape parameter in sheared granular media. *Physical Review E*, 84(1):011306.

Evans, S. and Hungr, O. (1993). The assessment of rockfall hazard at the base of talus slopes. *Canadian Geotechnical Journal*, 30(4):620–636.

Gerber, W. and Volkwein, A. (2010). Impact loads of falling rocks on granular material. *Darve F.; Doghri I.; El Fatmi R.; Hassis H*, pages 337–342.

Goddard, J. (1990). Nonlinear elasticity and pressure-dependent wave speeds in granular media. In *Proceedings of the Royal Society of London A: Mathematical, Physical and Engineering Sciences*, volume 430, pages 105–131. The Royal Society.

Hagenmuller, P., Theile, T., and Schneebeli, M. (2014). Numerical simulation of microstructural damage and tensile strength of snow. *Geophysical Research Letters*, 41(1):86–89.

Hardin, B. (1985). Crushing of soil particles. *J. Geotech. Engrg.*, 111 (10):1171–1192.

Heidenreich, B. (2004). *Small-and half-scale experimental studies of rockfall impacts on sandy slopes*. PhD thesis, EPFL.

Hentz, S., Daudeville, L., and Donzé, F. (2004). Identification and validation of a discrete element model for concrete. *Journal of engineering mechanics*, 130(6):709–719.

Highland, L. (2004). Landslide types and processes. Technical report.

Hou, M., Peng, Z., Liu, R., Lu, K., and Chan, C. (2005). Dynamics of a projectile penetrating in granular systems. *PHYSICAL REVIEW-SERIES E-*, 72(6):062301.

Hungr, O. and Evans, S. (1988). Engineering evaluation of fragmental rockfall hazards. In *5th International symposium on landslides*, volume 1, pages 685–690.

Iwashita, K. and Oda, M. (1998). Rolling resistance at contacts in simulation of shear band development by dem. *J. Eng. Mech. Div.*, 124 (3):ASCE: 285–292.

Iwashita, K. and Oda, M. (2000). Micro-deformation mechanism of shear banding process based on modified distinct element method. *Powder Technology*, 109:192–205.

JTJ013-95 (1995). Specifications for design of highway subgrades.

Kawahara, S. and Muro, T. (2006). Effects of dry density and thickness of sandy soil on impact response due to rockfall. *Journal of terramechanics*, 43(3):329–340.

Kenner, R., Phillips, M., Danioth, C., Denier, C., Thee, P., and Zgraggen, A. (2011). Investigation of rock and ice loss in a recently deglaciated mountain rock wall using terrestrial laser scanning: Gemsstock, swiss alps. *Cold Regions Science and Technology*, 67(3):157–164.

Kondic, L., Fang, X., Losert, W., O'Hern, C., and Behringer, R. (2012). Microstructure evolution during impact on granular matter. *Physical review.*, E85:011305.

Labiouse, V., Descoeudres, F., and Montani, S. (1996). Experimental study of rock sheds impacted by rock blocks. *Structural Engineering International*, 3/96:171–176.

Labiouse, V. and Heidenreich, B. (2009). Half-scale experimental study of rockfall impacts on sandy slopes. *Natural Hazards and Earth System Science*, 9(6):1981–1993.

Lambert, S. and Bourrier, F. (2013). Design of rockfall protection embankments: a review. *Engineering Geology*, 154:77–88.

Lambert, S., Bourrier, F., and Toe, D. (2013). Improving three-dimensional rockfall trajectory simulation codes for assessing the efficiency of protective embankments. *International Journal of Rock Mechanics and Mining Sciences*, 60:26–36.

Lorentz, J., Donzé, F., Perrotin, P., and Plotto, P. (2006). Experimental study of the dissipative efficiency of a multilayered protective structure against rockfall impact. *Revue européenne de génie civil*, 10(3):295–308.

Majmudar, T. and Behringer, R. (2005). Contact force measurements and stress-induced anisotropy in granular materials. *Nature*, 435:1079–1082.

Makse, H., Johnson, D., and Schwartz, L. (2000). Packing of compressible granular materials. *Physical review letters*, 84:4160.

Makse, H. A., Gland, N., Johnson, D., and Schwartz, L. (2004). Granular packings: Nonlinear elasticity, sound propagation, and collective relaxation dynamics. *Physical Review E*, 70(6):061302.

Mitchell, J. and Soga, K. (1976). *Fundamentals of Soil Behavior*. John Wiley and Sons, New York.

Mueth, D., Jaeger, H., and Nagel, S. (1998). Force distribution in a granular medium. *Physical Review E.*, 57:3164.

Neyman, J. (1937). Outline of a theory of statistical estimation based on the classical theory of probability. *Philosophical Transactions of the Royal Society of London. Series A, Mathematical and Physical Sciences*, 236(767):333–380.

Nicot, F. (2004). Constitutive modelling of snow as a cohesive-granular material. *Granular Matter*, 6(1):47–60.

Nicot, F., Gotteland, P., Bertrand, D., and Lambert, S. (2007). Multiscale approach to geo-composite cellular structures subjected to rock impacts. *Int. J. Numer. Anal. Meth. Geomech.*, 31:1477–1515.

Nicot, F., Hadda, N., Bourrier, F., Sibille, L., and Darve, F. (2011). Failure mechanisms in granular media: a discrete element analysis. *Granular Matter*, 13(3):255–260.

Nordstrom, K., Lim, E., Harrington, M., and Losert, W. (2014). Granular dynamics during impact. *Physical review letters*, 112(22):228002.

Nouguier-Lehon, C., Cambou, B., and Vincens, E. (2003). Influence of particle shape and angularity on the behaviour of granular materials: a numerical analysis. *International Journal for Numerical and Analytical Methods in Geomechanics*, 27(14):1207–1226.

Oda, M. and Kazama, H. (1998). Microstructure of shear bands and its relation to the mechanisms of dilatancy and failure of dense granular soils. *Geotechnique*, 48(4):465–481.

Oda, M., Konishi, J., and Nemat-Nasser, S. (1982). Experimental micromechanical evaluation of strength of granular materials: effects of particle rolling. *Mechanics of Materials*, 1:269–283.

Oger, L., Ammi, M., Valance, A., and Beladjine, D. (2005). Discrete element method studies of the collision of one rapid sphere on 2d and 3d packings. *The European Physical Journal E*, 17(4):467–476.

Oger, L., Ammi, M., Valance, A., and Beladjine, D. (2008). Study of the collision of one rapid sphere on 3d packings: Experimental and numerical results. *Computers & Mathematics with Applications*, 55(2):132–148.

Olmedo, I., Bourrier, F., Bertrand, D., Berger, F., and Limam, A. (2015). Felled trees as a rockfall protection system: Experimental and numerical studies. In *Engineering Geology for Society and Territory-Volume 2*, pages 1889–1893. Springer.

Pacheco-Vázquez, F., Caballero-Robledo, G., Solano-Altamirano, J., Altshuler, E., Batista-Leyva, A., and Ruiz-Suárez, J. (2011). Infinite penetration of a projectile into a granular medium. *Physical review letters*, 106(21):218001.

Peila, D. (2011). Ground reinforced embankments for rockfall protection: From real scale tests to numerical modeling. *Rockfall engineering*, pages 393–426.

Peila, D., Oggeri, C., and Castiglia, C. (2007). Ground reinforced embankments for rockfall protection: design and evaluation of full scale tests. *Landslides*, 4:255–265.

Pena, A., Garcia-Rojo, R., and Herrmann, H. (2007). Influence of particle shape on sheared dense granular media. *Granular Matter*, 9(3-4):279–291.

Peters, J., Muthuswamy, M., Wibowo, J., and Tordesillas, A. (2005). Characterization of force chains in granular material. *Physical review E*, 72:041307.

Pichler, B., Hellmich, C., and Mang, H. (2005). Impact of rocks onto gravel design and evaluation of experiments. *International Journal of Impact Engineering*, 31:559–578.

Pierson, L. A., Gullixson, C. F., Chassie, R. G., and Engineer, P. G. (2001). Rockfall catchment area design guide. Technical report, Oregon Department of Transportation, Research Group.

Plassiard, J., Belheine, N., and Donzé, F. (2009). A spherical discrete element model: calibration procedure and incremental response. *Granular Matter*, 11(5):293–306.

Plassiard, J. and Donzé, F. (2009). Rockfall impact parameters on embankments: a discrete element method analysis. *Structural Engineering International*, 19(3):333–341.

Plassiard, J., Donzé, F., and Plotto, P. (2005). High energy impact on embankments: a numerical discrete approach. *Discrete Element Group for Risk Mitigation*, page 57.

Prisco, C. and Vecchiotti, M. (2006). A rheological model for the description of boulder impacts on granular strata. *Geotechnique*, 56(7):469–482.

Radjaï, F. and Dubois, F. (2011). *Discrete-element modeling of granular materials*. Wiley-Iste.

Radjaï, F. and Lanier, J. (2009). Experimental and numerical analysis of local variables in granular materials. *Micromechanics of granular materials*, pages 1–49.

Radjaï, F., Wolf, D., Jean, M., and Moreau, J. (1998). Bimodal character of stress transmission in granular packings. *Physical review letters*, 80(1):61–64.

Razali, N. and Wah, Y. (2011). Power comparisons of shapiro-wilk, kolmogorov-smirnov, lilliefors and anderson-darling tests. *Journal of Statistical Modeling and Analytics*, 2(1):21–33.

Ronco, C., Oggeri, C., and Peila, D. (2009). Design of reinforced ground embankments used for rocfall protection. *Natural Hazards and Earth System Science*, 9(4):1189–1199.

Salot, C., Gotteland, P., and Villard, P. (2009). Influence of relative density on granular materials behavior: Dem simulations of triaxial tests. *Granular Matter*, 11:221–236.

Schellenberg, K. (2009). *On the design of rockfall protection galeries*. PhD thesis, Swiss Federal Institute of Technology Zurich.

Shapiro, S. S. and Wilk, M. (1965). An analysis of variance test for normality (complete samples). *Biometrika*, pages 591–611.

Shiu, W., Donzé, F., and Magnier, S. (2005). Numerical study of rockfalls on covered galleries by the discrete elements method. *Discrete Element Group for Risk Mitigation*, page 67.

Shodja, H. and Nezami, E. (2003). A micromechanical study of rolling and sliding contacts in assemblies of oval granules. *Int. J. Numer. Anal. Meth. Geomech.*, 27:403–424.

Šmilauer, V., Catalano, E., Chareyre, B., Dorofeenko, S., Duriez, J., Gladky, A., Kozicki, J., Modenese, C., Scholtès, L., Sibille, L., et al. (2010). Yade reference documentation. *Yade Documentation*, 474.

Stoffel, S. M. (1998). *Sollicitation dynamique de la couverture des galeries de protection lors de chutes de blocs*. PhD thesis, EPFL.

Szarf, K., Combe, G., and Villard, P. (2011). Polygons vs. clumps of discs: A numerical study of the influence of grain shape on the mechanical behaviour of granular materials. *Powder Technology*, 208(2):279–288.

Tordesillas, A., Steer, C., and Walker, D. (2014). Force chain and contact cycle evolution in a dense granular material under shallow penetration. *Nonlin. Processes Geophys.*, 21:505–519.

Tordesillas, A., Tobin, S., Cil, M., Alshibli, K., and Behringer, R. (2015). Network flow model of force transmission in unbonded and bonded granular media. *Physical Review E*, 91(6):062204.

Tordesillas, A., Zhang, J., and Behringer, R. (2009). Buckling force chains in dense granular assemblies: physical and numerical experiments. *Geomechanics and Geoengineering: An International Journal*, 4(1):3–16.

Tsimring, L. and Volfson, D. (2005). Modeling of impact cratering in granular media. *Powders and grains*, 2:1215–1223.

Vijayakumar, S., Yacoub, T., and Curran, J. H. (2011). On the effect of rock size and shape in rockfall analyses. In *Proceedings of the US Rock Mechanics Symposium (ARMA) San Francisco CA, USA*.

Volkwein, A., Schellenberg, K., Labiouse, V., Agliardi, F., Berger, F., Bourrier, F., Dorren, L. K., Gerber, W., and Jaboyedoff, M. (2011). Rockfall characterisation and structural protection-a review. *Natural Hazards and Earth System Sciences*, 11:p–2617.

Wang, J. and Yan, H. (2012). Dem analysis of energy dissipation in crushable soils. *Soils and Foundations*, 52(4):644–657.

Wilk, M. and Gnanadesikan, R. (1968). Probability plotting methods for the analysis for the analysis of data. *Biometrika*, 55(1):1–17.

Wong, R., Ho, K., and Chau, K. (2000). Shape and mechanical properties of slope material effects on the coefficient of restitution of rockfall study. In *4th North American Rock Mechanics Symposium*. American Rock Mechanics Association.

Ye, S., Chen, H., and Tang, H. (2010). Comparative research on impact force calculation methods for rockfalls. *Hydrogeology and Engineer geology*, 37(2):59–64.

Zhang, ., Wang, J., and Jiang, M. (2013). Dem-aided discovery of the relationship between energy dissipation and shear band formation considering the effects of particle rolling resistance. *Journal of Geotechnical and Geoenvironmental Engineering*, 139(9):1512–1527.

Zhang, G., Xiang, X., and Tang, H. (2011). Field test and numerical calculation of restitution coefficient of rockfall collision. *Chinese Journal of Rock Mechanics and Engineering*, 30(6):1266–1273.

Zhang, J., Majmudar, T., Tordesillas, A., and Behringer, R. (2010). Statistical properties of a 2d granular material subjected to cyclic shear. *Granular matter*, 12:159–172.

Zhang, L., Lambert, S., Nicot, F., and Bourrier, F. (2014). Contact law in granular assemblies: from statics to dynamics. In *Numerical methods in geotechnical engineering*, volume 1, pages 427–432.

Zhao, J. and Guo, N. (2014). Rotational resistance and shear-induced anisotropy in granular media. *Acta Mechanica Solida Sinica*, 27(1):1–14.

Zhou, B., Huang, R., Wang, H., and Wang, J. (2013). Dem investigation of particle anti-rotation effects on the micromechanical response of granular materials. *Granular Matter*, 15(3):315–326.

Zhu, H., Nicot, F., and Darve, F. The force-chain interaction with meso-structure in two-dimensional granular material of biaxial loading path. (under review).

Zhu, H., Nicot, F., and Darve, F. Meso-structure evolution in a 2d granular material during biaxial loading. (in press).

**Abstract**

This thesis deals with 3D DEM modelling of the interaction between a falling boulder and a granular medium in the context of rockfall. An elastic-plastic contact law, implemented with rolling resistance to consider soil particle shape effects, is used to model the dynamic impact process. The impact model is validated based on experiments from literature. The thesis investigates the bouncing of the boulder in relation with the evolution of some microstructure descriptors within the impacted medium.

Energy propagation processes are also analyzed within the impacted medium. Simulations under various boulder sizes and medium thickness conditions indicate that three bouncing regimes exist. Detailed investigations show that bouncing of a boulder is related to a relatively high strength and low energy dissipation capacity of the medium. Further micromechanical investigations indicate that the so-called force chains play an important role in the strength of the medium by constituting an appropriate network to transmit forces. The buckling of force chains appears to be the main microstructural feature that governs the penetration and possibly the absence of bouncing of a boulder.

**Keywords:** Rockfall, impact, granular material, DEM, bouncing, force chain.

**Résumé**

La thèse traite de la modélisation DEM 3D de l'interaction entre un projectile et un milieu granulaire dans le cadre des chutes de blocs. Une loi de contact élastique-plastique, incluant une résistance au roulement pour prendre en compte les effets de forme des particules, est implémentée pour modéliser le processus d'impact. Le modèle d'impact est validé à partir d'expériences issues de la littérature. Ce travail s'intéresse en particulier au rebond du bloc en relation avec l'évolution de la microstructure du milieu impacté.

Le rebond du bloc est étudié à partir des processus de propagation d'énergie au sein du milieu impacté. Des simulations considérant plusieurs tailles de bloc et plusieurs épaisseurs du milieu montrent que trois régimes de rebond existent. Une étude détaillée révèle que le rebond du bloc est lié à la résistance mécanique du milieu et aux faibles capacités de dissipation d'énergie. L'analyse micromécanique démontre que les chaines de force jouent un rôle majeur dans la résistance du milieu en formant un réseau capable de transmettre les forces. L'effondrement de ces chaînes de force apparaît donc comme étant la principale caractéristique microstructurelle contrôlant la pénétration voire l'absence de rebond du bloc.

**Mots-clés:** Chute de bloc, impact, matériau granulaire, DEM, rebond, chaîne de force.